

High Throughput Optical Sensor Arrays for Drug Screening

By

Daniel I. Harjes

B.S. Mechanical Engineering
Lehigh University, 2004

SUBMITTED TO THE DEPARTMENT OF MECHANICAL ENGINEERING IN
PARTIAL FULFILLMENT OF THE REQUIREMENTS FOR THE DEGREE OF

MASTERS OF SCIENCE IN MECHANICAL ENGINEERING
AT THE
MASSACHUSETTS INSTITUTE OF TECHNOLOGY

SEPTEMBER 2006

Copyright ©2006 Daniel I. Harjes. All rights reserved

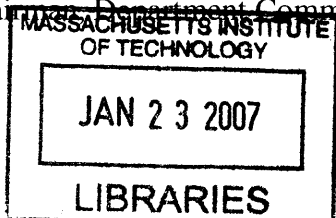
The author hereby grants to MIT permission to reproduce and to distribute publicly paper
and electronic copies of this thesis document in whole or in part.

Signature of Author _____
Department of Mechanical Engineering
July 10, 2006

Certified by _____
Dr. Heather A. Clark
Charles Stark Draper Laboratory
Thesis Supervisor

Certified by _____
Professor Roger D. Kamm
Associate Head of Mechanical Engineering
Thesis Advisor

Accepted by _____
Professor Lallit Anand
Chair, Mass. Department Committee on Graduate Students



BARKER

High Throughput Optical Sensor Arrays for Drug Screening

By

Daniel I. Harjes

Submitted to the Department of Mechanical Engineering on July 10, 2006
in partial fulfillment of the requirements for the degree of Masters of
Science in Mechanical Engineering

Abstract

In the world of drug discovery, high throughput whole cell assays are a critical step in discovering therapeutically relevant drug compounds [1]. This report details the development of several novel sensor systems capable of detecting cellular ion flux in multi-well plate format. Optodes are employed as the primary sensors, which are an optically based ion selective polymer. These assays utilize both potassium and sodium selective optodes to provide real time measurements of extracellular ion concentration, which can yield extremely valuable information regarding compound induced cellular activity [2]. Individual assay formats have been specifically tailored for use with both adherent and suspended cell lines.

For adherent cell lines, the optode based sensor system was evaluated using an HEK 293 cell model. To evoke cellular activity, the cells were exposed to Isoproterenol and Forskolin, which are known to elicit intracellular cyclic AMP production. The assay proved robust in detecting long term drug induced extracellular potassium flux. Ion flux magnitude was used to generate EC50 values of 1.185 nM and 66.5 nM for Isoproterenol and Forskolin, respectively. These values correlate closely with reported values that were attained with assays using intracellular calcium as the active biomarker [3-5].

In a secondary application, a potassium optode based system was developed to screen for QT prorogating compounds, such as Haloperidol. Modern hERG screening protocols are relatively low throughput and expensive using existing commercially available patch clamping techniques [6]. The system described in this report offers a less expensive alternative technology that permits cells to operate under natural biological conditions. Test data indicates the system was able to detect 30% reductions in potassium flux magnitude from neonatal mouse cardiac Myocytes upon exposure to 2.0 uM Haloperidol. The changes in action potential properties were not detectable using transmitted light data alone.

Technical Supervisor: Dr. Heather A. Clark
Title: Senior Member Technical Staff (Draper Laboratory)

Thesis Advisor: Professor Roger D. Kamm
Title: Associate Head of Mechanical Engineering and Germeshausen Professor of Mechanical and Biological Engineering (MIT)

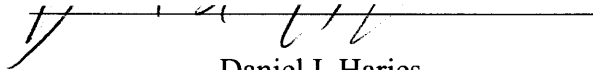
This page intentionally left blank

ACKNOWLEDGMENT

07/10/2006

This thesis was prepared at The Charles Stark Draper Laboratory, Inc., under Internal Company Sponsored Research Project 20270-001, Optical Biosensor Arrays.

Publication of this thesis does not constitute approval by Draper or the sponsoring agency of the findings or conclusions contained herein. It is published for the exchange and stimulation of ideas.



Daniel I. Harjes

This page intentionally left blank

Table of Contents

ABSTRACT	3
ACKNOWLEDGMENT	5
TABLE OF CONTENTS	7
INTRODUCTION	11
1.1 - THEORY OF CELLULAR ION SIGNALING AND ASSAY MECHANISMS	11
<i>1.1.1: Basics of Cellular Ion Signaling</i>	<i>11</i>
<i>1.1.2: Current Methods for Drug Discovery</i>	<i>16</i>
<i>1.1.3: Electrical Model of an Action Potential</i>	<i>17</i>
<i>1.1.4: Toxicity Screening: hERG and Long QT Syndrome</i>	<i>19</i>
1.2 – OPTICAL ION SENSORS (OPTODES)	22
<i>1.2.1: Optode Development</i>	<i>22</i>
<i>1.2.2: Response Mechanism</i>	<i>23</i>
<i>1.2.3: Selectivity</i>	<i>29</i>
<i>1.2.4: Sensitivity, Resolution, and Dynamic Range</i>	<i>30</i>
<i>1.2.5: Reversibility</i>	<i>31</i>
<i>1.2.6: Dynamics</i>	<i>31</i>
<i>1.2.7: Component Leaching</i>	<i>32</i>
<i>1.2.8: Optode Limitations</i>	<i>32</i>
1.3 – NOVEL OPTODE BASED ASSAY SYSTEMS	33
<i>1.3.1: Assay Descriptions</i>	<i>33</i>
<i>1.3.2: Advantages over Current Techniques</i>	<i>34</i>
<i>1.3.3: Disadvantages over Current Techniques</i>	<i>34</i>
CHAPTER 1 - OPTODE DEVELOPMENT	35
1.1 – DEVELOPMENT OF SODIUM AND POTASSIUM OPTODES	35
<i>1.1.1: Introduction</i>	<i>35</i>
<i>1.1.2: Component Selection</i>	<i>35</i>
<i>1.1.3: Theoretical Response</i>	<i>37</i>
1.2 – EXPERIMENTAL METHODS	38
<i>1.2.1: Reagents</i>	<i>38</i>
<i>1.2.2: Optics</i>	<i>39</i>
<i>1.2.3: Optode Membrane Preparation (Various Techniques)</i>	<i>39</i>
<i>1.2.4: Calibration Protocol</i>	<i>42</i>
<i>1.2.5: Data Acquisition and Processing</i>	<i>43</i>
1.3 – RESULTS AND DISCUSSION I: MEMBRANE FABRICATION TECHNIQUES	43
<i>1.3.1: Evaporation Coating</i>	<i>43</i>
<i>1.3.2: Spray Coating</i>	<i>46</i>
<i>1.3.3: Spin Coating</i>	<i>48</i>
<i>1.3.4: Micro-sphere deposition</i>	<i>49</i>
<i>1.3.5: Technique Comparison</i>	<i>50</i>
1.4 – RESULTS AND DISCUSSION II: OPTODE PERFORMANCE	51
<i>1.4.1: K-Optode I Response Properties</i>	<i>51</i>
<i>1.4.2: K-Optode II Response Properties</i>	<i>53</i>
<i>1.4.3: Na-Optode I Response Properties</i>	<i>57</i>
<i>1.4.4: Sensitivity, Resolution and Dynamic Range</i>	<i>58</i>
<i>1.4.5: Reversibility</i>	<i>60</i>
<i>1.4.6: Response Time</i>	<i>61</i>
CHAPTER 2: SUSPENDED CELL ASSAYS	63
2.1 – ASSAY PROPERTIES	63
<i>2.1.1: Applications - The Advantage of Suspended Cell Lines</i>	<i>63</i>
<i>2.1.2: Assay Design Criteria</i>	<i>63</i>

2.1.3: Assay Design - Optode Disks.....	64
2.1.3: Limitations.....	65
2.2 – TARGET CELL LINE: SACCHAROMYCES CEREVISIAE	66
2.2.1: Cell Properties.....	66
2.2.2: Test Compounds - Haloperidol and Ifenprodil.....	66
2.3 – EXPERIMENTAL METHODS.....	67
2.3.1: Reagents	67
2.3.3: Yeast Culture	67
2.3.4: Assay Protocol.....	67
2.3.4: Data Processing	68
2.4 – RESULTS AND DISCUSSION	69
2.4.1: Dose Response.....	69
2.4.3: Assay Conclusions	73
CHAPTER 3: ADHERENT CELL ASSAY.....	74
3.1 – ASSAY PROPERTIES.....	74
3.1.1: Applications - Biological Relevance of Adherent Cell Lines.....	74
3.1.2: Assay Design Criteria.....	74
3.1.2: Assay Design: Optode Insert Module (OIM).....	76
3.1.3: Limitations.....	83
3.2 – EXPERIMENTAL CELL LINE: HEK 293	84
3.2.1: Cell Properties.....	84
3.2.2: Test Compounds – Isoproterenol and Forskolin.....	85
3.2.3: Theoretical Response.....	86
3.3 – EXPERIMENTAL METHODS.....	86
3.3.1: Reagents	86
3.3.2: Optode Insert Preparation.....	87
3.3.3: HEK 293 Culture and Proliferation	87
3.3.4: Assay Protocol.....	87
3.3.5: Data Processing	88
3.4 – RESULTS AND DISCUSSION	90
3.4.1: Isoproterenol and Forskolin EC50s'	90
3.4.2: Z-Factor.....	92
CHAPTER 4: HERG SCREENING ASSAY.....	94
4.1 – TARGET CELL LINE: NEONATAL MOUSE CARDIAC MYOCYTE.....	94
4.2.1: Cell Properties.....	94
4.2.2: Test Compounds - Haloperidol.....	94
4.2 – THEORETICAL RESPONSE: SYSTEM MODELING	95
4.2.1: Model Generation: Modified Nygren.....	95
4.1.2: Model Output.....	96
4.3 – SYSTEM PROPERTIES.....	101
4.3.1: Applications.....	101
4.3.2: Design Criteria.....	101
4.3.3: Design 1: CSOS.....	102
4.3.4: CSOS Limitations	104
4.3.5: Design 2: Stimulation Chamber	105
4.3.6: Stimulation Chamber Limitations.....	107
4.4 – EXPERIMENTAL METHODS.....	108
4.4.1: Reagents	108
4.4.2: Optode Preparation 1: CSOS.....	108
4.4.3: Optode Preparation 2: Chamber.....	108
4.4.4: Myocyte Culture	108
4.4.5: Testing Protocol 1: CSOS.....	109
4.4.6: Testing Protocol 2: Stimulation Chamber	109
4.4.7: Data Processing	110

4.5 – RESULTS AND DISCUSSION	111
4.5.1: CSOS Beat Pattern Results	111
4.5.2: Optode Chamber Beat Pattern Results	119
4.5.3: hERG Screening Future Work	121
CONCLUSIONS.....	123
BIOGRAPHICAL NOTE	126
BIBLIOGRAPHY	127

This page intentionally left blank

Introduction

I.1 - Theory of Cellular Ion Signaling and Assay Mechanisms

This thesis introduces a series of novel optically based assay systems. Before presenting these assays, it is necessary to understand the principles behind cellular signaling and assay mechanisms. Section I.1.1 reviews the basics of cellular ion signaling, which include modeling the cell as an electrical system. The classic Hodgkin-Huxley circuit model is presented, which details how the cell is capable of regulating ion currents [2]. Cellular ion signaling represents the core of virtually all current high throughput whole cell based assays. Section I.1.2 summarizes the existing drug discovery process and explores the various techniques employed in bringing a drug to market. Many of these include high throughput assays that measure ion channel activity. Following this, Section I.1.3 expands the cellular ion channel model described in Section I.1.1 to include excitable cell lines. This advanced analysis contains a detailed electrical model of the cell, which incorporates individual ion channel families. Finally, Section I.1.4 explains the highly important field of toxicity screening referred to as hERG screening. The hERG (human-ether-a-go-go) gene is responsible for encoding a family of potassium channels responsible for re-polarizing the membrane following an action potential [7]. Blockage of these channels in cardiac cells in vivo leads to arrhythmia and possible death.

I.1.1: Basics of Cellular Ion Signaling

Every living cell is encapsulated by a thin lipid membrane that separates the cytoplasm from the extracellular environment. The hydrogen bonds that comprise this membrane have an extremely high dielectric constant. Since the fluid mediums on either side of the membrane are highly conductive, a cell can be modeled as a parallel plate capacitor. This enables the cell to efficiently store electrical charge and generate a potential across the membrane (membrane potential). The ability of the cell to regulate and control membrane potential represents the basis for cellular ion signaling.

A cell is able to charge and discharge through a series of ion channels imbedded in the membrane. Highly selective gating mechanisms allow particular families of channels to be permeable to only one type of ion, such as potassium. In most cells, potassium, sodium, calcium, and chloride represent the four primary ions used to regulate membrane potential. Calcium transport inside the cell is extremely complex and is responsible for hundreds of cellular mechanisms in addition to voltage regulation. The majority of cellular activity usually results in some form of ion flux across the membrane. The ability to detect and quantify these ion fluxes can yield highly valuable information regarding cellular response mechanisms.

Excitable cell lines are unique because they have additional ion channels which enable them to produce an action potential. An action potential is an abrupt voltage spike triggered by a slight increase in membrane potential. They can be initiated by neighboring cells or an external stimulus, such as a drug. If a series of excitable cells are connected to form a long chain, they can propagate electrical signals (nerve cells). Action potentials are the principle mechanism behind all electrical signal transmission

within the human body. They are also used to control muscle contraction and a host of other cellular control mechanisms.

In order to understand the theory behind cellular ion flux, it is vital to develop an appropriate electrical model of the cell. The most widely accepted model is that developed by Hodgkin-Huxley in 1952. This model will be utilized throughout this report as a foundation for modeling ion flux.

As stated previously, a cell can be modeled as an ideal parallel plate capacitor. Typical cell membranes have a specific capacitance on the order of $1.0 \mu\text{F}/\text{cm}^2$, which has been determined experimentally based on patch clamp techniques. Assuming a dielectric constant of 2.1 (hydrocarbon chains), the estimated membrane thickness is approximately 2.3 nm, or 23 Å [2]. This is supported by the formal definition for the capacitance of a parallel plate capacitor in Equation 1.

$$C = \frac{\epsilon\epsilon_0 A}{d}$$

C = Capacitance (Farad)

ϵ = Dielectric Constant

ϵ_0 = Polarizability of Free Space (8.85e^{-12})

A = Surface Area

d = Gap Thickness

Equation 1: Capacitance of a Parallel Plate Capacitor

Ion channels electrically bridge the extracellular and intracellular environments. By altering gating mechanisms, they are able to control their conductivity towards particular ions. Combining membrane capacitance with ion channel resistance yields a simple RC circuit model for a cell, which is shown in Figure 1. Notice the membrane resistor is variable to account for changing channel conductivities.

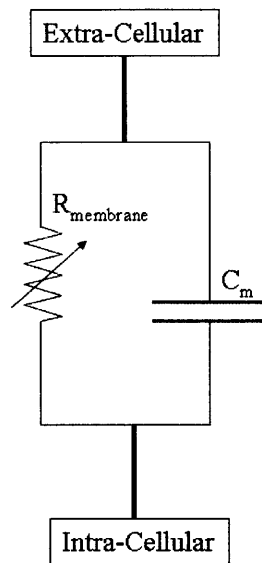


Figure 1: RC Model of a Cell Membrane Circuit [2]

The circuit diagram in Figure 1 is useful for intuitive understanding of ion signaling; however, further modeling is required to accurately represent a cell. Cellular circuitry is more complex than typical electrical systems because each type of ion represents a unique current. These currents sum to control the overall membrane potential. For each type of current, there are two potential gradients that drive ion flow. The most obvious of these potentials are the electrostatic forces produced by the charge differential across the membrane. The second potential in the system is created by the ion concentration gradient across the membrane (thermodynamic forces). In a cell, these two forces can act together, or oppose each other depending on the state of the cell. For each ionic current, there is a specific membrane potential that perfectly opposes concentration gradient forces. This potential is referred to as the equilibrium potential. It is unique for each ion and is dependant on the temperature and the concentration gradient.

This concept can be easily explained using a simple example. Imagine a highly conductive salt bath separated by a thin dielectric barrier. The barrier is also ideally permeable to potassium ions (K^+). The dielectric barrier allows the bath to store electrical charge. This situation is depicted by the basic diagram in Figure 2 below. Now imagine an arbitrary amount of potassium chloride is added to one side of the bath. Initially, potassium ions will diffuse through the barrier as a result of the concentration gradient. As this occurs, the left side of the bath will decrease charge and the right side will increase by an equal magnitude. This charge buildup will cause an electrostatic potential that opposes current flow. At a certain point, the electrostatic forces will balance thermodynamic forces and potassium ion flow will cease. The resulting voltage

across the barrier represents the equilibrium potential for potassium under those particular conditions [2].

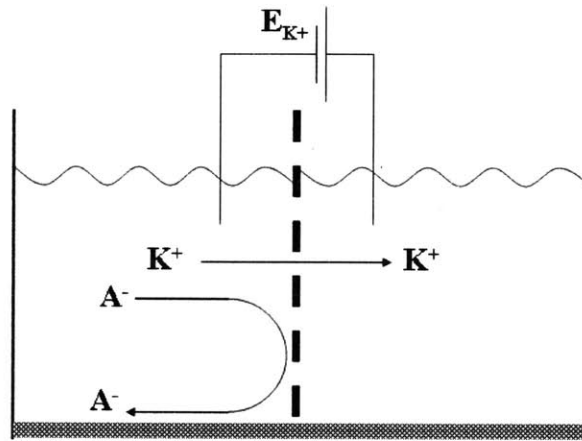


Figure 2: Equilibrium Potential with Ion Permeable Membranes [2]

The equilibrium potential is formally defined with the Nernst equation, which is displayed below in Equation 2.

$$E_n = E_1 - E_2 = \frac{RT}{z_s F} \ln \left(\frac{[S]_2}{[S]_1} \right)$$

E_n = Equilibrium Potential

R = Gas Constant

T = Temperature

F = Faraday Constant

z_s = Ion Charge

$[S]_n$ = Respective Ion Concentration

Equation 2: Nernst Equation for Calculating Equilibrium Potential [2]

The equilibrium potential for any ion is dependant on temperature and concentration differential. Under typical biological conditions, the Nerst potentials for the four primary biological ions are shown in Table 1.

Ion	[C] _o (mM)	[C] _i (mM)	[C] _o /[C] _i	Equilibrium Potential (mV)
Na ⁺	145	12	12	67
K ⁺	4	155	0.026	-98
Ca ²⁺	1.5	1.00E-04	15,000	129
Cl ⁻	123	4.2	29	-90

Table 1: Typical Equilibrium Potentials for Primary Ions under Standard Biological Conditions [2]

In a vast majority of cell lines, the membrane is highly conductive to potassium ions at rest (open potassium channels). This drives the resting membrane potential close to the equilibrium potential for potassium, which can range between -60 and -100 mV. Additional background leakage and pump activity will alter this potential between various cell types and biological environments.

The concept of equilibrium potential can now be used to augment the simple RC circuit model presented in Figure 1. In series with each ion branch is a voltage source that is equal to the equilibrium potential for that particular ion. This updated cell system is shown by the following schematic in Figure 3 [2].

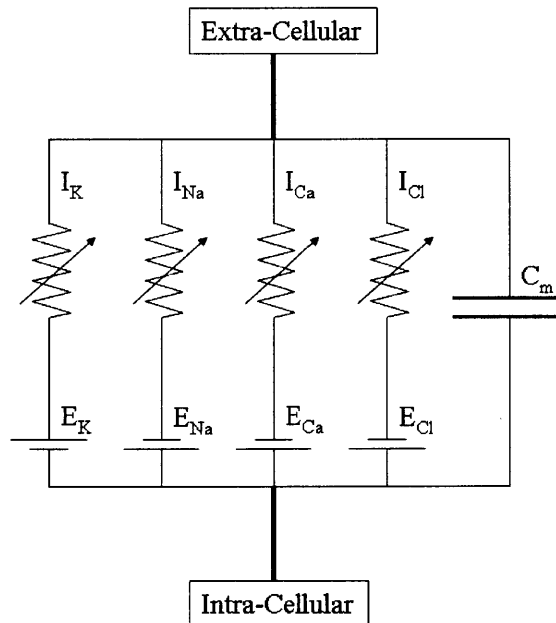


Figure 3: Cell Membrane Electrical Schematic Including Equilibrium Potentials

Using this model, it is relatively easy to predict the effects of altering the conductivity of individual ion channels. Opening sodium channels and closing potassium

channels would cause a rapid influx of sodium into the cell. The rate of this influx would be dependant on the product of the membrane capacitance and the resistivity of the sodium channels (RC discharge time constant). The de-polarization would continue until the membrane potential achieved the equilibrium potential for sodium (around +80mv). In Section I.1.3, this model is further expanded to include particular families of ion channels for each type of ion. This will add a set of parallel resistors in each current branch.

I.1.2: Current Methods for Drug Discovery

Pharmaceutical companies invest considerable amounts of capital and man hours to bring a single drug to market. It has been estimated that it costs in excess of one billion dollars to develop and release a single drug [8]. A significant percentage of that cost is spent developing compounds that never make it to market despite having beneficial therapeutic properties.

The drug discovery process begins with a single target, which is often either an enzyme or a receptor site. Inhibiting this enzyme or activating the receptor site is expected to produce the desired biological effects (pain relief, anti-inflammatory, etc). Depending on the extent of knowledge regarding the chemistry of the target, a variety of steps are taken to initiate the development process. Often, very little information is known regarding the chemical properties of the target [9]. In this case, teams of medicinal chemists will design libraries of compound families that are suspected to interact with the target. Many of these libraries can be in excess of 50,000 compounds. Following manufacturing, high throughput screening assays are employed to detect “hit” compounds that elicit the appropriate biological activity. This entire process is referred to as “Early stage research and development”. Typically, the screening process will eliminate approximately 95% of the initial compound library from the development process. The remaining 5% of compounds will proceed to the next phases of development, which include toxicity screening, animal studies, and clinical trials [10]. Only a select few compounds will make it to clinical trials.

For some targets, binding assays can be used as the preliminary screening tool. Binding assays are relatively simple chemical reactions that determine how effective compounds will bind to certain biological components [11]. They are extremely high throughput, but do not give reliable information regarding a compounds behavior in living biological systems. For this reason, it is difficult to predict how compounds will actually act on the target in a living system (large percentage of false positive and false negatives).

An additional screening tool is the high throughput whole cell based assay. Whole cell assays expose libraries of compounds to various living cell lines and detect certain changes in cellular activity [1, 12]. Cellular activity is monitored using sensors that are able to monitor specific biomarkers, which are indications of the state of the cell. Biomarkers can include membrane potential and intracellular calcium concentration. The most popular family of sensors used in existing high throughput infrastructures are optically based, largely fluorescent, indicator dyes [13]. Calcium selective dyes are extremely popular because of the importance of intracellular calcium to many response mechanisms. In addition, commercially available calcium dyes, such as Fluo-4, have

excellent performance characteristics such as sensitivity and reliability. Whole cell assays achieve similar throughput to binding assays, but are capable of producing highly valuable information regarding actual cellular activity.

Compounds that elicit activity in whole cell assays proceed to a series of relatively low throughput pre-clinical animal studies and toxicity screening protocols. Such toxicity tests include hERG screening, which is detailed in Section I.1.4. Compounds that pass this stage will then file an Investigational New Drug (IND) application and proceed to rigorous clinical trials, which are split into three initial phases. These initial clinical trials can last up to seven years [10]. Any compounds that proceed to clinical trials, only to be deemed not-efficacious, will add millions of dollars in additional expenses to the development process.

The assays developed in this report introduce a new type of bio-sensor system that can detect previously immeasurable cellular activity markers. These assays could be used to replace or augment traditional cell based assays and toxicity screening.

I.1.3: Electrical Model of an Action Potential

Excitable cell lines have the ability generate and transmit electrical signals using action potentials. Action potentials are abrupt increases in membrane potential caused by the rapid activation of sodium and calcium channels. In muscle cells, action potentials result in a cascade of cellular response mechanisms that eventually lead to contraction. Section I.1.1 consists of an introduction into cellular ion channel modeling using a simple parallel RC circuit. This model helps with basic conceptual understanding, but is insufficient to predict the behavior of excitable cell lines. To accurately model and simulate an action potential, additional ion channels and pumps must be added and their behavior classified. This model will be used later in this report as a tool to estimate changes in ion concentrations during a series of action potentials.

Over the past thirty years, patch clamp studies have revealed an assortment of ion channel families that play key roles in the generation of an action potential. Certain biologically relevant cell lines have been extensively studied. As a result, the voltage-conductance relationship for many of their ion channel families has been accurately characterized. Since the mid-1980's, researchers have searched for a suitable mathematical model to describe the properties of an action potential [14]. In 1998, Nygren and coworkers developed a detailed mathematical model for the adult human atrial cell [15]. The model is highly complex, but accurately reproduces patch clamp results. Their work revealed that a minimum of nine ion channels and three ion pumps were required to successfully reproduce observed atrial action potentials. The electrical schematic used to represent the cell is pictured in Figure 4 below.

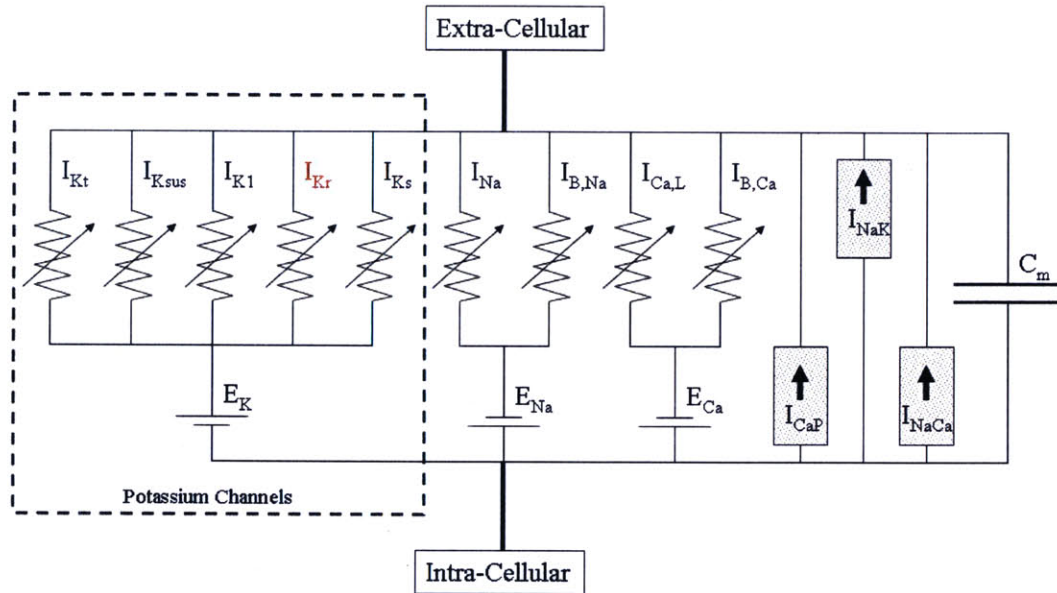


Figure 4: Nygren Electrical Schematic of a Human Atrial Cell [15]

Though this model is specific to the human atrial cell, its action potential characteristics are similar to many excitable cell lines. The model includes five potassium, two sodium, and two calcium channels with three ATP consuming ion pumps. The pumps act to continuously restore ion concentrations to their resting levels. Each ion channel is modeled as a variable resistor, which is governed by a first order ODE (ordinary differential equation). Each ODE defines channel conductance as a function of time and membrane potential. These functions were derived by curve fitting empirical data from patch clamp studies. Detailed information regarding these equations can be located in the original model publication [15].

In this model, an action potential is initiated by a slight increase in membrane potential caused by external stimuli. For simulation purposes, this is created by a millisecond duration square wave pulse of current into the cell. In vivo, this is usually the result of induced current flow from a neighboring cell (action potential propagation). When the membrane potential exceeds its “launch” voltage (around -50 mV), I_{Na} channels open and sodium ions rush into the cell and further depolarize the membrane. Simultaneously, voltage activated calcium channels open causing secondary depolarizing current into the cell. Together, these currents can sum together to drive the membrane potential as high as +50 mV. As the membrane potential crests +30 mV, sodium and calcium channels quickly inactivate and become highly resistive to current flow. At this point, four of the five potassium channels begin to activate in various manners causing an outward ion flux. Eventually, these outward potassium currents will restore the cell to its resting potential of around -85 mV. Throughout and after this process, the ion pumps are continuously working to restore ion concentrations to their resting levels [15].

Each of the four potassium channels has a distinct role in re-polarizing the membrane. I_{Kt} and I_{Ksus} represent the transient and sustained outward potassium currents, respectively. In many cell lines, these two currents are responsible for the majority of cell re-polarization. They activate quickly and cause sharp potassium currents at the onset of the action potential. Their opening virtually neutralizes the membrane potential after sodium and calcium channels inactivate. I_{Kt} activates extremely fast but only remains open for a few milliseconds. I_{Ksus} is larger in magnitude and usually remains open for a longer period.

I_{Ks} and I_{Kr} represent the two forms of delayed rectifier currents. They dominate the final stage of an action potential and are the two channels responsible for restoring the membrane potential to its resting state. I_{Kr} is quickly activating and has a substantial impact on re-polarization. Despite being slower and lower in magnitude, I_{Ks} has been shown to have significant effects on re-polarization times at high beat frequencies [15]. Virtually all anti-arrhythmic drugs target and block I_{Kr} channels, which leads to a prolonged re-polarization period [16, 17]. This phenomenon extends the overall action potential duration (APD) and is referred to as a long QT interval (LQT). This will be explained further in the following section. Chapter 4 is entirely based on the detection of I_{Kr} block over a series of action potentials.

The exact characteristics of each potassium channel vary greatly between species and cell type. For example, I_{Kr} currents are quite large in human ventricular myocytes, but are virtually non-existent in mouse lines [18]. This causes significant problems when investigating the effects of channel block in non-human cell lines. Even standard long term genetic mutations in identical cell lines can alter the performance of various ion channels.

I.1.4: Toxicity Screening: hERG and Long QT Syndrome

The human heart is a highly sophisticated pump that operates through a complex system of electrical signaling and compartmental contraction. The electrical signals that trigger a heart contraction originate from a group of cells referred to as pacemakers. They will drive contraction frequencies anywhere between 70 and 200 beats per minute depending on the extent of physical activity. When the pacemaker cells trigger, a series of action potentials propagate to various regions of the heart. As these action potentials reach cardiac myocytes in the atrium and ventricle, they trigger a muscular contraction. In vivo, cardiac electrical signals are monitored using an electro-cardio gram (ECG or EKG). Using two electrodes, the average membrane potential over a large population of cardiac cells can be monitored. For each beat, an EKG trace is split into five unique phases labeled 0-4. These phases are defined in Table 2 [19].

Phase	Description	Driving Currents
0	De-Polarization	I_{Na^+} , I_{Ca}
1	Partial Re-Polarization	$I_{K_{sub}}$, I_{Kt}
2	Plateau	I_{Ca} , I_{Kr} , I_{Ks}
3	Myocellular Re-Polarization	I_{Kr} , I_{Ks}
4	Ventricular Relaxation	I_{K1} , I_{Ks}

Table 2: Primary Driving Currents for Each Stage of an Action Potential [19]

In certain unique cases, the heart experiences abnormal beat patterns known as arrhythmias, which can lead to instantaneous death. A large percentage of arrhythmias are caused by Long QT (LQT) syndrome [20]. As stated in the previous section, this refers to the elongation of the QT interval [21]. The QT interval represents the time between phases 1-3 on an EKG trace, which is a measure of overall re-polarization time. When LQT syndrome results in arrhythmia, it is referred to as Torsades de Points. This name refers to the “twisting of the points” on an EKG trace over time. LQT syndrome can be inherited, acquired, or both. Inherited LQT syndrome is the result of genetic mutations that cause abnormal ion channel formation. A total of six genes have been reported to cause arrhythmic behavior: KVLQT1, hERG, SCN5A, minK, MiRP1, RyR2. These genes encode a variety of I_{Kr} and I_{Ks} ion channels. Of these KVLQT1, minK, hERG, and MiRP1 mutations have been directly linked with LQT syndrome. The range in severity of these mutations in clinical patients is very large; therefore the extent of QT elongation is unique to each individual [19]. In some cases people experiencing I_{Kr} mutational deficiencies have increased I_{Ks} activity to compensate [22]. For these individuals, their QT interval was not noticeably elongated. This makes it highly difficult to characterize a person’s susceptibility to Torsades de Points based on genetic analysis alone.

LQT syndrome can also be acquired by pharmacological block of hERG encoded I_{Kr} channels. Unfortunately, a large number of pharmaceutical compounds have been known to block hERG [23]. Pharmacologists have tried desperately to understand the physical and chemical properties of hERG channels to better understand how such a large variety of compounds can inhibit channel function. It is suspected that hERG channels having larger inner cavities than typical voltage gated potassium channel. This makes it easier for various compounds to enter and block the channel. FDA regulations require that every compound released to market be screened for hERG channel inhibition. This screening process is typically performed using patch clamp analysis [18, 24, 25].

Whole cell patch clamping permits conductivity measurements on a “patch” of cell membrane. This is accomplished by placing a glass micro-pipette electrode onto the membrane surface. If performed properly, this will allow ions to flow from the cell cytoplasm into the glass electrode. It is essential that the seal between electrode and membrane be highly resistive ($1e^9 \Omega$). Through this protocol, a circuit is created that can be used to hold the membrane at various potentials and measure the resulting current flow through the ion channels. Using highly selective channel blockers, virtually every ion channel in the cell can be blocked except for the channel of interest. By measuring

current flow across the membrane at various bias-voltages, the voltage-conductivity properties for that ion channel type can be classified. This process is depicted in Figure 5. By measuring current flow, patch clamping provides very accurate information regarding ion channel blockage. Despite the power of this technique, it has several inherent limitations.

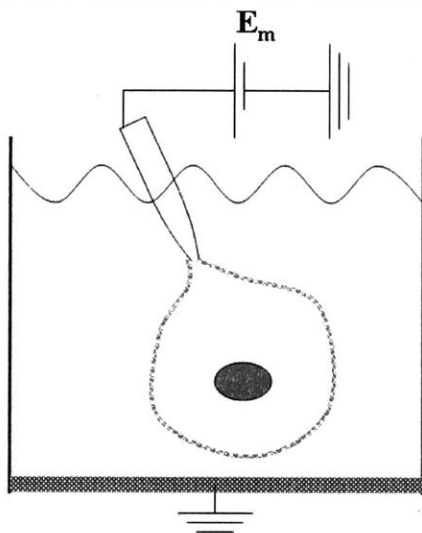


Figure 5: Patch Clamp Diagram

Conducting patch clamp experiments is labor intensive and relatively slow. The process of sealing the glass pipette to the membrane is difficult and requires a trained technician. Studies show that at best, patch clamping is capable of screening one compound a day per technician per workstation [26]. The resulting high cost per compound drives patch clamp studies towards the end of the drug discovery process, when only a small library of “hit” compounds remains.

An issue of great concern with patch clamping is the blocking of irrelevant ion channels using toxic compounds. Eliminating supplemental ion channel activity greatly affects the response mechanisms of a cell. Even with extremely efficient channel blockers, background leak currents remain and are often difficult to separate from the target current. Actual cellular response under normal conditions is difficult to predict using patch clamp data alone.

Efforts have been made over the past decade to automate patch clamping for high throughput applications. Recent years have seen the commercial release of such systems as the PatchXpress 7000A (Qpatch,) and IonWorks HT (Molecular Devices) [27, 28]. While greatly streamlining the process, these systems are expensive and retain the general limitations of patch clamp analysis [28, 29].

I.2 – Optical Ion Sensors (Optodes)

I.2.1: Optode Development

The early 1950's saw the introduction of a new type of electrically based ion-sensor referred to as an Ion-Selective Electrode (ISE). The principle component of an ISE is the ion-selective polymer membrane that separates the sample solution from reference solution. The polymer is able to create a phase boundary potential that is directly correlated to the activity (proportional to concentration) of a particular ion in the sample solution. As various forms of ISEs were developed (K⁺, Na⁺, etc), the technology was expanded on to create an optically based ion-selective polymer [30-33]. This new sensor type was referred to as an optode. Instead of using phase boundary potential, bulk optodes extract ions into the organic polymer phase, which results in a change in optical properties (absorbance, fluorescence, refractive index) [34].

An optode is a polymer matrix containing three lipophilic¹ chemical components. Certain forms of optodes use additional compounds, but they will not be examined in the scope of this report. Optodes operate using the concept of electroneutrality within the polymer phase. Electroneutrality dictates that the polymer phase must retain a constant charge at all times. Any charged particle that enters the polymer phase must be exactly balanced by the co-extraction or expulsion of another charged particle. Through this process, optodes measure the activity of a target ion based on the activity of a secondary ion, usually hydrogen. It must be noted that all properties related to optode response are related to ion activities rather than concentrations. This is a result of thermodynamic equilibrium constraints [35, 36].

The core of an optode is the polymer matrix that allows selective ion transport. For the system to function properly the polymer matrix must allow ion diffusion at a reasonable rate. To achieve this, it is critical that the polymer remain above its glass transition temperature. Several polymers have been employed in optodes that naturally exceed their glass transition temperature at room temperature [37]. However, it is often necessary to plasticize the polymer using components such as bis(2-ethylhexyl) sebacate (DOS) or o-NPOE. The most popular matrix used for both ISE and optode membranes is Poly(vinyl chloride) (PVC) plasticized with DOS. It has strong charge neutrality characteristics and fast ion diffusion rates. To this day it remains the optode matrix of choice for many applications [34]. In this report, all optode matrices consist of PVC plasticized with DOS.

¹ Lipophilic: Lipophilic species tend to be electrically neutral or non-polar (oily)

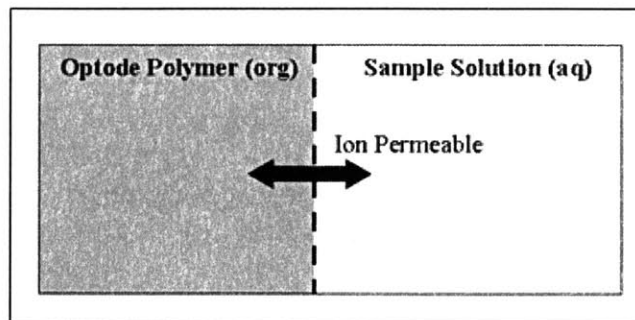


Figure 6: Simple Diagram of the Optode/Solution Interface

An optode in contact with a solution can be thought of as an organic phase and an aqueous phase separated by an ion permeable boundary [34]. Since the organic phase is lipophilic, ions will not passively enter the polymer. The purpose of the components within the polymer is to extract ions into the organic phase in a manner directly correlated with the ion activity in the sample solution.

I.2.2: Response Mechanism

To explain the mechanisms of optode response, a single type of optode will be examined. This type of optode will be used exclusively for the remainder of the report. It contains three lipophilic components and is selective for cations only. The three components are a negatively charged additive, and a neutral ionophore and chromoionophore (in basic form). The theory behind this type of optode is directly amenable to other forms with only minor modifications to the response equations (charges ionophores, anionic target, etc.). The components used for this optode are listed in Table 3 below.

Component	Purpose
(-) Additive	Negative charge sites in the polymer phase
Neutral Chromoionophore (Basic)	Optical measure of pH within polymer phase
Neutral Ionophore	Binds target ion

Table 3: Primary Active Components of an Optode Membrane

An ionophore is defined as a lipid soluble substance that allows ions to move across or into a membrane. In this particular type of optode, the ionophore is an electrically neutral compound that forms a complex with the target ion. Many of the early ionophores used for both ISEs and optodes were antibiotics. As development progressed more effective ionophores were discovered, such as Valinomycin, which has a

strong affinity for potassium [30, 32]. The ionophore is optically inactive in the visible spectrum and does not change absorbance or fluorescence depending on its state of complexation. Every ionophore/ion complex has a stability constant β_{ILn} , which has a direct effect on the lower detection limit of an optode. This can be seen in Equation 8 below. Strong stability constants allow the optode to detect low levels on target ion activity in solution. More information on ionophores and their properties can be found at [34, 38, 39].

A chromoionophore is an ionophore that changes its optical properties in the visible spectrum depending on the state of complexation. In the case of bulk optodes, chromoionophores are usually proton sensitive dyes that change absorbance (and fluorescence in many cases) depending on its degree of hydrogen complexation (protonation). Many existing popular pH sensitive dyes (such as fluorescein) are hydrophilic and quickly leach out of the polymer phase into the sample solution. This limits the library of pH sensitive dyes to ones that are highly lipophilic. Virtually all optodes in use today employ some form of a Nile-Blue derivative. These dyes have excellent performance characteristics in absorbance mode, but have relatively low quantum efficiencies (weak fluorescence). As with the ionophore, the pKa of the chromoionophore in the organic phase has a direct effect on the sensitivity of the optode.

The additive can be any inert lipophilic component that has a negative charge associated with it. Its only purpose is to imbed charge sites within the polymer, which essentially helps to enforce charge neutrality within the optode film. This allows the polymer to carry an equal amount of positively charged particles as additive. The concentration ratio of additive to chromoionophore is usually 1:1. This allows the chromoionophore to become completely protonated or de-protonated. If there is excess chromoionophore with respect to additive, full protonization cannot be achieved. In some situations, this may be beneficial, but for the optodes used in this report, it is never of practical use. In the following report the primary additive employed is potassium Tetrakis[3,5-bis(trifluoromethyl)phenyl]borate (KTFPB). The lipophilic anionic component TFPB- molecules are retained by the PVC and the potassium ions are either complexed by the ionophore, or expelled into the sample solution through diffusion.

Once the above components are dissolved into the polymer phase and exposed to the sample solution, the optode becomes active. It now continuously extracts or expels analyte cations depending on ion activity in the sample solution. With zero target ions, the optode must remain completely de-protonated to achieve charge neutrality (assumes 1:1 additive-chromoionophore ratio). As the target ion concentration increases (increasing activity), the ionophore extracts these ions into the optode. To maintain charge neutrality, hydrogen ions are stripped from the chromoionophore and expelled into the sample solution. This process is depicted in Figure 7 below.

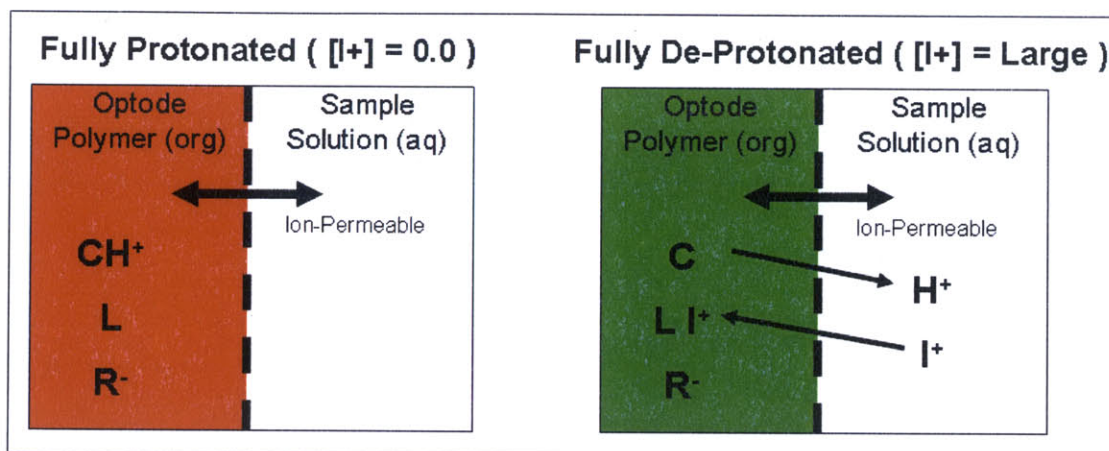
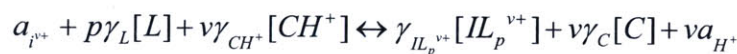


Figure 7: Optode/Solution Interface with Ion Extraction

The theoretical framework for ISEs was accurately defined soon after their development. As optodes were being discovered, existing ISE concepts were adapted in an attempt to describe the behavior of bulk optodes (Nicolosky-Eisenman selectivity formalism). These attempts were able to predict general response characteristics, but there were obvious experimental discrepancies. It wasn't until 1992 that Bakker and Simon developed suitable theoretical equations to describe bulk optode behavior [40, 41]. The following equations (3-12) review their theoretical work, which has been validated by countless experimental reports [42, 43].

The ion-exchange equilibrium between optode and aqueous sample phases can be described by Equation 3 with the resulting exchange coefficient defined in Equation 4.



Equation 3: Ion Exchange Equilibrium

$$K_{ex}^i = \frac{(a_{H^+})^v}{a_{i^{v+}}} \left(\frac{[C]}{[CH^+]} \right)^v \frac{[IL_p^{v+}]}{[L]^p} = \frac{\kappa_{i^{v+}}}{(\kappa_{H^+})^v} \left(\frac{\gamma_{CH^+}}{\gamma_C} \right) \left(\frac{\gamma_L}{\gamma_{IL_p^{v+}}} \right)^p \beta_{IL_p^{v+}} (K_a)^v$$

Equation 4: Exchange Coefficient

The exchange coefficient, K_{ex}^i will determine the overall selectivity of the optode towards the target ion. As shown in the above the equation, there are several constants unique to every ionophore / chromoionophore combination that will influence this value. The two primary parameters are the acidity constant of the chromoionophore K_a , and the

stability constant on the ionophore β_{ILn} . Both parameters are described by the following set of equations.

$$\kappa_{H^+} = \frac{\gamma_{H^+} [H^+]}{a_{H^+}}$$

Equation 5: Hydrogen Activity Ratio

$$\kappa_{I^{v+}} = \frac{\gamma_{I^{v+}} [I^{v+}]}{a_{I^{v+}}}$$

Equation 6: Target Ion Activity Ratio

$$K_a = \frac{[H^+][C] \gamma_{H^+} \gamma_C}{[CH^+] \gamma_{CH^+}}$$

Equation 7: Acidity Constant of the Chromoionophore

$$\beta_{IL_p^{v+}} = \frac{[IL_p^{v+}] \gamma_{IL_p^{v+}}}{[L]^p [I^{v+}] \gamma_{I^{v+}} (\gamma_L)^p}$$

Equation 8: Stability Constant of the Ionophore

The exchange coefficient is extremely important to the performance of an optode because it defines the midpoint of the dynamic range. A larger exchange constant makes the optode more selective for the target ion; therefore promoting lower detection limits. Manipulating this constant can be a very powerful tool to optimize an optodes response in various environments (pH and target ion concentration). One of the simplest techniques utilized to alter the exchange coefficient is to use chromoionophores with various acidity constants [44, 45]. This method is used to reduce the sensitivity of K-Optode I described in Section 1.2.

At this point, it is necessary to define a new variable, α , which represents the ratio of protonated chromoionophore to un-protonated chromoionophore. It is the standard method used to normalize the optical response of an optode between zero and one. Since optodes can function using spectral changes in both absorbance and fluorescence, α can be defined using the two equivalent formulas below for single peak analysis.

$$\alpha = \frac{A_p - A_d}{A_p - A_d} = \frac{F_p - F_d}{F_p - F_d}$$

Equation 9: Degree of Protonization

For a dual-peak chromoionophore, there are several accepted ways to measure alpha [45]. For this report, only two of these techniques will be employed. The first method, as defined by Equation 9, uses only the intensity of a single peak. Maximum and minimum intensity values are determined by peak intensity measurements when the chromoionophore is in its basic and acidic forms. The second method of analysis involves dividing the intensities of each peak by each other ($I_1 / I_2 = \text{Ratio}$). This method is referred to as ratiometric analysis. Using an intensity ratio has clear advantages since it eliminates the effects of polymer movement and volume change. It also reduces the effects of photo-bleaching; however, studies show that photo bleaching may still cause minor interference even with ratio-metric analysis [46].

Equation 3 through Equation 9 can now be combined with electro neutrality and mass balance constraints to develop a formal equation governing the optical response of an optodes with respect to target ion activity (or concentration). This final formalism is defined by Equation 12 below.

$$[R_{tot}^-] = [CH^+] + v[IL_p^{v+}]$$

Equation 10: Charge Balance

$$[L_{tot}] = [L] + p[IL_p^{v+}]$$

Equation 11: Mass Balance

$$a_{i^{v+}} = \frac{1}{K_{ex}^i} \left(\frac{\alpha a_{H^+}}{1-\alpha} \right)^v \frac{[R_{tot}^-] - (1-\alpha)[C_{tot}]}{v \left([L_{tot}] - \frac{p}{v} \{ [R_{tot}^-] - (1-\alpha)[C_{tot}] \} \right)^p}$$

Equation 12: Optode Response I

For this application, both the ionophore complexing coefficient (p) and the target ion charge (v) are both unity. In addition, the activity constants for hydrogen and the target ion can be combined with the exchange coefficient to define an equivalent formula in terms of concentration rather than activity (Equation 13). This simplification will be used throughout the duration of this report since all ion levels are reported in concentration.

$$\frac{[[I^+]]}{[[H^+]]} = K_o^i \left(\frac{\alpha}{1-\alpha} \right) \frac{[R_{tot}^-] - (1-\alpha)[C_{tot}]}{[L_{tot}] - \{ [R_{tot}^-] - (1-\alpha)[C_{tot}] \}}$$

Equation 13: Optode Response II

Many of the parameters in the above equation can be calculated during membrane fabrication, but the ion exchange coefficient, K_o^i is usually determined experimentally. A sample log plot of Equation 13 with typical component concentrations is shown in Figure 8. The curve exhibits a typical Boltzmann sigmoidal shape. The upper and lower asymptotes are fixed at zero and one; therefore the curve can be defined by two parameters, X_o and the Hill Constant.

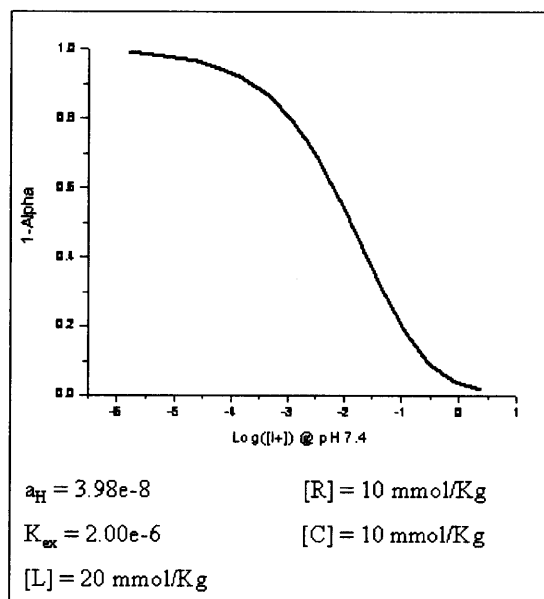


Figure 8: Typical Optode Response Curve

X_o is usually used to denote by the X-axis value where the curve is half way between its minimum and maximum values (in this case, $\alpha = 0.5$). It is also the inflection point of the curve where the second derivative changes sign. It is a general measure of curve shift along the x-axis. In pharmacological dosing applications, this point is referred to as the IC50 or EC50 (effective concentration). With an optode, X_o is a measure of selectivity towards the target ion. At this point, the curve will also attain the steepest slope. To achieve optimal ion sensitivity the optode should be designed to operate at concentrations as close to X_o as possible. The ion exchange coefficient K_o^i has a direct linear 1:1 relationship with this parameter. Component concentrations such as $[R]$ and $[L]$ also affect X_o , but in a highly non-linear manner.

The Hill Constant is an inverse measure of response curve slope at the inflection point (X_o). If the slope is small, the optode will have a large dynamic range, but will lack sensitivity. Conversely, a larger slope will yield high sensitivity and a reduced dynamic range. In the case of both p and v equaling one, component concentration ratios are the only parameters that influence the Hill Constant.

To assess the effects of altering various component concentrations on optode response, a basic sensitivity analysis was performed. Figure 9 shows the theoretical effects of changing various component concentrations and values.

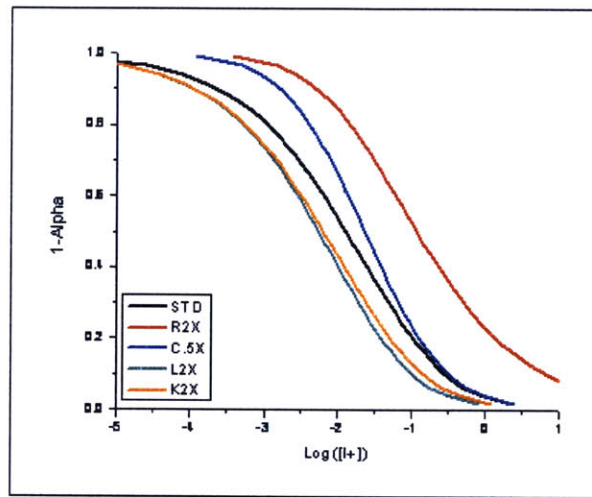


Figure 9: Sensitivity Analysis for Optode Response

The black trace represents optode response with standard component concentrations. It is used as a reference curve to investigate the affects of altering component levels (2:1:1 – L:C:R). Doubling the ionophore concentration, shown by the green curve, increases optode affinity towards the target ion (increased selectivity). The resulting curve is shifted to the left by about half a decade. The curve also increases its slope at the inflection point, which will result in increased optode sensitivity. A similar effect is generated by doubling the value of the exchange coefficient, shown by the yellow trace. Both techniques are effective in increasing overall optode selectivity towards the target ion.

One of the more drastic response changes results from doubling the additive concentration, represented by the red curve. The sensitivity and slope of the response curve become highly reduced. The X_o value has been increased by over a decade and the dynamic range is extended. In practice, it is rarely required to decrease an optode's selectivity and sensitivity.

In some applications, it is necessary to increase optode sensitivity around a particular concentration. This is exactly the case when detecting extracellular ion flux, so this concept is highly relevant for this report. One of the most efficient ways to accomplish this is to reduce the chromoionophore concentration in the polymer phase. This effect is depicted by the blue curve in Figure 9. In fluorescent applications, this will reduce intensity, but will dramatically increase sensitivity and resolution. This same effect can be generated by doubling additive and ionophore concentrations, which will retain fluorescent intensity, but increase component leaching.

I.2.3: Selectivity

The above theoretical equations assume the chromoionophore is exclusively selective for protons. Even at low pH values, it is given that the chromoionophore will

not bind to other interfering cations. This is a valid assumption since virtually all chromoionophores used in optodes have a selectivity coefficients against interfering cations of over one billion ($\text{Log}(K_H^X) = -10$) [40]. However, ionophores are not as selective. In many cases they have the ability to complex interfering cations with relative ease.

If interfering ions are present in the sample solution, it is necessary to accurately model their effect on optode response. Optodes selectivity towards an interfering positive species (J^+) is defined using an additional selectivity coefficient, K_{ex}^J . It is determined experimentally by measuring optode response to a range of interfering ion concentrations. Once determined, this new coefficient can be used to augment Equation 13.

$$\frac{[[I^+]]}{[[H^+]]} = K_o^i \left(\frac{\alpha}{1-\alpha} \right) \frac{[R_{tot}^-] - (1-\alpha)[C_{tot}]}{[L_{tot}] - \{[R_{tot}^-] - (1-\alpha)[C_{tot}]\}} - K_{ex}^J \gamma_j [[J^+]]$$

Equation 14: Optode Response III

Additionally, the two selectivity coefficients can be divided to obtain a parameter that is a direct measure of an ionophores selectivity towards a target ion over an interfering species. It is denoted by the symbol (K_I^X), where I is the target ion and X is the interfering ion. The log of this coefficient represents the shift in response curves between the two ionic species. Usually, the optode is more selective for the target ion and this number will be negative. The potassium ionophore BME-44, described in section 1.2, has a reported $\text{Log}(K_K^{Na})$ of -3.0, indicating the ionophore is 1000 times more selective for potassium over sodium [47].

1.2.4: Sensitivity, Resolution, and Dynamic Range

The sensitivity of any sensor is defined as the change in output produced by a unit change of input. For an optode, sensitivity is the change in optical properties of the membrane (α) created by a change in target ion concentration. This can be calculated by taking the slope of the response curve at any particular concentration. Since the optode response curve is highly non-linear, as shown in Figure 3, the sensitivity is unique at every point. At best, the curve can be approximated with a log-linear relationship in concentration regions around X_o . In this report, optodes are used to measure small changes in ion concentration with respect to equilibrium levels. By linearizing the response curve at a particular concentration, it is possible to estimate optode sensitivity. This theory will be used in Section 1.5.4 to estimate the sensitivity of two optodes using experimentally generated response curves.

The resolution of an optode is the smallest detectable change in ion concentration. Since the resolution is also directly coupled with sensitivity (output/input), the resolution will also be unique at every point along the response curve. On a theoretical basis, optodes will change their optical signal (α) with the release or uptake of a single proton. Under typical operating conditions, optodes typically extract millions of target

ions throughout its response range; therefore it may be considered an analog sensor. The resolution of an analog sensor is typically defined by the sensitivity and background noise level.

Assuming the sensitivity can be determined through linearization, the resolution of an optode can be defined by Equation 15.

$$R_{opt} = \frac{F_s}{S_{opt}(SN)}$$

R_{opt} = Optode Resolution (Moles Target Ions)
 S_{opt} = Optode Sensitivity ($d\alpha/d[I^+]$)
 SN = Signal to Noise ($\alpha/d\alpha$)
 F_s = Noise Factor

Equation 15: Optode Resolution

SN is the signal to noise ratio of the optical signal generated by the optode. Depending on the experimental setup, this value typically ranges from 10 to 1000. The parameter F_s is lowest acceptable signal to noise ratio. If F_s is three, the resulting change in alpha must be at least three standard deviations of the background noise. F_s is entirely determined by the application. If ultra-high resolution is required, as in Chapter 4, F_s may set to less than one; however, noise filtering is required post-processing to attenuate background noise.

The dynamic range on an optode is directly coupled with its sensitivity (assuming sigmoidal response). As the maximum slope of the response curve increases, the dynamic range is reduced. There have been several reported methods to determine the exact upper and lower detection limits. A common technique, which will be used in this report, is to define the detection limits as the points where the slope of the response curve reaches half its maximum value.

1.2.5: Reversibility

The reversibility of an optode is entirely reliant on the chemical properties of the ionophore and chromoionophore. For certain ionophores, the binding kinetics are slow with respect to diffusion. In these cases an optode may not be entirely reversible within a desired time span. All three optode matrices discussed in this report are not limited by binding kinetics; therefore, the theory of reversibility will not be discussed. Detailed information regarding optode reversibility can be found in [34].

1.2.6: Dynamics

With the exception of extremely thin membranes, optode response time is primarily determined by ion diffusion through the polymer. The dynamics of this process follow standard diffusion equations. Many optodes have a thickness (relativity constant)

which is small compared to the diameter or width (D/T ratios in excess of 5,000). This permits modeling an optode membrane as a constant thickness slab. Assuming a uniform diffusion coefficient, Ficks Diffusion Law can be employed to solve for the time rate of diffusion through the polymer, as shown by Equation 16. Also shown is an equation predicting the time required to achieve a 95% optical change (t95%) [34].

$$\alpha(t) = \alpha(\infty) - [\alpha(\infty) - \alpha(0)] \frac{8}{\pi^2} \sum_{m=0}^{\infty} \frac{1}{(2m+1)^2} \exp\left(-\frac{(2m+1)^2 \pi^2 D_m t}{4d^2}\right)$$

D_m = Mean Diffusion Coefficient

d = Membrane Thickness

$$t_{95\%} = 1.13 \frac{d^2}{D_m} \text{ (95 \% Optical Response Time)}$$

Equation 16: Optode Dynamics (Thin Slab)

The diffusion constant for PVC plasticized with DOS has been estimated to be approximately 10⁻⁸ s/cm² (source). Under this assumption, the 95% response time for a 1.0 micron thick optode is approximately 1.13 seconds[34].

1.2.7: Component Leaching

Despite being primarily lipophilic, many common optode components have the capacity to leach out of the membrane over an extended period of time. The rate of leaching is usually slow with respect to common exposure times, but its effect can still be influential on sensor response. The theoretical framework detailing component leaching has been accurately documented [34], but will not be explained in the scope of this report since it was never observed to effect optode performance. It should be noted; however, that increasing component weight percents over 1% will dramatically increase leaching time.

1.2.8: Optode Limitations

Optodes are extremely effective ion-sensors; however, they have inherent limitations that must be addressed. The most notable of these drawbacks is ionophore selectivity for interfering ions. If interfering ions exist in the sample solutions at relatively high concentrations, it is essential that the ionophore be sufficiently selective over this interfering ion. If not, cross-sensitivity will be a major problem and effect experimental results.

With fluorescent chromoionophores, optodes can suffer from photo-bleaching under high-powered excitation light. Photo-bleaching is a common problem with any fluorescent dye, not just optodes [48, 49]. This is usually avoided by reducing excitation power, but for certain applications this is not an option. If the sample has low emission intensities, it is necessary to increase excitation power to achieve acceptable signal to

noise levels. Post processing can usually be employed to subtract photo-bleaching through curve fitting and reference data subtraction. If the dye has two emission peaks, ratiometric analysis can also be employed to reduce these effects. However, studies have shown that photobleaching is not always constant across the entire emission spectra [46]. In these cases even ratiometric analysis will still show residual interference from photo-bleaching.

Due to their response mechanisms, optodes are highly pH sensitive. In many biological applications the pH is relatively fixed, but cellular activity can cause small pH fluctuations. Without adequate buffering, these pH changes will ultimately cause an undesirable optode response. To combat this problem, all sample solutions used in this application are highly pH buffered with Tris or HEPES.

I.3 – Novel Optode Based Assay Systems

I.3.1: Assay Descriptions

The following report introduces a series of novel optode-based whole cell assays. The technology is capable of non-invasively monitoring extracellular ion flux from a large population of cells, which have the ability to replace or augment traditional high throughput drug screening assays. These systems have strong applications throughout many areas of drug discovery including lead compound identification and toxicity screening (hERG). They are capable of accurately detecting several relevant biomarkers not possible with existing technology.

The assays detailed in Chapters 2 and 3 utilize optode membranes to measure extracellular ion flux from whole cells in standard 96- or 384-well plates. These assays are very flexible and can be used with virtually any cell line and drug compound. The vast majority of drug-receptor interactions result in some form of ion signaling. Depending on the nature of the receptor, the ion signaling signatures will be unique. By monitoring the key biological ion currents (sodium, potassium, and calcium), it is possible to develop cataloged “fingerprints” for various forms of cellular response. This will yield extremely high content information on how a particular compound affects cellular activity. Due to its accurate measure of biological activity, these assays have the potential to produce less false-positive and false-negatives in the screening process, which will drastically increase the efficiency of the entire drug development process.

Chapter 4 introduces a specialized system that is capable of field stimulating excitable cell lines and simultaneously measuring the resulting extracellular potassium fluctuations. This is accomplished by positioning ultra-thin optode membrane just microns over a monolayer of cells. These fluctuations are a result of potassium efflux during cell repolarization. Arrhythmic compounds such as Dofetilide and Haloperidol can target and block potassium channels, which will cause a reduction in fluctuation amplitude.

By mapping potassium flux during an action potential, the toxicity of possible arrhythmic inducing compounds can be accurately evaluated. Most importantly, this system allows the cells to function in a natural environment. This is not possible with existing patch-clamp techniques. Work is currently being done to incorporate this technology into 96-well and 384-well plates for high throughput capability.

I.3.2: Advantages over Current Techniques

The assay technologies developed in this report have distinct advantages over current methods. The Heisenberg Uncertainty principle states that it is impossible to measure a system without affecting it in some manner. Cells are highly complex biological systems and are easily affected by foreign matter. This represents a substantial problem with many existing high throughput assays. The vast majority of current biomarker sensors are fluorescent dyes that load into the cell. The most popular of these are voltage and calcium sensitive dyes. They have a variety of documented adverse effects, which include but are not limited to, protein binding, cytotoxicity, free radical release, and ER loading. Any one of these side effects can dramatically alter cellular response mechanisms and reduce the reliability of the assay.

In particular, patch clamping, which is the gold standard for hERG screening, is extremely invasive with an abundance of unwanted side effects. As described in Section I.1.4, patch clamping reduces the cell to a single family of voltage gated ion channels. Any additional cellular systems are eliminated from the analysis.

By using extracellular optodes for biomarker detection, the assays in this report have little to no adverse cellular side effects. The optodes do extract a small number of ions into the polymer membrane, but nothing that would produce significant changes in extracellular concentration. The cells are allowed to operate in a natural environment. In addition, optodes are very robust sensors by nature. Therefore virtually all irreproducibility in this new assay is traced to the cell density and viability, which are inherent in all whole cell assays.

I.3.3: Disadvantages over Current Techniques

Although the assay technology described in this report offers advantages over existing assays, there are some inherent drawbacks. The most substantial of these limitations is the significant buffering of extracellular ion levels. Intracellular calcium dyes (Fluo-4 for example) are detecting changes in concentration up to three orders of magnitude ($10^{-9} \rightarrow 10^{-6}$ M). These large changes eliminate the need for these dyes to be highly sensitive. Conversely, anticipated changes in extracellular potassium and sodium levels are much smaller ($\sim 10\% \rightarrow 0.1\%$), depending on the extracellular fluid volumes. This requires the sensors to be highly sensitive and will inevitably reduce the signal to noise levels of the detection system.

An additional drawback to the assays developed in this report is the need for large a population of cells. Patch clamping, for example, only requires a single viable cell to perform the required analysis. The assays in this report are measuring ion flux in a large volume of fluid, which requires extremely large populations of cells that are all viable and uniform. Therefore, if a percentage of the cell population is dead or not functioning properly, the assay will yield false data. This limitation dictates that cell counts and viability are critical to assay performance.

Chapter 1 - Optode Development

This chapter details the adaptation of three previously reported optode matrices. Two are selective for potassium and the third is selective for sodium. Section 1.2 describes the process used to select the active components for each of these optodes. The following sections describe their experimental performance in comparison with theoretical expectations. These sections also contain fabrication techniques and experimental methods. All three optodes proved to be extremely robust sensors for their respective ions.

1.1 – Development of Sodium and Potassium Optodes

1.1.1: Introduction

As described in *1.1.1: Basics of Cellular Ion Signaling*, potassium, sodium, calcium, and chloride are the four primary ions responsible for cellular ion signaling. The assays developed in Chapters 2-4 are intended to measure cellular ion flux through changes in ion concentration in the extracellular environment. Eventually, optodes for each of these ions will be developed and optimized for biological conditions. For the scope of this report; however, only potassium and sodium optodes are explored. Future continuation of this project will explore the use of calcium and chloride optodes in the extracellular environment.

Potassium and sodium optodes have been in development since the introduction of optodes [30, 32]. Their extensive study has led to the discovery of many different ionophore/chromoionophore combinations that yield excellent optode performance throughout various concentration and pH ranges. Their well documented success will help to reduce development time for this application and ensure optimal sensor response characteristics.

In addition to robust optode performance, potassium and sodium fluxes are extremely important with respect to biological response mechanisms. As Chapter 4 will describe, potassium and sodium are the primary ion currents that control membrane potential during an action potential. In addition to biological relevance, extracellular potassium flux will be the easiest to detect of the four primary ions. The intra/extracellular concentration gradient for potassium is very large (~50:1), which means cell de-polarization will cause a significant increase in extracellular potassium levels.

1.1.2: Component Selection

Several successful potassium and sodium optode matrices have been reported over the last ten years [44, 45, 50]. For this study, several design specifications had to be considered in the selection of optode components. The success of the assays developed in Chapters 2-4 hinges on the performance of these optodes. If the sensitivity or S/N ratios are below required specifications, cellular ion fluxes will be impossible to detect.

For each optode, the inflection point of the response curve should reside around extracellular concentrations for each respective ion. This will maximize sensitivity and resolution. For sodium and potassium, typical extracellular concentrations are approximately 150 mM and 4.0 mM, respectively [2]. To ensure optimal performance, the inflection point of the response curve should not deviate more than half a decade from these values. With any cellular ion signaling, the changes in extracellular concentration are very small. This places high priority on sensitivity over dynamic range.

Most small cation ionophores (ammonium, potassium, sodium, etc) have a strong affinity for each other. Since both potassium and sodium concentrations are relatively high in the extracellular matrix, both optodes need to be highly non-selective for the interfering ion. This will prevent any cross-selectivity or ion interference. $\text{Log}(K_I^X)$ values should be no greater than -1.5 for each ionophore, especially potassium. In addition, the chromoionophore must have exceptional performance characteristics in fluorescence mode. The majority of chromoionophores used in optodes are Nile Blue derivatives. Virtually all have excellent performance characteristics in absorbance, but only a few have adequate fluorescence properties.

For potassium, two optode formulations were discovered that had reported response characteristics that matched the criteria listed above [44]. Both membranes contained the same ionophore, additive, and polymer, but incorporated different chromoionophores (Chromoionophore II and Chromoionophore III). The pK_a difference between the two is approximately 3.7, so the two response curves should be shifted by approximately 3.7 on the $\text{Log}([I^+])$ axis. The report indicated the inflection point for these matrices resides on either side of standard extracellular potassium levels (4.0 mM @ pH 7.4) [44]. Only experimental data will yield the exact exchange coefficients for each optode matrix. This will decide the appropriate optode matrix to be used with the assays developed in this report. Optode components and concentrations according to Shortreed, Durado, and Kopelman are shown in Table 4 below.

K-Optode I					
Item	Code	Name	FW (g/mol)	mmol/Kg	wt %
Ionophore	BME-44	Potassium Ionophore III	967.06	22.4	2.2%
Chromoionophore	ETH 2439	Chromoionophore II	733.98	10.1	0.7%
Additive	KTFPB	Potassium Tetrakis[3,5-bis(trifluoromethyl)phenyl]borate	902.31	10.1	0.9%
Polymer	PVC	Poly(vinyl chloride)	NA	NA	32.3%
Plasticizer	DOS	bis(2-ethylhexyl) sebacate	NA	NA	63.9%
K-Optode II					
Item	Code	Name	FW (g/mol)	mmol/Kg	wt %
Ionophore	BME-44	Potassium Ionophore III	967.06	19.9	1.9%
Chromoionophore	ETH 5350	Chromoionophore III	569.86	10.1	0.6%
Additive	KTFPB	Potassium Tetrakis[3,5-bis(trifluoromethyl)phenyl]borate	902.31	10	0.9%
Polymer	PVC	Poly(vinyl chloride)	NA	NA	32.1%
Plasticizer	DOS	bis(2-ethylhexyl) sebacate	NA	NA	64.5%

Table 4: Potassium Optode Component List

All of the components in the above table are commercially available and are relatively inexpensive (Sigma-Aldrich). In addition, Potassium Ionophore III has been studied extensively and is extremely lipophilic with a high selectivity against sodium and other small cations.

Further literature searches revealed a sodium optode cocktail used for micro-sensor applications [45]. Its performance characteristics were ideal, but the suggested ionophore, Sodium Ionophore IV, was very difficult to obtain. As a substitute, Sodium Ionophore VI was incorporated. It has a similar selectivity towards sodium and should not alter the response characteristics dramatically. It also has a strong selectivity against potassium and other small cations. The modified sodium optode components are listed in the following table.

Item	Code	Name	FW (g/mol)	mmol/Kg	wt %
Ionophore	-	Sodium Ionophore VI	662.85	56.3	3.7%
Chromoionophore	ETH 5350	Chromoionophore III	569.86	13.6	0.8%
Additive	KTFPB	Potassium Tetrakis[3,5-bis(trifluoromethyl)phenyl]borate	902.31	14.3	1.3%
Polymer	PVC	Poly(vinyl chloride)	NA	NA	31.4%
Plasticizer	DOS	bis(2-ethylhexyl) sebacate	NA	NA	62.8%

Table 5: Sodium Optode Component List

1.1.3: Theoretical Response

Theoretical optode response can be estimated using seven independent parameters listed in Equation 13. This assumes negligible effects from any interfering ions, which is acceptable for both Potassium Ionophore III and Sodium Ionophore VI. For the above three optode matrices, six of the seven required parameters can be determined prior to testing and are displayed in Table 6.

Parameter	K-Optode I	K-Optode II	Na-Optode I
n	1	1	1
z	1	1	1
[L]	22.4	19.9	56.3
[R]	10.1	10.1	13.6
[C]	10.1	10	14.3
pH	7.4	7.4	7.4
K_o	Unknown	Unknown	Unknown

Table 6: Known Optode Response Parameters

The ability to measure out exact component quantities is extremely difficult. For this reason, the experimental response curves may deviate slightly from the expected theoretical response. The only unknown parameter is the exchange coefficient, which must be determined experimentally. The response curves produced by references [44, 45] can be used to gain an estimate of the exchange coefficient, but true values can only be determined experimentally by least squares curve fitting to actual experimental data sets. Using estimated exchange coefficient data from [44], theoretical response curves were generated using Equation 13 and are shown in Figure 10.

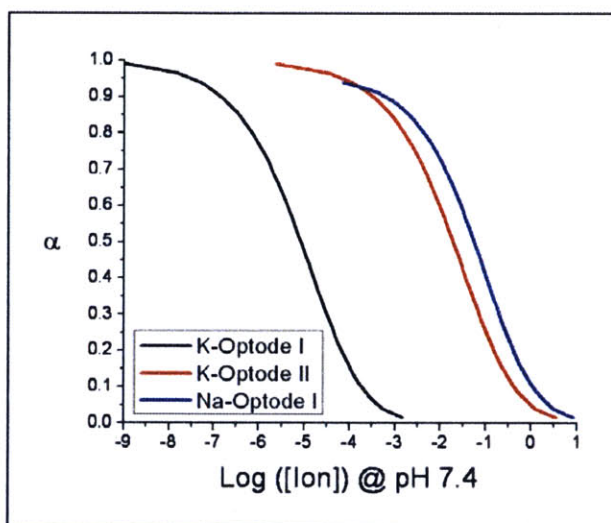


Figure 10: Theoretical Optode Response

As Figure 10 indicates, K-Optode I may be too selective for potassium. Its theoretical inflection point resides around $10 \mu\text{M}$, which is over two decades below typical extracellular concentrations. If this proves to be the case, then K-Optode II should produce a response curve with an estimated inflection point between 30 and 100 mM. These two curves are separated by three decades, which means at least one curve should be log-linear at extracellular concentrations. Only experimental response data will decide the optimal optode matrix to be used for the assays developed in this report.

1.2 – Experimental Methods

1.2.1: Reagents

Optode components included Chromoionophore III (ETH 5350), Chromoionophore II (ETH 2439), Potassium Tetrakis[3,5-bis(trifluoromethyl)phenyl]borate (KTFPB), Potassium Ionophore III (BME-44), Sodium

Ionophore VI, Poly(vinyl chloride) (PVC), and bis(2-ethylhexyl) sebacate (DOS). The plasticized PVC was dissolved in freshly distilled Tetrahydrofuran (THF). All optode components and solvents were purchased from Sigma-Aldrich (St. Louis, MO) at the highest available purities.

Potassium and sodium standard solutions were prepared using salts of the highest available quality (>99%) from Sigma-Aldrich. Calibration solutions were made using serial dilutions in 10mM Tris Buffer at pH 7.4. Trizma-Base was acquired from Sigma-Aldrich and Tris-HCL from ICN Biomedical. On Average, a molar ratio of 8:1 (Tris-HCL : Trizma Base) was required to achieve a pH of 7.4.

1.2.2: Optics

All multi-well plate based optode measurements were performed using the Molecular Devices SpectraMax M2 and Gemini EM plate readers. The SpectraMax M2 was used solely for absorbance measurements through optically clear 96-well plates. Its top-reading optics were inefficient at scanning fluorescent material positioned at the base of the plate. As a result, the Gemini EM was used exclusively for all fluorescence based measurements.

Optode membranes were imaged on 5mm No. 1 glass cover slips with a Carl Zeiss Axiovert 200 inverted fluorescent microscope. Objectives included the Zeiss EC Pan-Neofluar 5X and EC Pan-Neofluar 40X. For effective imaging, optodes were immersed in a 500 mM Trizma-Base buffer solution at pH 12 to ensure a fully basic chromoionophore. Optodes were then imaged using a Rhodamine filter cube.

1.2.3: Optode Membrane Preparation (Various Techniques)

The following methods were used to coat 5mm diameter No. 1 glass cover slips. These techniques should be amenable to virtually any glass or THF resistant polymer substrate. For each technique, all cover slips were first cleaned with THF to remove any organic residue that could contaminate the optode.

Droplet Evaporation

Due to the small size and low weight of the 5mm cover slips, double sided tape or a vacuum chuck was used to immobilize the cover slip. Once secured, between 1 and 5 μ L of optode solution (8-16 mL THF / 100 mg PVC) was applied to the entire surface. The cover slip was then placed in a fume hood and allowed to dry for a minimum of twenty minutes. Similar techniques were used for other substrates, such as the OIM featured in Chapter 3.

Bath Evaporation

A 5mm diameter glass cover slip was placed in the center of a large 25mm X 50 mm glass cover slide. Fifty μ L of dissolved optode solution (8 mL THF / 100 mg PVC)

was applied to the entire surface of the cover slip. Care was taken to ensure the 5mm diameter cover slip remained in contact with the lower glass at all times. The entire setup was then placed in a fume hood and allowed to dry for approximately 120 minutes.

Using a specially modified set of tweezers, the 5mm cover slip was simultaneously rotated and separated from the lower glass. Rotation was required to shear the plasticized PVC joining the two cover slips.

Spray Coating

Spray coating was accomplished using a commercially available bottom feed airbrush (Badger Model 200 NH). This airbrush was ideal for this application due to its small spray cone and finely controllable flow rates. A custom feed tank was fabricated to fit the standard 2 mL glass vials used to store dissolved optode. For optode preparation, 5mm diameter glass cover slips were fixed to a polypropylene backing using standard double sided tape. Typically 10 to 30 cover slips were coated at a single time to ensure uniformity between optodes. This also reduced the volume of wasted optode mixture used to prime airbrush feeds. The spray gun was then connected to 30 PSI shop air and the needle was set to between 0.5 and 2.0 turns out from fully shut. Pure nitrogen was also employed as a carrier gas, which seemed to produce finer particles.

Cover slips were placed at a distance between 5-8 inches from the nozzle and kept at a 45° angle to the airbrush centerline axis. With the above settings, typically 3-4 coatings were applied to achieve optode membranes approximately 5 microns in thickness. A diagram of this process is shown in Figure 11 below.

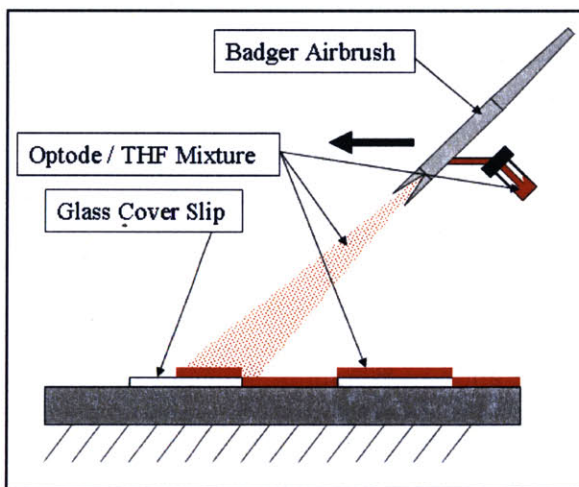


Figure 11: Diagram Showing the Spray Coating Process

Spin Coating

In the laboratory, spin coating was accomplished using a small 3.0 Volt DC motor. A variable resistor was used in series with the motor armature to control shaft speed. A rough diagram of the spinning setup is shown in Figure 12.

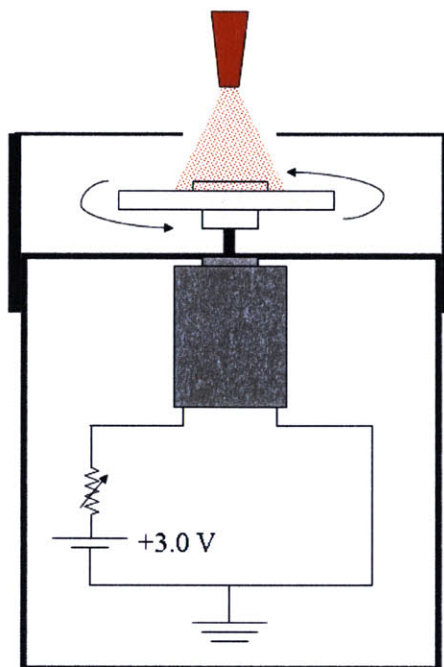


Figure 12: Diagram Showing the Spin Coating Process

A single 5mm diameter glass cover slip was fixed to the motor shaft using a custom nylon adaptor and spun at approximately 2,000 RPM. Once up to speed, 20 μL of optode/THF cocktail (16:1 [mL THF : 100 mg PVC]) was sprayed onto the disk surface using a pipette. After twenty seconds the motor was shut down and the membrane was allowed to dry for an additional twenty minutes. The disk was then imaged using the techniques outlined in Section 1.2.1.

Micro-Sphere Deposition

The process began by creating an optode emulsion. This was accomplished by injecting dissolved optode (16mL THF / 100 mg PVC) into a pH buffered solution that is submerged in a sonicating water bath. Typically, 50 μL of the optode/THF solution was injected into 1,000 – 1,500 μL of buffered solution. The resulting emulsion contained a mixture of spherical optode particles ranging in size from 200 nanometers to 20 microns. One hundred μL of the resulting emulsion was placed in a single 96-well plate well coating a 5mm cover slip. The plate was then centrifuged at 200 g's for 10 minutes. The remaining liquid was then aspirated and the cover slip removed. This was shown to form

a highly uniform optode mesh on the glass surface. Mesh thickness was controlled through solution height and emulsion density.

1.2.4: Calibration Protocol

Standard Cover Slip Calibration

Optodes were pre-conditioned in a 100 mM target ion solution buffered to pH 7.4 for 5-10 minutes and then rinsed with deionized water (18 M Ω). All membranes were then exposed to 500 mM Tris-HCL (pH 4.5) for a minimum of 5 minutes to fully protonate the chromoionophore. Optodes were rinsed a second time with deionized water and carefully placed at the base of a Nunc Optically Clear Black 96 well plate. Each well was filled with 100 μ L of 10 mM Tris Buffer (pH 7.4). At this point, serial additions were performed to increase target ion concentration in each well.

To classify the optical properties of the chromoionophore, it was necessary to perform spectral scans at each concentration in both absorbance and fluorescence mode. After spectral peaks were identified, calibrations were performed using the kinetic scan mode. Typically, optodes were scanned at three wavelengths every 20 seconds for 5 minutes at each concentration, yielding a total of 15 points per wavelength per concentration. For each wavelength, the last 5 points of the kinetic run were averaged together to give a single value. After each kinetic scan (concentration), the plate was ejected and target ion solution was added in the appropriate amount. Typically, the addition sequence was designed to produce a constant increasing logarithmic concentration interval. Note, all calibrations runs in this report were performed at room temperature. A sample addition table is shown below for a potassium optode calibration.

Addition Step #	Volume Added (μL)	Solution #	[K⁺] (mM)
1	100	1	0.000
2	1	2	0.010
3	1.2	2	0.022
4	2.7	2	0.047
5	6.1	2	0.099
6	1.3	3	0.214
7	2.9	3	0.460
8	6.8	3	0.992
9	1.5	4	2.194
10	3.2	4	4.665
11	6.3	4	9.180
12	1.6	5	20.958
13	3.5	5	45.771
14	5.9	5	84.868
15	24	5	215.601
16	80	5	468.633

Solution # 1	0.0 mM KCl
Solution # 2	1.0 mM KCl
Solution # 3	10.0 mM KCl
Solution # 4	100.0 mM KCl
Solution # 5	1000 mM KCl

Table 7: Sample Potassium Calibration Look-Up Table

Optode Insert Module (OIM) Calibration - Chapter 3

This protocol is used to calibrate the optode insert module developed in Chapter 3. It must be noted that the optode insert module is only compatible with fluorescent bottom scanning plate readers. All insert posts were cleaned with THF and optode membranes were formed using the droplet evaporation technique. At this point, the protocol is identical to the cover slips with only one difference. For each fluid addition, the insert had to be taken out of the plate for access purposes. During this step, a fluid droplet remains on the end of each post. It was essential to keep this droplet on the post. Removal caused concentration changes that resulted in a step in the response curve. It was also critical not to hit or damage the optode in any way between additions.

1.2.5: Data Acquisition and Processing

Molecular Devices Softmax Pro 4.8 was used to interface with both SpectraMax M2 and Gemini EM plate readers. For each concentration, wells were scanned using either spectrum or kinetic mode. The resulting data (spectrum or kinetic) was exported as a .txt file. A custom Matlab program was used to extract and process the data produce spectral plots and dose response curves. Data was finally imported into Origin 7 and Graph Pad for advanced plotting features such as Boltzmann curve fitting.

1.3 – Results and Discussion I: Membrane Fabrication Techniques

It is extremely difficult to manipulate plasticized PVC in its natural form under standard conditions (22°C @ 1.0 Atm). Dissolving the optode in an appropriate solvent, such as THF, makes the polymer easier to work with. When dissolved, the optode can be coated onto a variety of substrates using a set of fabrication techniques.

Four popular coating techniques were explored in an attempt to find the optimal optode membrane fabrication method. These techniques included evaporation coating, spray coating, spin coating, and micro-sphere deposition. The following sections discuss each individual technique and comment on their effectiveness. It should be noted that all testing was performed using K-Optode II dissolved in THF (various solvent concentrations).

1.3.1: Evaporation Coating

Evaporation coating is a simple technique that uses only solvent evaporation to deposit a thin optode membrane onto a desired substrate. Evaporation coating can be split into two separate sub-categories that differ only in the initial shape of the liquid mixture. Both techniques are extremely simple to perform with a small number of experimental variables. This technique can coat optode onto virtually any surface permitting it is chemically resistant to the solvent (THF).

Droplet Coating

The first sub-category of evaporation coating is referred to as droplet coating. It involves placing a single droplet of polymer/solvent mixture onto a horizontal substrate. When the solvent completely evaporates, only a thin optode membrane remains. The mixture rarely covers the entire surface of the substrate, which creates a dome shaped droplet. This method is used throughout this report because of simplicity and low preparation time. A strong disadvantage to this method is its inability to create uniform thickness membranes. The curvature of the droplet effects how the polymer is distributed upon evaporation. Non-uniform thickness membranes will not affect steady state optical properties, but can dramatically increase response time.

When a droplet is drying on most common flat surfaces it creates a “ring effect”. The “ring effect” is a thick region of polymer at the perimeter of the membrane. This is caused by polymer driven towards the droplet edge during evaporation from surface tension gradients. As described in 1.2.6: *Dynamics*, optode response time is directly proportional to the square of its thickness. This results in extremely slow response times at the outer portions of the membrane. The theory describing the formation of these uneven coatings will not be described in this report, but experimental results show a clear dependence on the initial surface profile of the dissolved polymer. Figure 13 shows a cross-section of solvent evaporation on a circular disk over time. All figure dimensions are not to scale and the time stamp is only approximate.

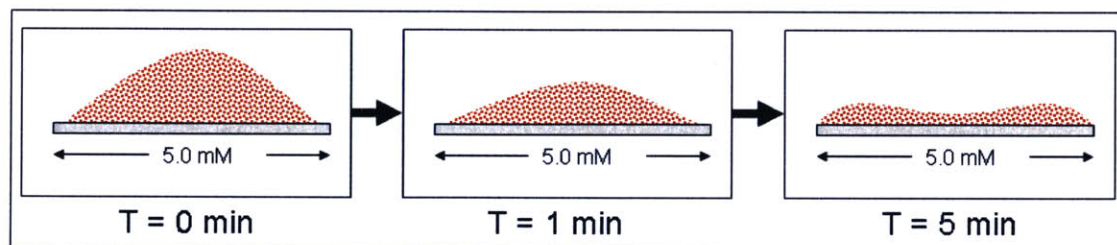


Figure 13: Cross Section of an Optode Droplet Evaporating Over Time

The “ring effect” caused by solvent evaporation was virtually unavoidable despite tuning several fabrication factors. These factors included droplet size, solvent to polymer ratio, increased drying rate, temperature, and even changing the angle of the glass optode during evaporation. The only parameter that had a moderate effect on membrane uniformity was the polymer/solvent ratio.

In a very simple experiment, two optode membranes were formed on 5mm glass cover slips and then compared. The overall mass of polymer was kept constant between optodes, but the initial solvent volume differed by a factor of two at application time. Figure 14 shows the two disks in pseudo color mode. Optode A had an initial PVC/THF (100mg/mL) ratio of 1:8 compared to Optode B, which had an initial ratio of 1:16.

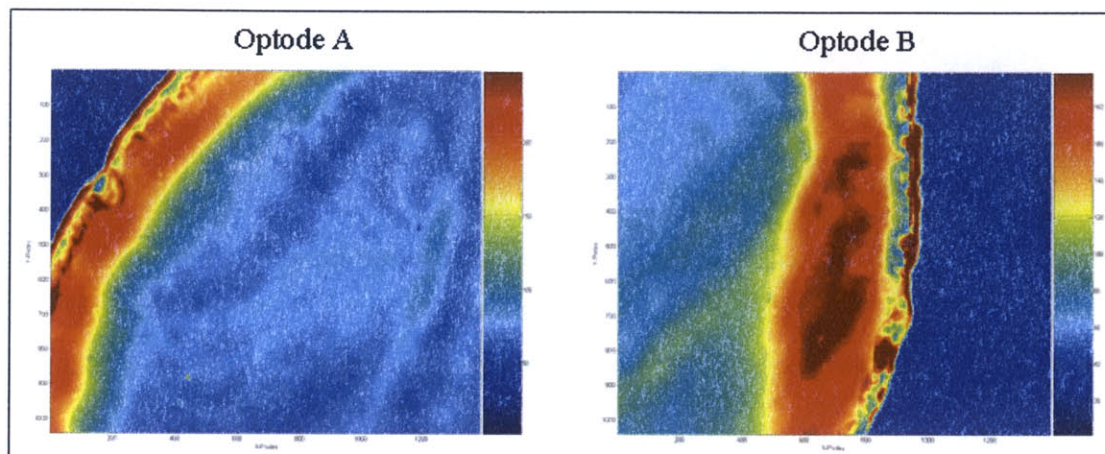


Figure 14: Pseudo Color Image of Two Optode Coated 5mm Glass Cover Slips

Both optodes in Figure 14 demonstrates a clear “ring effect” towards the perimeter of each optode disk. This is indicated by the bright red area, which has a fluorescent intensity over twice that of the center of the disk. Due to the initial high solvent volume in Optode B, a higher percentage of polymer was deposited towards the edge of the disk, which amplified the “ring effect”. This is expected to be a result of the increased droplet departure angleⁱⁱ. These results suggest employing low volumes of solvent to attenuate the “ring effect”. At a certain point, the polymer solvent solution becomes highly viscous and is difficult to apply, which also proved to create non-uniform coatings. In addition, applications requiring ultra-thin optode membrane require using high initial solvent to polymer ratios.

Bath Coating

The second method of evaporation coating consists of submerging the entire substrate in a relatively large polymer/solvent bath. In contrast, the substrate emersion method proved to be highly useful in avoiding any “edge effects” caused by a curved surface profile during evaporation. This was achieved only if the bath diameter or width was large with respect to the surface curvature radius. A rough schematic of this process is shown in Figure 15 below.

ⁱⁱ Departure angle refers to the angle between the substrate and the droplet surface at the interface.

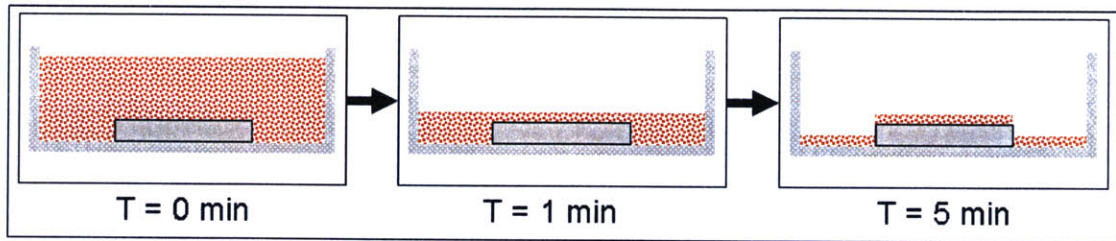


Figure 15: Cross Section of Optode Membrane Fabrication Using Bath Evaporation

To demonstrate the dramatic increase in membrane quality, an optode was prepared and imaged using a fluorescent microscope. Figure 16 shows the resulting pseudo color fluorescent intensity image.

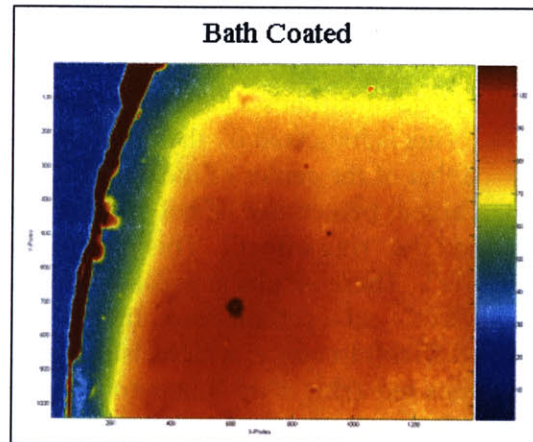


Figure 16: Pseudo Color Image of an Optode Formed with Bath Evaporation

There is a significant increase in membrane uniformity over the droplet method. There is actually an opposite “edge effect”, which is a reduced membrane thickness at the perimeter of the disk. Since this is only present at the very edge, it should not affect overall optode performance. Towards the center of the disk the membrane is far more consistent. The intensity values fluctuate less than twenty percent, which is highly acceptable. This fabrication proved to be effective at producing uniform coatings, but consumed large quantities of unused optode. The unused optode can be re-dissolved, but at the risk of particle contamination.

1.3.2: Spray Coating

Spray coating is a widely used technique to achieve uniform polymer coatings. The most common use for spray coating is the application of paint and other surface

coatings. It has numerous advantages over other methods for the purpose of optode membrane fabrication. A dissolved optode polymer behaves similarly to many typical paint products; therefore, not adverse effects are caused by using optode solutions. Membrane thickness can be accurately controlled through a variety of setup parameters including air pressure, needle valve settings, and polymer/solvent ratios. The process is very high throughput and can accept any shape substrate. A diagram of this process is shown in Figure 11 below. Spray coating is also highly amenable to high throughput optode manufacturing systems. At first glance, spray coating appeared to be a highly promising coating technique.

To investigate the quality of these membranes, a batch of optodes were spray coated and imaged using the protocols outlined in 1.2.3: *Optode Membrane Preparation (Various Techniques)*. The resulting pseudo color fluorescent intensity images are shown in Figure 17.

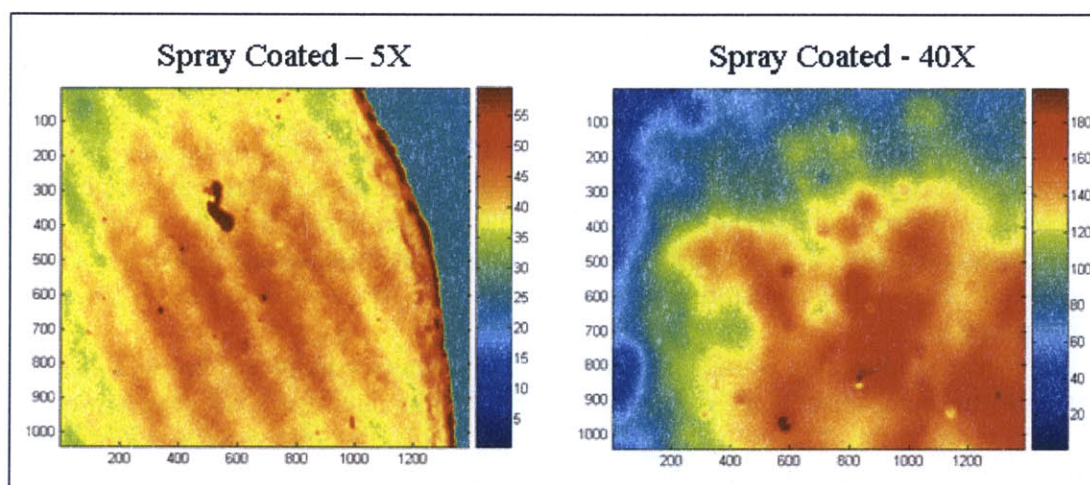


Figure 17: Spray Coated 5mm Glass Cover Slip

The left panel of Figure 17 shows a spray coated optode disk viewed with a 5X objective. Under this magnification, the optode membrane appears highly uniform. The parallel lines are an optical artifact caused by glass-on-glass contact during imaging; it is not a feature of the membrane. Over the entire surface of the disk, the thickness varies less than five percent. This is a significant increase over the evaporation techniques.

Upon further investigation, the 40X objective revealed non-uniform membrane formations. The right panel of Figure 17 shows features that indicate component crystallization or clumping. This phenomenon was more evident when the membrane was imaged using a confocal microscope. It is unclear as to the cause of these features, but their presence may be detrimental to optode performance. Due to this phenomenon, spray coating was not employed as a fabrication technique for the optodes described in this report. Current research has shown that spray coating with pure nitrogen eliminates component clumping, which has allowed spray coating to be a viable fabrication technique.

1.3.3: Spin Coating

As with spray coating, spin coating is a widely used and respected means of fabricating uniform polymer membranes. Membrane thickness is highly controllable since it is directly related to spin speed [51, 52]. Several studies over the past two decades have detailed the physics governing spin coating dissolved polymer. The theory dictates that under perfect conditions, spin coating will produce perfectly uniform membranes. Equation 17 predicts the thickness of a spun coat membrane based on a series of experimental variables [52].

$$h_f = C_o (v_o D_o)^{1/4} \Omega^{-1/2}$$

h_f = Film Thickness

Ω = Spin Speed

Equation 17: Membrane Thickness from Spin Coating

The first three parameters in Equation 17 (C_o , v_o , D_o) represent various fluidic and material properties such as viscosity and surface tension. Many of these are impossible to determine theoretically and must be estimated using experimental data. Despite this, the equation does give a direct power relationship between membrane thicknesses and spin speed. This indicates that membrane thickness can be controlled directly through rotation rate.

These studies also warn against a host of laboratory conditions that will cause non-uniform membranes. One of these parameters is the rate of solvent evaporation from the polymer mixture. The equation assumes that the solvent concentration within the polymer/solvent mixture is uniform. If the solvent evaporates too quickly, a concentration gradient will be created, which will cause “skin” formation. A solution to this problem, used by several sources, is to saturate the atmosphere with solvent vapor while spinning. This will slow evaporation rate and prevent large solvent concentration gradients. Other laboratory parameters that will cause poor membrane formation include non-horizontal spinning, rough substrate surface, and low initial solvent concentration.

Experimentally, spin coating produced the most uniform and easily controllable optode membranes discussed in this report. Its only drawback is the obvious requirement that the surface being coated need to be spun at high RPM. This limits the list of acceptable substrates to individual disks or cylinders, which dramatically reduces throughput of the assay preparation (longer setup times).

The resulting pseudo color fluorescent intensity images using two objectives are shown in Figure 18.

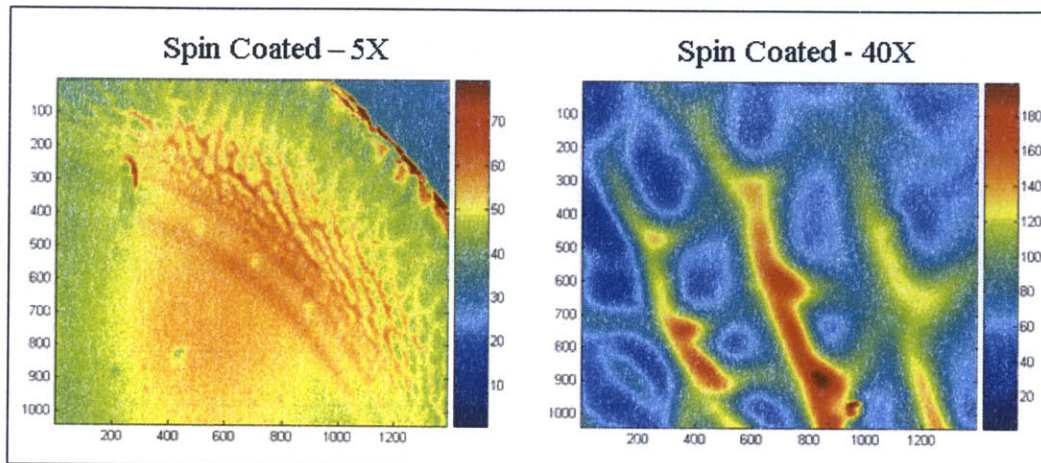


Figure 18: Pseudo Color Images of a Spun Coat 5mm Glass Cover Slip

The left panel of Figure 18 shows the edge of a spin coated 5mm disk imaged using a 5X objective. Overall, the membrane thickness is uniform with fluorescent intensity variations of less than ten percent. The only apparent defect is the slight presence of the “skin effect” towards the perimeter of the disk. This was most likely caused by a high rate of THF evaporation during the spinning process. The effected region is not significantly thicker than the center of the disk, but it displays surface ripples. These ripples were most likely caused by centripetal forces acting on the upper viscous layer during the final stages of solvent evaporation.

The ripples caused by the “skin effect” are better visualized in the right panel of Figure 18, which shows the optode disk imaged using a 40X objective. Under this magnification, the peaks and valleys of the ripples are much more apparent. This phenomenon might increase response time slightly, but this was not observed experimentally. The ripples may actually decrease optode response time by increasing the surface area to volume ratio of the outer region. If desired, the “skin effect” could be eliminated by saturating the spinning chamber with THF vapor during formation.

1.3.4: Micro-sphere deposition

Micro-sphere deposition was used to create a single optode membrane with thousands of small optode particles adhered together to form a mesh-like film. This technique has distinct advantages over the previously described fabrication methods. Virtually any shape or size surface can be coated and the material does not have to be chemically resistant against the optode solvent. This is a result of the optode solvent being highly diluted in the emulsion buffer. Most importantly, the mesh of particles has greater surface area to volume ratios than typical “slab” membranes, which will significantly reduce response time. This technique also has potential to be high throughput with a custom robotic system.

The primary disadvantage to this technique is the additional preparation steps. Of all the above methods, this is the most time intensive to perform in the laboratory. Under high throughput conditions; however, this technique could be efficient with the proper automation systems. Another drawback to these membranes is their lack of durability. It has been observed that even low velocity fluid flow over the mesh surface causes particles to dislodge. Dislodged particles could contaminate the sample and cause a change in optical intensity due to the removal of dye. Extensive drying of the mesh membrane may increase adhesion and make the membrane more robust.

Figure 19 shows two fluorescent intensity images of a 5mm diameter cover slip coated using the deposition technique. Imaging protocols are consistent with the steps outlined in Section 1.2.1.

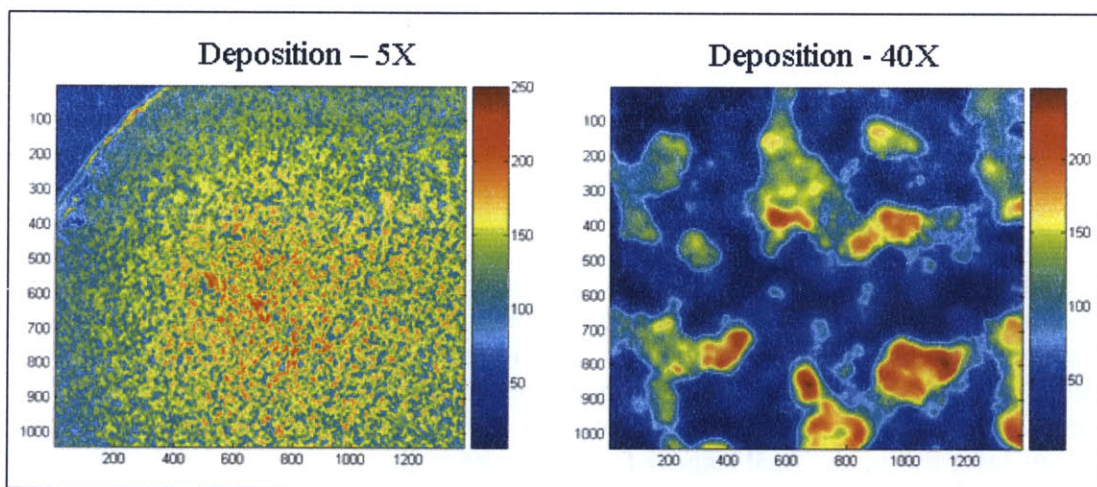


Figure 19: Pseudo Color Image of a 5mm Glass Cover Slip Coated Using Micro-Sphere Deposition

Even using the 5X objective (left panel), the optode particles are clearly visible. Notice the distribution is relatively uniform over the surface of the disk. The only visual defect with this membrane is the absence of particles at the very edge of the disk. These particles were most likely dislodged while extracting the optode disk from the 96-well plated.

The individual optode particles are clearly visible using the 40X objective, as shown by the right panel of Figure 19. The particles in red are deposited on the surface of the cover slip and are in focus. The light blue shadows in the background represent particles in the upper layer of the mesh, which are out of focus. Notice the low particle density throughout the mesh. This should allow adequate ion diffusion through the membrane and further promote rapid sensor response.

1.3.5: Technique Comparison

Every technique discussed above was able to produce fully functional macro-scale optode membranes. In addition, each technique has a unique set of advantages and

disadvantages for the purpose of optode membrane production. Table 8 contains a set of performance properties and the associated best and worst fabrication techniques as determined by laboratory testing.

Parameter	Best	Worst
Low Preparation Time	Droplet Evaporation	Micro-Sphere Deposition
Uniform Membrane Thickness	Spin Coating	Droplet Evaporation
Durability	Spin Coating	Micro-Sphere Deposition
High Throughput Capability	Spray Coating	Spin Coating
Response Time	Micro-Sphere Deposition	Droplet Evaporation
Optode Cost	Droplet Evaporation	Spray Coating
Substrate Flexibility	Spray Coating	Spin Coating

Table 8: Best and Worst Properties of Various Optode Fabrication Techniques

As Table 8 indicates, no single fabrication technique excels over the rest. It is apparent that the fabrication techniques are application specific. For the sensor systems developed in Chapters 2 and 3, the droplet evaporation technique was the most commonly used coating method. This was due to its simplicity and the relaxed design restraints on response time. It was also helpful in conserving expensive optode components. In Chapter 4; however, spin coating was used exclusively to fabricate repeatable uniform thickness optode membranes. This was a result of response time and membrane thickness being a critical factor in optimizing system performance. Overall, the fabrication technique must be tailored to the design requirements of the system.

1.4 – Results and Discussion II: Optode Performance

1.4.1: K-Optode I Response Properties

Reports had indicated that K-Optode I might be an acceptable potassium sensor for extracellular measurements [44]. To assess its performance for this application, the optode was fully characterized using a series of calibrations employing both spectral and kinetic analysis.

Spectral calibrations were performed using both absorbance and fluorescence to fully classify optode response properties. Calibrations were performed according to the protocol outlined in *1.2.4: Calibration Protocol*. Potassium concentration was increased from 4.8 μM up to 39.2 mM at a pH of 7.4. The resulting spectral plots and response curves in absorbance and fluorescence mode are shown in Figure 20 and Figure 21, respectively.

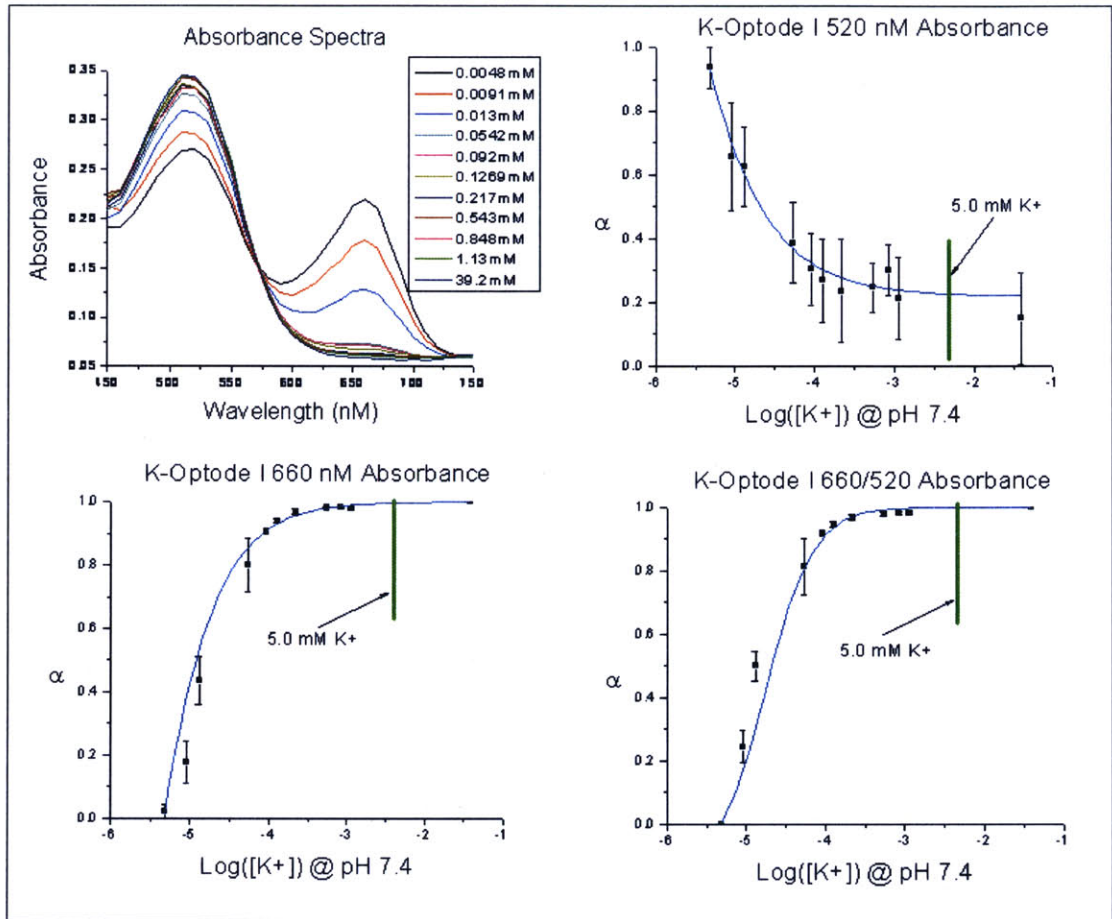


Figure 20: K-Optode I Absorbance Response Properties

The absorbance spectrum in the upper left panel shows classic dual-peak response behavior. The high frequency wavelength peak resides at 520 nm and has low absorbance in the protonated state ($[K^+] = 0.0048 \text{ mM}$). The low frequency peak resides at 660 nm and has high absorbance in the protonated state. As potassium concentration increases, chromoionophore II begins to de-protonate as hydrogen ions leave the optode membrane. This causes the absorbance at 520 nm to rise while the absorbance at 660 nm decreases simultaneously. Notice the absorbance at 570 nm between the two peaks remains constant throughout the entire concentration range. This wavelength is referred to as the isosbestic point. The absorbance at this wavelength remains constant despite changes in chromoionophore complexation. It is commonly used as an internal standard for ratiometric analysis.

Optode response curves using 660 nm single peak, 520 nm single peak, and the 660/520 ratio absorbance were generated using the spectral data from the upper left panel of Figure 20. The resulting plots are contained in the remaining three quadrants. Note raw absorbance and ratios are normalized between zero and one (alpha). All three curves

show a similar response behavior to increasing potassium concentration. Note the lower portion of the sigmoidal curve is not complete. The sensitivity of this optode matrix was underestimated; therefore, the lowest potassium concentration (0.0048 mM K⁺) exceeded the lower detection limit of the optode. Additional response curves would need to be generated to determine the full dynamic range of the optode. Since the upper detection limit is approximately 0.1 mM, this optode matrix is far too selective for use in the extracellular environment. Based on absorbance response properties, K-Optode I cannot be used for the assays in this report.

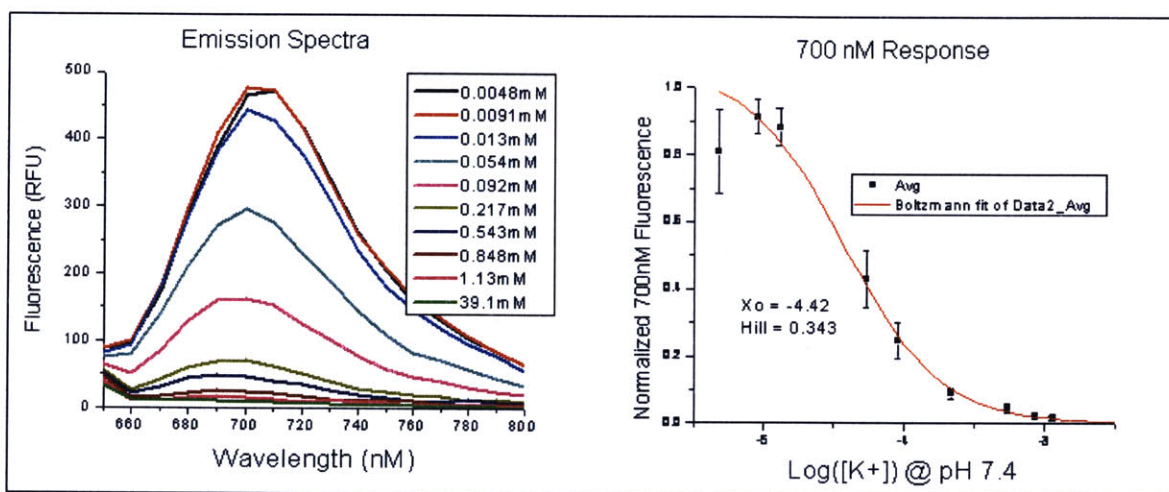


Figure 21: K-Optode I Fluorescent Response Properties

The left panel of Figure 21 shows the fluorescent emission spectrum of K-Optode I throughout the same range of concentrations used with the absorbance analysis in Figure 21. When excited at 640 nm, the emission spectrum for Chromoionophore II only has a single emission peak at 700 nm. Using single peak normalization, the right panel of Figure 21 shows the resulting 700 nm response curve. Consistent with absorbance response curves, the dynamic range for this optode is far too low for typical extracellular potassium detection. The X_0 (EC_{50}) point for both absorbance and fluorescent response curves is approximately 30 μ M. This dictates reducing the selectivity coefficient by over two orders of magnitude. As shown by the following section, increasing the pK_a of the chromoionophore can create such a shift in selectivity.

1.4.2: K-Optode II Response Properties

K-Optode II uses Chromoionophore III, which has a reported pK_a of 12 [44]. This is an increase in pK_a of 3.7 over Chromoionophore II, which means K-Optode II should have an inflection (X_0) point around 30 mM. Theoretically, this optode matrix should be ideal for extracellular potassium measurements.

As with K-Optode I, K-Optode II was fully classified with both absorbance and fluorescence to determine response properties. At this point in the project evolution, optodes were no longer required to operate in absorbance mode. For this reason, only spectral plots will be shown for K-Optode II. The resulting response curves were omitted. The absorbance spectra for chromoionophore III at various states of complexation are shown in Figure 22. The pH of the standard solutions was held constant at 7.4 using a 10mM Tris Buffer.

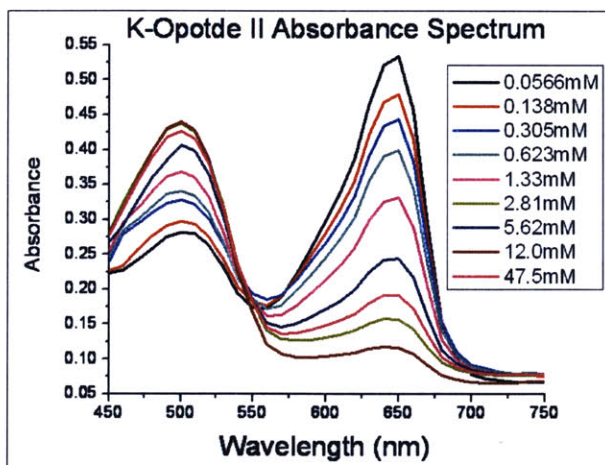


Figure 22: K-Optode II Absorbance Response Spectra

As with K-Optode Matrix I, Chromoionophore III has two absorbance peaks with an isosbestic point between them. The high and low frequency peaks reach their maximum intensities at 502 nm and 650 nm, respectively. The isosbestic point resides at 550 nm. Although absorbance will not be used as a measure of alpha for the assay systems described in Chapters 2-4, the above spectrums indicate excellent dual wavelength behavior. This expands the flexibility of this optode matrix for future absorbance based applications.

Figure 23 shows the results from a fluorescent spectral analysis performed on K-Optode II. Excitation wavelength was set to 485 nm as recommended by Sigma Aldrich. A 500 nm excitation cutoff filter was employed to reduce excitation interference.

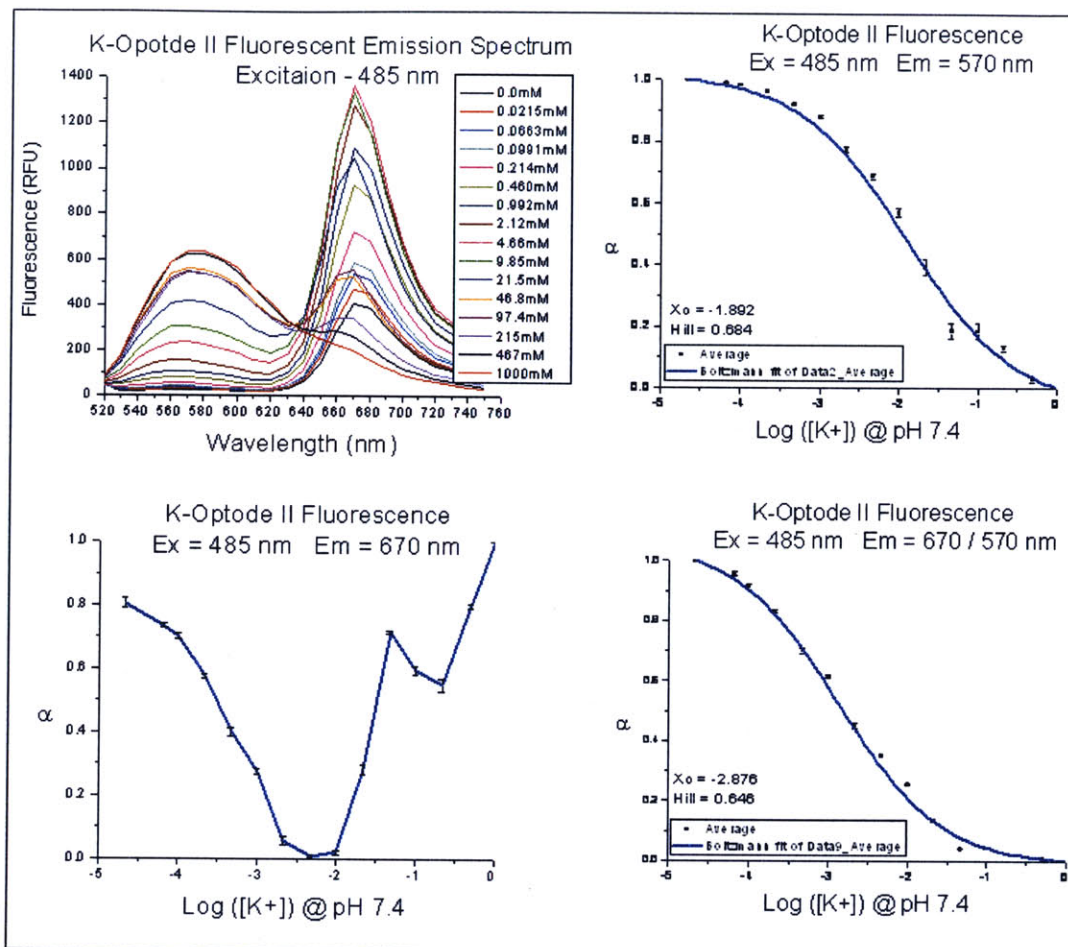


Figure 23: K-Optode II Fluorescent Response Properties

The spectral traces in the upper left panel of Figure 23 show apparent dual peak emission characteristics. As with K-Optode I, response curves were generated using the emission intensities at 570 nm, 670 nm, and the 670/570 ratio.

The high frequency peak resides at 570 nm and reaches maximum fluorescence when the dye is fully protonated. The resulting dose response curve for the high frequency peak is shown in the upper right panel. A least squares sigmoidal curve fit places the inflection point of the curve at 6 mM, which is extremely close to typical extracellular concentrations. This response curve displays classic Boltzmann response behavior with no irregular characteristics. Based on 570nm excitation data alone, this optode is ideal for extracellular potassium measurements.

Conversely, the low frequency peak residing at 670 nm exhibits highly unique response characteristics. As the dye begins to protonate (increasing K⁺ concentration) the fluorescent intensity increases, which is counter to classic dual-emission peak behavior. As one peak rises, the other should fall simultaneously. At a certain point ([K⁺] = 5 mM), the intensity reaches a maximum and the fluorescent intensity begins to

fall back towards its de-protonated level. This “hump” behavior is represented in the 670 nm dose response curve pictured in the lower left panel of Figure 23. Since Chromoionophore III has an extremely wide excitation band, it is likely that emission light at 570 nm is supplementing the plate readers’ excitation source. Details of this behavior will not be explored in this report, but the behavior must be noted.

Surprisingly, when the peaks are divided by each other (ratiometric analysis), the response curve remains relatively sigmoidal as shown in the lower right quadrant of Figure 23. Despite this acceptable response curve, ratio-metric measurements are avoided whenever possible in the remainder of this report.

Despite non-ideal fluorescent characteristics, K-optode II has a selectivity constant that is ideal for extracellular potassium measurements. In addition, the overall fluorescent intensity of Chromoionophore III is relatively high when compared to other Nile-Blue derivatives (Chromoionophore I, II). Based on these two characteristics, this optode matrix was further investigated.

As mentioned previously, Chromoionophore III has a wide excitation band. By exploring other excitation wavelengths, it might be possible to find a wavelength that generates ideal sigmoidal response behavior in fluorescence mode. To investigate this theory, an excitation scan was performed while measuring the emission at 670 nm. The excitation sweep ranged from 450 nm through 650 nm at 10 nm increments. The results showed an approximately linear increase in emission intensity as excitation wavelength approached 650 nm. Based on these results, it would be optimal to excite the dye as close to 670 nm as possible. However, to maintain a reasonable stokes shift^{III}, an optimal excitation wavelength of 570 nm was chosen. Since this wavelength overlaps with the high frequency emission peak, the previously describes cross-excitation phenomenon should be eliminated. The drawback to this method is the elimination of ratiometric analysis, which can be helpful at reducing artifacts from photobleaching and changes in sensor geometry.

To accurately characterize the performance of the optode under these new optical settings, a response curve was generated using the calibration protocol outlined in *1.2.3: Optode Membrane Preparation*. Emission was measured at 680 nm while exciting at 570 nm. An excitation cutoff filter at 660 nm was used to reduce interference. The kinetic scan feature was employed to obtain five minutes of intensity data for each concentration. The results are shown in Figure 24.

^{III} Stokes Shift refers to the difference in wavelength between the excitation source and measured emission (EMwave-EXwave). Industry standards recommend a stokes shift greater than 80 nm to avoid excitation interference.

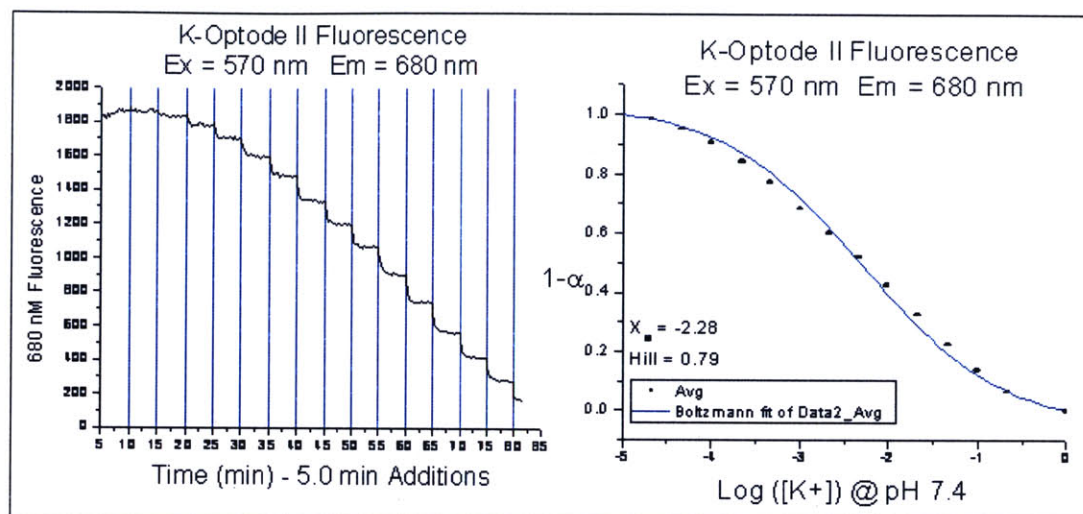


Figure 24: K-Optode II Kinetic Fluorescent Response (ex=570nM)

Measured 670 nm emission intensities increased 4-5 times over the previous 485 excitation data. This drastically improved the signal to noise ratio for the optode membrane. The response curve in the right panel of Figure 24 shows excellent sigmoidal response behavior with highly log-linear response around the inflection point. In addition, the error between the six optodes tested was extremely low. Standard errors were on the order of 0.15% with respect to overall fluorescent intensity. The least squares sigmoidal fit from the response data indicates a X_0 of -2.28, which translates to 5.2 mM potassium at pH 7.4. This directly coincides with standard extracellular potassium concentrations. The Hill constant for the curve is 0.8, which is sub-optimal, but can be improved by increasing additive and ionophore concentrations as described in Section 1.1.1. Overall, K-Optode II displays ideal response behavior for use in the extracellular environment. This optode will be the primary sensor used for the assays developed in the remainder of this report.

1.4.3: Na-Optode I Response Properties

Na-Optode I and K-Optode II matrices are identical except for their ionophores. As a result, all response properties will be consistent except for the selectivity coefficient (X_0). The spectral characteristics for Chromoionophore III have been fully classified in Section 1.5.2; therefore additional spectral analysis for Na-Optode I will be redundant. A single wavelength calibration curve is still required to determine selectivity and classify the response of the optode. Theoretically, the shape of the sigmoidal response curve will be identical to K-Optode II; however, small errors in component concentrations may cause slight deviations. Using the calibration protocols outlined in 1.2.4: *Calibration Protocol*, a response curve for Na-Optode I was generated. Optical response data with a least squares sigmoidal fit is displayed in Figure 25 along with the raw kinetic scan time series data.

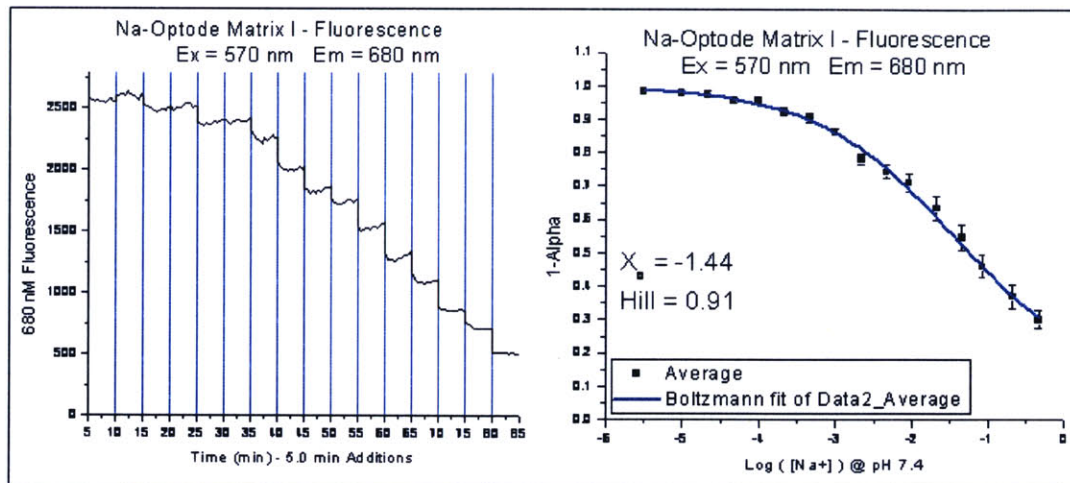


Figure 25: Na-Optode I Kinetic Fluorescent Response (ex=570nm)

The least squares Boltzmann fit calculates the X_0 point for Na-Optode I at -1.44 or 36.3 mM sodium at a pH of 7.4. While not ideal for extracellular sodium measurements (130 mM), the response curve is still log-linear between 1.0 and 500 mM sodium. This will cause the optode to have similar sensitivities in both extra and intracellular environments (130 mM and 10 mM). The hill constant for the response curve is 0.91, which is higher than expected (shallow curve, small slope). As stated in the previous section, this parameter can be improved by increasing additive and ionophore concentrations in the optode matrix.

1.4.4: Sensitivity, Resolution and Dynamic Range

K-Optode I is omitted from the remainder of experiments conducted in this report; therefore optode properties such as sensitivity and response time will only be reported for K-Optode II and Na-Optode I.

Response curves for both optode matrices must be linearized around an equilibrium concentration to permit a sensitivity analysis. Electrolyte concentrations in Buffer # 3 (Chapter 4) are used as equilibrium values since it is the primary extracellular buffer used for the assays in this report (2.7 mM K^+ , 137 mM Na^+). Response curve slopes were calculated about these ion concentrations. In addition, the upper detection limit (UDL) and lower detection limit (LDL) were calculated at the $\frac{1}{2}$ max slope concentrations.

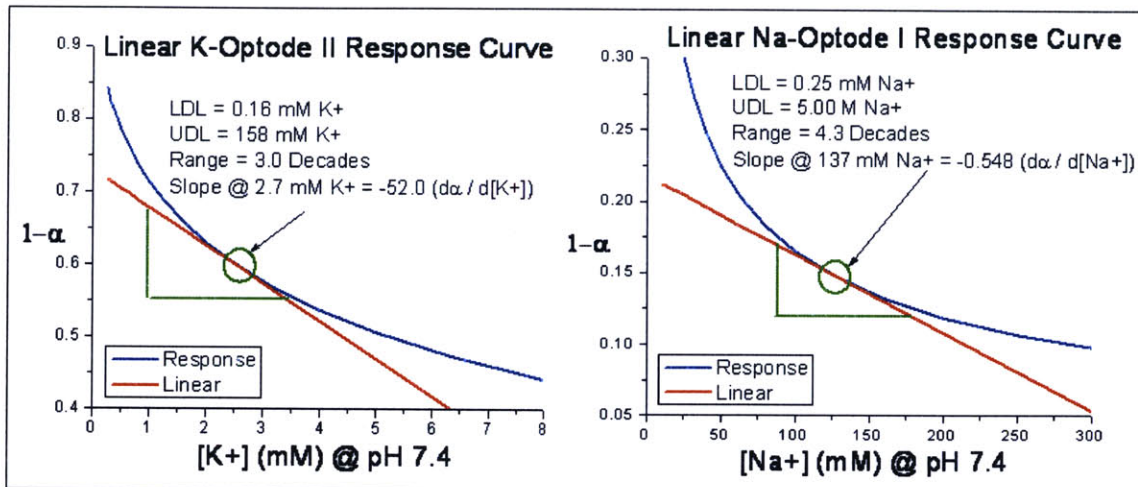


Figure 26: Potassium and Sodium Optode Sensitivities at Biological Concentrations

Figure 26 contains sensitivity and dynamic range information for K-Optode II and Na-Optode I. The slope of the K-Optode II response curve is approximately two orders of magnitude greater than Na-Optode II. This is a result of lower equilibrium concentrations and a smaller Hill constant in the log-response curve. K-Optode II will therefore be one hundred times more sensitive to ion concentration changes than Na-Optode I. In addition, potassium concentration fluctuations are expected to be larger in the extracellular environment during cellular ion signaling. This indicates K-Optode II will be a more robust assays sensor that is capable of detecting small changes in potassium levels. The dynamic range for both optodes is very large (> 3 decades). Since neither ion concentrations will approach the detection limits of the optode under biological conditions, the parameter is not of great concern.

As Equation 15 dictates, the resolution of each sensor is dependant on the signal to noise ratio, which is unique for every individual membrane an optical setup. This makes accurate resolution calculations very difficult for K-Optode II and Na-Optode I. Resolution estimations can be generated using average signal to noise values observed during typical calibration experiments. With a 63% optical response time of around 5 minutes, both optode matrices have average 670 nm fluorescent intensities of approximately 4000 RFUs' using the Gemini EM plate reader. The standard deviation of background noise at this level has been estimated to be between 5 and 10 RFU's. The resulting optode resolutions, with an F_s of 1, are shown in Table 9.

Parameter	K-Optode II	Na-Optode I
Noise / Signal	0.0025	0.0025
Equilibrium Concentration	2.7 mM K ⁺	137 mM Na ⁺
Sensitivity (dα/dI ⁺)	52	0.548
Resolution (μM)	48.1	4562.0

Table 9: Potassium and Sodium Optode Sensitivity and Resolution

As predicted, the resolution of the potassium optode is approximately 100 times smaller than the sodium optode. The “Noise/Signal” parameter (Inverse of S/N) in the above table is unique to the sample optodes on the Gemini EM plate reader. Optical setups on the Zeiss inverted fluorescent microscope described in Chapter 4 have improved noise levels over the Gemini EM. Optodes used with this configuration have reported resolutions as low as 10 μM.

1.4.5: Reversibility

Reversibility of the optode matrices was evaluated by cycling multiple optode membranes with various salt solutions at 10 minute intervals. Figure 27 shows the endpoint 670 nm fluorescence of two K-Optode II coated disks. Solutions were cycled between 0.0 mM K⁺ and 100 mM K⁺ in 10 mM Tris buffer (pH 7.4).

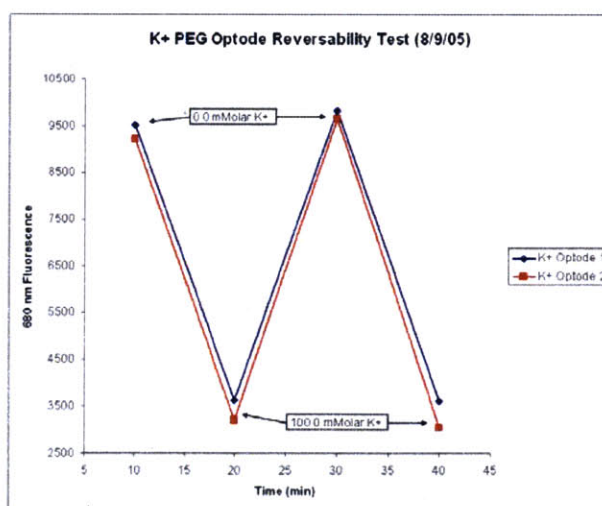


Figure 27: K-Optode II Reversibility

The cycle endpoints show excellent reversibility characteristics. After a single cycle, both optodes fluorescent intensity returned to within four percent of their previous

value. Na-Optode I cycle tests showed similar reversibility characteristics (data not shown). This data shows that the optode matrices used in this report are completely reversible with not adverse effects from binding kinetics. This property is critical for the experiments in Chapter 4, which require the measurement of potassium oscillations.

1.4.6: Response Time

Section 1.4.5 indicates that ionophore binding kinetics have a negligible effect on the response of either K-Optode II or Na-Optode I. For this reason, the response time characteristics for both optode matrices should be identical. For conciseness, only K-Optode II optode membranes are studied in the remainder of this section. Na-Optode I behavior was observed to be identical.

The dynamic properties of K-Optode II membranes were analyzed using four 5mm glass cover slips coated with optode using the droplet technique. The cover slips were placed at the base of their respective wells in a clear bottom 96 well plate. Membranes were purposely made thick (>20 μM) to achieve extended response times. This was done to ensure the majority of the response curve was captured by the Gemini EM plate reader. The resulting response curves for a step increase in potassium are shown below in Figure 28.

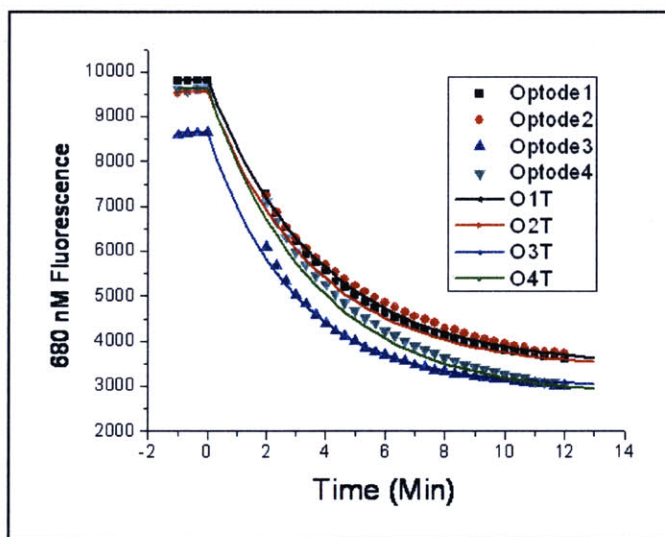


Figure 28: K-Optode II Response Time

The data for all four optodes displays classic first order response behavior. As described in Section I.2.6, the optode response time should be proportional to the square of the membrane thickness. This should also be proportional to fluorescent intensity assuming the membrane thickness is relatively uniform. Using these observations, a first order step-response model was developed for K-Optode II membranes under these optical settings. Equation 18 shows the resulting solution to the first order differential equation.

$$F(t) = (F_o - F_\infty)e^{-\frac{t}{\tau}} + F_\infty$$

$$\tau = (3.9 * 10^{-8})F_o^2$$

F_o = De-Protonated 680 nM Fluorescence

F_∞ = Final 680 nM Fluorescence

Equation 18: First Order Optode Response Model

The constant 3.9e-8 was determined empirically and will be unique for every optical setup. The thickness of the optode membranes was assumed to be proportional to their fully protonated fluorescence (0.0 mM K+), which is shown by the negative time data points. For each optode, their theoretical response is shown by the solid lines of the same color. The correlation between experimental and theoretical data is striking. There is very little deviation between theoretical and experimental data. The slight deviations that do exist on optodes 2 and 4 are most likely the cause of non-uniform membranes. These results prove that optode dynamics can be estimated using a first order model with response time proportional to fluorescent intensity. This model will be used in Chapter 4 to estimate the effect of slow optode dynamics on potassium oscillation tracking.

Chapter 2: Suspended Cell Assays

This chapter chronicles the development of an optode based assay specifically designed for suspended cells. Many modern assays (intracellular calcium) are only able to operate effectively using adherent cell lines; however, there are a large number of biologically relevant cell types that only grow in a suspended format. The beginning of the chapter describes the necessary design characteristics needed to achieve a successful assay specifically designed for suspended cells.

The remaining sections describe the development of a novel optode based suspension cell assay capable of detecting extracellular ion flux. The assay is evaluated using standard fluorescent well-plate reading equipment. To simplify proof-of-concept testing, yeast cells were chosen as the model cell line. Their robust nature allowed the assay to be refined with greater ease. Experimental results for this chapter include drug induced ion flux experiments with two drug compounds known to affect the sterol composition in yeast cells. The results show definitive proof that this assay is capable of detecting extracellular ion flux from suspended cells and could be easily modified for use in conventional high throughput screening infrastructures.

2.1 – Assay Properties

2.1.1: Applications - The Advantage of Suspended Cell Lines

Many cell lines, including many mammalian varieties, grow and proliferate while suspended in a liquid medium. Subsequently, these cells are referred to as suspended cell lines. For many standard intracellular fluorescent indicator assays, suspended cells pose serious problems. The most severe of these is cell movement within the well. During time-series acquisitions, cell movement causes motion artifacts that hamper the assays reliability and reproducibility. Another problem with suspended cell lines is the additional complexity involved with the loading and washing of dyes, which could affect cell viability. For these and other reasons, suspended cells lines are avoided in many high throughput signaling assays.

Despite their incompatibility with indicator dye assays, suspended cells offer a variety of advantages over adherent cell lines. Suspension cells do not require adhesion time before testing. Cell solutions can be dispensed into well plates and evaluated immediately. This results in highly uniform cell populations between wells since little to no growth occurs throughout the testing period. The cell densities are also highly controllable through dilution of an initial sample at high density.

2.1.2: Assay Design Criteria

Developing an optode based assay for suspension cells in 96-well and 384-well plates has a series of critical design requirements that must be met to achieve reliable assay performance. The following criteria represent the most important considerations to the project at its inception.

To maximize optode signal change, it is essential to maintain a high cell to fluid volume ratio. This is easily controlled by spinning cells down to a pellet and

subsequently re-suspending them in the appropriate volume of testing media. To achieve maximum cell signal, extremely high cell densities will be required. However, at very high densities ($> 10^7$), cells will begin to lose functionality and die off. Only empirical testing will yield the optimal cell density that will produce large signal changes while retaining cell viability throughout the duration of the assay. It should be noted that cell settling occurs when using high cell densities unless a mixing protocol is used during the course of the assay. To maintain artifact free fluorescent signals, no mixing procedures were used in the experiments conducted in this report, which means the cells will settle over time. It is difficult to estimate the effects of settling on cell viability and ion signaling ability.

An issue of critical importance in this assay is removing cell matter and debris from the light path of the plate reader optics. High cell densities and movement in the path of either excitation or emission photons could generate noise, scatter, and false signaling. This is a serious problem with current fluorescent based suspension cell assays. The only solution to this problem is to place the optode membrane between the cell solution and the scanning optics. For many commercial plate readers, optimal signal to noise ratios are achieved when the fluorescent material is positioned at the base of each well. These observations imply using a system that positions the optode membrane at the base of the well.

A final design constraint includes the physical integration of this system with commercially available plate readers. This places size restrictions on any features that extend outside of the well plate. Clearances on many plate readers only allow up to ¼" of clearance over the surface of the plate. In addition, all polymer or metal components must be optically and chemically inert. The use of auto-fluorescent or reflective materials will certainly result in compromised system performance.

2.1.3: Assay Design - Optode Disks

For initial proof-of-concept testing, a preliminary optode placement system was developed. The optode calibration protocols described in Section 1.3.3 require an optode membrane to be spin coated onto a 5mm glass disk and placed in the bottom of an optically clear 96-well plate. Fortunately, this optode insertion technique satisfies all of design requirements outlined in the previous section. The system has certain limitations, but proved effective for initial testing. A picture of this optode disk placement system is shown in Figure 29.



Figure 29: Nunc 96-well Plate Containing Optode Coated 5mm Glass Cover Slips

For the experiments conducted in this report, the optode disks were placed in each well manually. Future use of this assay system would promote the development of a semi-automated system to deposit each disk in parallel. Ideally, the use of glass bottomed plates would permit the application of dissolved optode directly to the base of each well. This would eliminate the need for optode disks all together. Glass bottom plates were not used in this study because of their high cost.

2.1.3: Limitations

A critical drawback to this assay is the time and labor intensive setup protocol. The process of spin coating a membrane onto a small disk, and then manually placing the optode into a well is highly tedious. Often, the membrane was damaged or the disk was inverted, which lead to prolonged response time and lower signal to noise ratios. On average an entire 96 well plate would take in excess of two hours to prepare with a single person. The high level of human involvement and skill imparts unreliability and irreproducibility into the system.

Additional problems with this system are created by the gap between the bottom of the well and the glass disk. Once fluid is wicked into this area, the optode disk was extremely prone to sliding with any sort of plate movement. Any movement of the disk would result in changes in optical intensity. Ratiometric analysis can subtract this phenomenon to a certain degree, but it is still undesirable. In addition, bubble formation was frequently observed in this gap region when testing at 37°C. These bubbles would increase optode shift while also changing the height of the membrane from the bottom of the well. This phenomenon also made it extremely difficult to replace the fluid in the wells. Upon fluid refill, the optode disks would float, which required manual re-submersion. This was observed to damage the membrane or invert the disk.

Virtually all of these limitations could be corrected by employing the assay insert module developed in Chapter 3 for adherent cell lines. This system would have been

used for the following experiments, but the technology was not fully developed at the time. These limitations could also be corrected by using micro-sphere deposition to form an optode layer directly on the base of each well.

2.2 – Target Cell Line: Saccharomyces Cerevisiae

2.2.1: Cell Properties

Saccharomyces Cerevisiae is a robust species of budding yeast. It is probably the most popular of the yeast family for its use in baking and brewing. Despite being a single cell form of fungus, Saccharomyces Cerevisiae is a eukaryotic cell line, which means it has a similar complex internal structure to plants and animals. It also proliferates in suspension format at very high growth rates. Most importantly, Saccharomyces Cerevisiae contains an advanced system of ion channels and receptors, which will allow ion signaling [53, 54].

In particular, the Saccharomyces Cerevisiae gene ERG2 encodes a sterol C8-C7 isomerase, which is used for cell proliferation and ergosterol synthesis [55]. It has been reported that this isomerase carries a similar binding affinity to sigma receptors in mammalian cell lines. The same source has shown that specific sigma ligands (Haloperidol and Ifenprodil) directly altered sterol composition in yeast cells. In their study, the changes in sterol composition halted cell proliferation. In addition to proliferation, ergosterol is a critical component in the cell membrane [56]. A change in ergosterol composition could alter membrane functionality, which would therefore induce ion signaling.

Assay validation was performed using two yeast cell lines. The first was a standard wild type strain of Saccharomyces Cerevisiae with no genetic modifications. The second yeast strain was Saccharomyces Cerevisiae with the ERG2 gene removed. It is anticipated that sigma ligands will have a reduced effect with the ERG2 knockout strain [55].

2.2.2: Test Compounds - Haloperidol and Ifenprodil

Haloperidol and Ifenprodil were used as test compounds to evaluate the effectiveness of this assay. Both compounds have been shown to affect the sterol C8-C7 isomerase, which should alter cell membrane properties. Haloperidol has a slightly higher binding affinity than Ifenprodil. The K_d for Haloperidol and Ifenprodil were reported at 0.3nM and 1.4 nM respectively [56]. These compounds should elicit some form of dose dependant ion signaling from yeast cells.

2.3 – Experimental Methods

2.3.1: Reagents

Yeast colonies were grown using Yeast Malt Agar on 6 cm Petri dishes. The resulting colonies were proliferated in a suspension medium of YPD Broth. Both growth mixtures were acquired from Sigma-Aldrich at the highest available quality. For ion flux experimentation yeast cells were re-suspended in a 10 mM Tris buffer containing 150 mM NaCl and 5 mM KCl. Trizma-Base, NaCl, and KCl salts were acquired from Sigma and Tris-HCl was acquired from ICN Biomedical. This solution will be referred to as Buffer # 1 for the remainder of the chapter.

2.3.3: Yeast Culture

At the beginning of each month, two 6.0 cm dishes were plated with YPD agar at a thickness of approximately 2.0 mm. Once fully cured, the surface of the agar was seeded with swabs of frozen yeast stock. One plate was seeded with standard wild type yeast and the remaining plate with an ERG2 knockout line. After 48 hrs in a 37° C incubator, the plates were removed and stored in a 4° C refrigerator shielded from light. On average, a single plate would yield between 100 and 1000 individual yeast colonies. These plates would be used throughout the remainder of the month to provide initial colonies for individual batch preparation.

The day prior to assay testing, a single yeast colony was be removed from the appropriate 6cm dish and placed into a 125 mL erlenmeyer flask containing 20 mL of YPD broth. After 24 hours in a 37° C incubator, each 125 mL flask would yield enough cells for approximately 50 wells (5000 µL total cell solution). Cells were then prepared for assay testing with the following protocol.

2.3.4: Assay Protocol

Prior to yeast introduction, a 96-well plate was prepared with optode membranes. 5mm No.1 glass cover slips were spun coat with K-Optode II at approximately 3,000 RPM. The dissolved optode solution consisted of a THF/PVC ratio of 5:1 (mL/100mg). This produced optodes with acceptable signal to noise characteristics while still retaining response times under five minutes. A single optode disk was carefully placed at the bottom of each well using a specially modified pair of tweezers. Utmost care was required not to damage the membranes upon insertion into the well.

After 24 hrs in a 37°C incubator, the 20 mL yeast/YPD broth mixture was aspirated and transferred into two 15 mL centrifuge tubes. The tubes were spun at 200 g's for 10-15 minutes. Once a yeast pellet was sufficiently formed at the base of each tube, the excess YPD broth was aspirated and disposed of. Each tube was rinsed twice with Buffer # 1 to remove any excess broth and loose cell debris. After rinsing, 5 mL of

Buffer # 1 was then added to each tube and the cells were re-suspended through vortexing or fine tip pipette trituration. The contents of each tube were then transferred to separate 30 mL capacity polycarbonate troughs. An eight channel multi-cell pipette was used to distribute 100 μ L of the cell/buffer mixture into each well. Constant mixing of the cell solution was required to maintain a uniform cell density throughout the filling process.

Once fully prepared, the plate was placed in a Gemini EM plate reader (Molecular Devices) at 37°C for 30 minutes prior to drug addition. This base line test assured the entire plate would reach thermal equilibrium. Also during this time, the wells were scanned using Kinetic mode to observe any abnormal optode behavior. Depending on the number of wells, up to three wavelengths would be used to scan each well (ex=485, em=570: ex=485, em=670: ex=570, em=670). Large variances in any of these time series traces were strong indicators of a suspect optodes. This was usually caused by membrane damage, bubble formation, or disk inversion. Suspect optodes were consequently omitted from assay analysis.

After a 30 min baseline, the plate was ejected and drug was added using an eight-channel multi-well pipette. To achieve a 10% dilution, 11 μ L of drug solution was added to each well. Drug compounds were dissolved in Buffer # 1 to eliminate any adverse effects from buffer changes. The plate was re-inserted into the Gemini EM plate reader and scanned using baseline setup parameters, but for a total of 50-80 minutes. Assay data was extracted as a .txt file using Softmax 4.8 and process using the protocol outlined in the following section.

2.3.4: Data Processing

For each test set, a minimum of three wells were used (N=3). The .txt files from Softmax 4.8 contained the fluorescent time series data from each optode. The .txt files were exported to Excel using a custom Matlab GUI subroutine. In Excel the time series data sets were normalized and averaged to yield a single time series trace for each three test set optodes.

To normalize these traces, the time series data for each optode was divided by the average of the first two points in the series. This accounted for any fluorescent intensity variation between optodes. After this, the three time series data sets for each optode were averaged together to produce a single trace. The resulting series represented the average time-series behavior for that test set of optodes, which was integrated to yield a single value representing ion flux magnitude.

With each test set, it was necessary to subtract the normalized control data. This was accomplished by fitting 3rd order polynomials to each control data set. These polynomials were then subtracted from the compound stimulated data sets for each cell type.

2.4 – Results and Discussion

2.4.1: Dose Response

The first assay validation experiment consisted of four individual ligand binding test sets. A single optode (Na-Optode I) was used to measure the sodium ion flux from wild type *Saccharomyces Cerevisiae* and an ERG2 knockout strain in the presence of Ifenprodil and Haloperidol (separately). A control set was included for each cell type to measure the natural ion flux with no drug present. These control well traces were later subtracted from active wells to obtain raw drug induced ion flux. Figure 30 shows the resulting average time series traces for each test set.

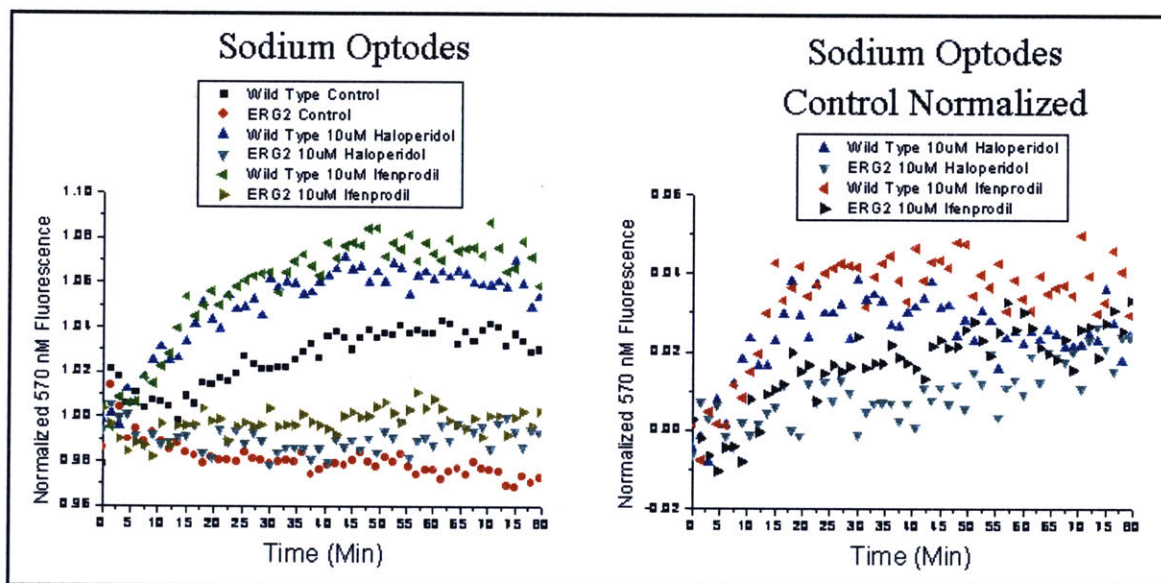


Figure 30: Compound Induced Extracellular Sodium Flux from Yeast

The left panel of Figure 30 shows the time series traces for all six test sets (4 compounds and 2 controls). The Y-axis represents normalized 570 nm Fluorescence, which represents percentage change in fluorescent intensity (around 1.0). An increase in 570nm fluorescence represents an increase in sodium concentration. It is interesting to note the control wells for wild type (WT) and the ERG2 knockout strain (E2K) drift in opposite directions. The WT control (black-square) shows an increase in sodium concentration, while the E2K (red-diamond) shows a decrease. In fact, all the WT traces show an upward trend, while the E2K traces show a neutral or decreasing trend. This was most likely the result of long term cell equilibration with the new extracellular matrix (Buffer # 1), which is at a slightly different ion concentration and pH than the growth medium. The resulting control-normalized time series traces are shown in the right panel of Figure 30.

All four data sets showed a strong increase in extracellular sodium concentration over time. This is counter to theory that these compounds might cause the cell membranes to become ion-permeable, which would cause sodium to enter the cell. It is possible that the cells absorbed sodium when they were initially exposed to the new extracellular matrix (Buffer # 1). These compounds could then have triggered a re-release of this stored sodium. It is also feasible that these compounds produced a change in membrane potential. This could trigger a series of ion channel and pump activity.

To quantify the magnitude of the compound induced sodium flux, the average change in fluorescent intensity was calculated 30 minutes after compound exposure. The resulting bar graph plotting the relative change in fluorescence is shown below in Figure 31.

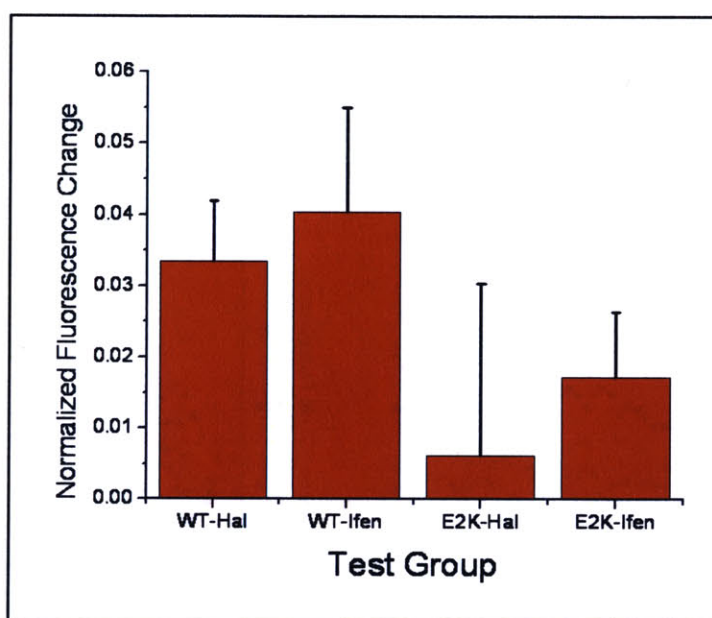


Figure 31: Statistical Results from Sodium Flux Time-Series Data

The bar plots in Figure 31 contain positive error bars which designate a single standard deviation (since $n=3$ standard error is very similar). This figure presents a noticeable increase in cellular activity in WT cells over the E2K cell with both compounds. This is expected since Ifenprodil and Haloperidol target the ERG2 encoded isomerase. The E2K cells do elicit some cellular activity, which is most likely the result of additional non-specific receptor and enzyme binding. Both compounds have strong affinities for a host of naturally occurring receptor sites in mammalian cells. The difference in activity between the two compounds is not significant with this experimental data, which was to be expected. Both cell types show similar response with respect to the standard deviation. The error bars are relatively large since the sample group was small ($n=3$). Larger test groups in future experiments would help to reduce the magnitude of these errors.

An identical experiment was conducted using a potassium optodes with similar results. The 570nm fluorescence indicated a reduction in extracellular potassium, which is also counter to the ion-permeable membrane theory. This result is promising because it rules out the possibility that the yeast cells are changing the pH of the extracellular solution. Any alterations in pH would cause both sodium and potassium optodes to respond in the same direction.

To further expand the experimental evidence promoting the effectiveness of this assay, a secondary set of experiments were conducted to obtain a dose-dependant potassium flux relationship. For maximal signal generation, only *Saccharomyces Cerevisiae* was chemically stimulated (No ERG2 Knockout).

The experiment consisted of two sub-sets that used potassium optodes (N=3) to measure the long term ion flux from yeast cells in the presence of three different Haloperidol concentrations (10, 100, 1000 nM). A control set was also used in each sub-set to measure natural ion flux from un-stimulated cells. The first sub-set was prepared in a manner consistent with Section 2.4.2 (30 min pre-incubation). The second subset exposed all test wells (including the control) to 1.0 μ M Ifenprodil fifteen minutes period to Haloperidol additions. The time-series averages for each sub-set are displayed in the two panels of Figure 32.

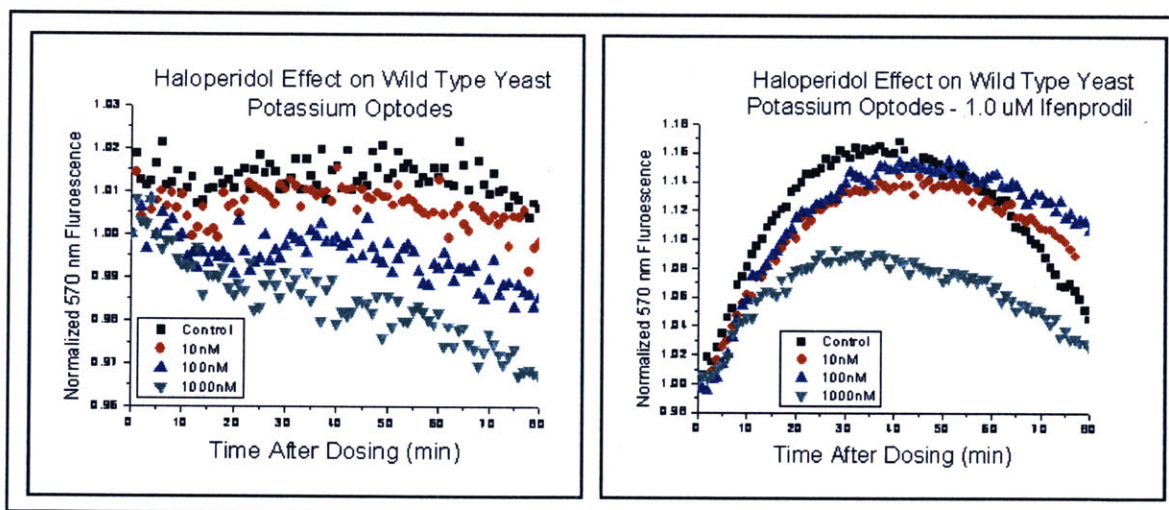


Figure 32: Compound Induced Extracellular Potassium Flux from Yeast

The left panel of Figure 32 shows the natural response of *Saccharomyces Cerevisiae* after exposure to various concentrations of Haloperidol. The Y-axis of each panel indicates normalized 570 nm fluorescence. As with Section 2.4.2, an increase in normalized 570 nm fluorescence represents an increase in potassium concentration. The time series trace for the control wells (black-squares) is very level, which is evidence that the cell is in a natural resting state. With each increase in Haloperidol concentration, the traces exhibit an increasing downward slope. All traces are relatively linear over time.

This translates to a long term steady state decrease in extracellular potassium directly dependant on Haloperidol concentration.

The right panel of Figure 32 shows the potassium dose responses after pre-incubation with Ifenprodil. All traces, including control wells, show a dramatic initial increase in potassium concentration, followed by a slow return to initial values. This “hump” behavior is clearly visible in the control well time series trace average (black-square). As with the left panel, this Haloperidol exposed wells show lower extracellular potassium concentration with respect to the control wells.

To investigate the extent of Haloperidol concentration on ion flux magnitude, a four point EC50 curve was generated for each subset. Activity was measured as the average fluorescent intensity change fifty minutes after Haloperidol addition (control normalized). The resulting dose-response curves are pictured in the right panel of Figure 33.

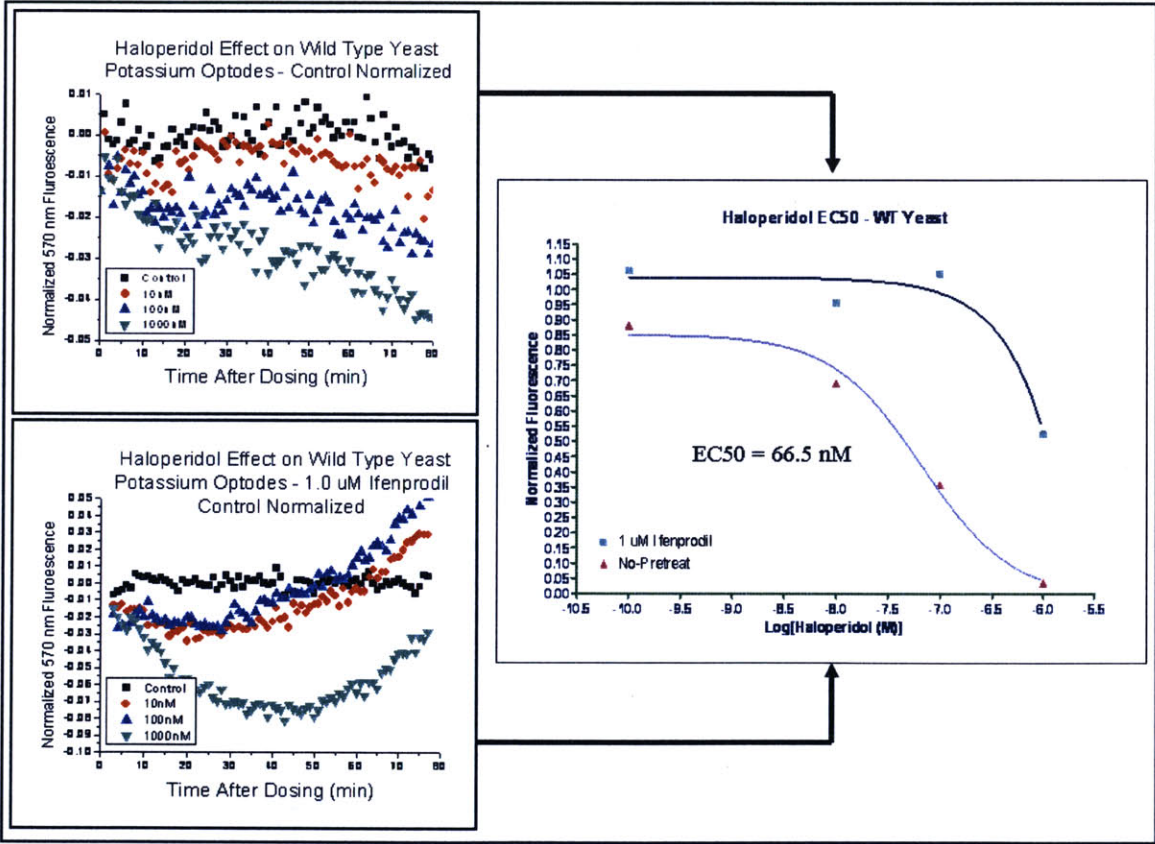


Figure 33: Haloperidol Dose Response from Yeast using Extracellular Potassium Concentration

The triangle data series in the right panel of Figure 33 represents the dose response data for pure Haloperidol induced potassium flux (no Ifenprodil). The curve

shows classic sigmoidal response behavior with a reported EC50 value of 66.5 nM. The K_d for Haloperidol was reported at 0.3 nM for the C8-C7 isomerase, which is far lower than the observed response behavior [56]. The elevated EC50 value could be due to a host of factors including exposure time, temperature, ion concentrations, etc.

The second dose response curve in Figure 3 (triangle) was derived from the test sub-set exposed to 1.0 μ M Ifenprodil fifteen minutes prior to Haloperidol addition. This curve shows an increase in Haloperidol EC50 by almost two decades. This increase is most likely the result of Ifenprodil occupying a vast majority of active binding sites. This would require an increased Haloperidol concentration to elicit a similar cellular response.

2.4.3: Assay Conclusions

The assay presented in this chapter proved capable of detecting extracellular potassium and sodium ion flux from yeast cells. Signal to noise levels were significant enough to produce dose-dependant relationships and identify gene knockout strains. Potassium and sodium flux was observed to act in opposing directions, thus ruling out the possibility of pH interference.

Despite its effectiveness, this assay could be improved through several modifications. Reliability could be increased by coating optode membranes through micro-sphere deposition. This would reduce variability between wells and increase signal to noise. Any motion artifacts from cover slip movement would also be avoided. The optode matrices could also be modified to improve response magnitude. By tuning the component ratios the slope of the response curve could be increased around the equilibrium concentration.

Chapter 3: Adherent Cell Assay

The following sections review the development of an optode based high throughput whole cell assay specifically designed for adherent cell lines. Adherent mammalian cells dominate the majority of existing whole cell assays used by pharmaceutical companies and research laboratories.

Section 3.1 reviews the various applications for adherent cell assays and their importance to modern drug discovery. Section 3.2 details the design of a novel optode sensor module specifically engineered for adherent cell lines in standard 96-well and 384-well plates. The system does not affect cell viability and is compatible with virtually all commercially available plate readers. The remaining sections review the results from a sample assay using potassium optodes to measure extracellular ion flux from HEK 293 (Human Embryonic Kidney) cells. Results include EC50 curve generation and Z-factor calculation for the assay.

3.1 – Assay Properties

3.1.1: Applications - Biological Relevance of Adherent Cell Lines

An adherent cell line requires adhesion to a fixed surface to permit cell growth and proliferation. Adherent cells are commonly grown on polystyrene substrates in a shallow bath of growth medium. The height of fluid over the cell monolayer is usually between 5 and 8 millimeters to allow proper gas exchange. The polystyrene substrate can be treated with a variety of compounds, such as poly-D lysine, to promote cell adhesion. Cells will continue to multiply on the substrate until the entire surface is covered with a monolayer of cells. This is referred to as 100% cell confluence.

Virtually every adherent cell line is derived from a type of tissue. Cells from the heart, kidney, nerve, and smooth muscle, are all classified as adherent cell lines. Since these tissues are crucial for therapeutic target evaluation, these cells encompass the majority of whole cell based assays used in drug discovery. An additional benefit to adherent cell lines is their obvious ability to remain stationary in a multi-well plate throughout the time course of the assay. For assays that incorporate intracellular dyes, this is a crucial factor. The development of an optode based assay for adherent cells would be highly advantageous in the field of drug discovery.

3.1.2: Assay Design Criteria

Using optodes with adherent cells in standard 96 and 384 well plates introduces a host of additional design problems not encountered with the suspended cell assay system presented in Chapter 2. The most severe of these problems is achieving adequately high cell to fluid volume ratios. Excess extracellular fluid will dilute the cellular ion flux below the detection limit of the optodes. Theoretically, maximizing ion flux signal would require using an ultra-thin layer of fluid to encapsulate the cell monolayer (only a couple cell diameters in thickness). This would reduce the fluid volume while maintaining cell viability. In practical conditions with multi-well plates, surface tension

makes this extremely difficult to achieve. In addition, the optode membrane must be in contact with the fluid layer and remain visible to typical plate reader optics.

Obtaining high cell to fluid ratios could be achieved by using a single high precision isolated cell chamber. This technique is employed in Chapter 4 to measure action potential ion flux from ventricular cardiac myocytes. Creating high cell to fluid volume ratios in standard 96-well or 384-well plates becomes much harder due to surface tension and evaporation. The shape of a 96-well, combined with the surface tension of the water/plastic interface creates a highly curved meniscus. The curvature of the fluid surface is dependent on the shape of the well, surface treatment, and various additional fluid and material properties. Since many of these parameters are variable between experiments, it is difficult to reliably model and predict surface curvature. To avoid surface tension problems, well-plate manufacturers' often recommend working volumes in excess of 50 μL for 96-well plates. Below this the meniscus will create a dry spot in the center of the well causing cell death. For this application, it has been estimated that the well volume must not exceed 20-30 μL to maintain acceptable ion signal generation. This estimation was based off the optode sensitivity analysis performed in Chapter 1. Evaporation is a problem in any whole cell assay, but reducing well volume will further exacerbate this phenomenon. These problems are equally prevalent in 384-well plates.

It is critical that the system must be able to position an optode membrane where it is sufficiently visible by standard plate reader optics. The membrane must also remain in contact with the extracellular fluid layer at all times. Virtually every high throughput fluorescent plate reader, including the FLIPR by Molecular Devices, scans each well from underneath the plate. Often, the excitation light enters the base of the well at a 20-45 degree angle to the bottom of the plate. The resulting emission light is then gathered using a PMT or CCD camera positioned directly below the well (sometimes offset at an opposing angle). Manufacturers have optimized their scanning optics to achieve optimal sensitivity when used with fluorescent dyes loaded into cell monolayers adherent to the base of each well. The following diagram shows an optical layout typical to common plate readers that use bottom-scanning optics.

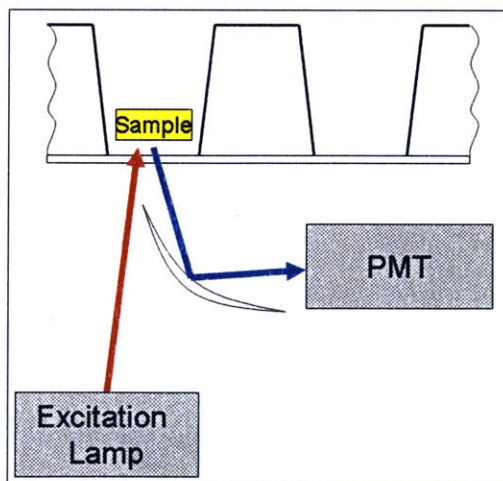


Figure 34: Typical Bottom Scanning Fluorescent Plate Reader Optics

For this system to attain optimal performance, the excitation photons must intersect a large percentage of the optode surface. In addition, scatter must be kept to a minimum to maintain acceptable signal to noise ratios.

Above all, the sensor system must be physically compatible with common plate readers. This places further restrictions on the external dimensions and shape of any sensor placement devices. Virtually every high throughput screening system utilizes automated fluid handling. If possible, the sensor system should also permit the use of such robotic systems.

3.1.2: Assay Design: Optode Insert Module (OIM)

Many of the design problems discussed in the preceding section were addressed through the development of a novel optode insert module (OIM). The OIM is a single polymer piece that mates with standard optically clear 96-well or 384-well plates. Once press fit into place, each well contains a tapered post that terminates in a flat surface parallel with the base of the well. The surface of each post is coated with a thin optode membrane, which rests approximately 50-300 microns above the bottom of the well. This forms a relatively constant thickness cell chamber, which will concentrate cellular ion flux and maximize optode signal change.

In this configuration, the optode membrane is positioned where it is highly visible to most conventional “bottom read” scanning optics, which maximizes optical throughput. In the annulus between the post and the well perimeter, a small ring of fluid is exposed to the atmosphere. The shape of this region greatly reduces surface curvature, which permits low fluid volumes while still maintaining cell viability. In addition, the smaller surface area helps to reduce evaporation. The most recent 96-well and 384-well prototype insert modules are shown in Figure 35 (SolidWorks).

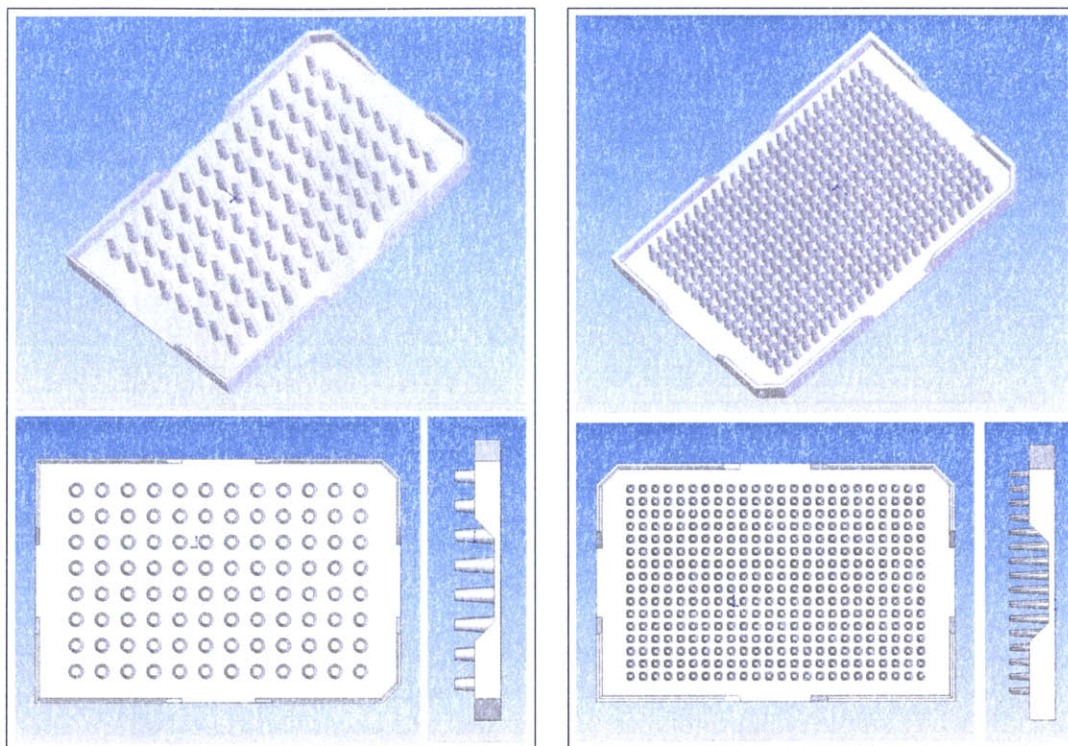


Figure 35: Solid Models of 384 and 96-well OIM (Optode Insert Module) Prototypes

Several other optode configurations were tested prior to the OIM designs above. These systems included extracellular optode spheres, floating disks, ring inserts, and a host of other promising setups. Despite the limited success with some of these additional designs, the OIM system proved to be highly robust and satisfied a large percentage of the design criteria outlined above.

A critical design parameter for the OIM was the diameter of the insert post with respect to the well diameter. If the post was too small, the optode membrane area was reduced, which detracted from the signal to noise ratio. In addition, the photons intersecting the side of the post had the potential to cause artifacts. A secondary disadvantage to small post diameter was the resulting increased surface curvature. This was shown to produce dry spots at low fluid levels. The increase in surface area also accelerated evaporation.

Conversely, as the post diameter increased, fluid was extremely prone to “wicking” up and around the well perimeter as a result of capillary forces. Large post diameters were also shown to increase the occurrence of bubbles underneath the optode membrane. The following diagram displays the occurrence of these problems.

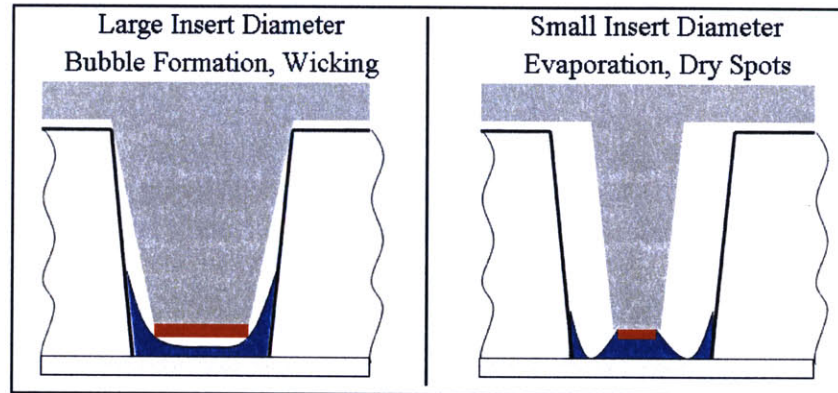


Figure 36: Common Problems with Post Insert System

Empirical testing showed an optimal post to well diameter ratio to be around 1:2. Deviation outside this ratio with either 96-well or 384-well OIMs caused severe problems.

Prototype optode inserts for both 96-well and 384-well plates were modeled in SolidWorks 2005. Design parameters such as post diameter and shape were determined empirically using single well prototypes. All fits and tolerances were checked by reverse modeling both 96-well and 384-well Nunc Plates into SolidWorks. The solid models could then be fit into each other and tolerances assessed. Prior to fabrication, it was essential to identify critical material properties that would affect system performance. Due to the complexity of this application, chemical, optical, and mechanical properties were all relevant to system performance.

Material Constraints

The membrane fabrication techniques discussed in Section 1.3 require the plasticized PVC to be dissolved in an appropriate solvent, typically THF. For the insert posts to retain acceptable dimensional tolerances, the material must be chemically resistant to THF and other similar organic solvents. This would also prevent any chemical interaction between the optode membrane and the insert material. Unfortunately, many common polymers have poor chemical resistivity towards THF. Metal insert posts were explored, but adverse optode response characteristics were observed. The cause of these metal/optode interactions was never resolved. Ceramics are expensive and difficult to machine. This limited the list of acceptable materials to polymers with acceptable resistance to THF, which are listed in Table 10.

Material
304 stainless steel
316 stainless steel
Acetal (Delrin®)
Bronze
Carbon graphite
Carbon Steel
Ceramic Al2O3
ChemRaz (FFKM)
Epoxy
Hastelloy-C®
Kalrez
Kel-F®
Nylon
Polyetherether Ketone (PEEK)
PPS (Ryton®)
PTFE (Teflon®)

Table 10: Materials Chemically Resistant to THF

A secondary material property of concern was autofluorescence^{IV}. Most polymers do not autofluoresce on their own (in pure form). However, certain cross linking and formation procedures can cause this phenomenon. High levels of background fluorescence will inevitably reduce the reliability and signal-noise ratio of the optode. Background fluorescence can be subtracted to a certain degree; however, it is highly undesirable. If the insert shifts or changes fluorescence in any way the optode signal will be affected resulting in interference. Polymer auto-fluorescence was a considerable concern when choosing the appropriate material for this application.

A host of mechanical properties also have the potential to influence system performance. Several dimensional tolerances on the OIM have a direct effect on system performance. The two most critical dimensions are post height and spacing. Changes in either of the parameters will alter fluorescent intensity and may affect cell viability (physical contact). Since the system is typically used at 17° C above room temperature (37 - 20° C = 17° C = 98.6 - 68° F), a large coefficient of thermal expansion could cause noticeable changes in these critical dimensions. Having a large thermal capacitance would be advantageous to reduce temperature fluctuations caused by the temperature control systems in the reading chamber. Since most commercial plate readers have robust temperature control systems this should not be of great concern.

The largest forces applied to the insert module will occur during handling, such as preparation and cleaning. Future optode inserts will most likely be disposable, but high prototype costs dictate re-use from run to run. To maintain assay repeatability, the optode inserts need to retain their physical dimensions over time. This requires using a material that is both hard and strong to prevent scratching and bending, respectively.

^{IV} Autofluorescence refers to the ability to re-emit absorbed light at a higher wavelength

Scratches on the insert post surface would result in non-uniform membrane formation, hampering optode performance. If the post was bent prior to insertion, the optode membrane would not reside in the center of the well. This would cause a host of adverse effects including light scatter and dry spots.

Fabrication

Based on the material and design constraints discussed above, initial prototypes were fabricated using a SLA (stereo-lithography) rapid prototyping machine, which uses a form of epoxy resin. Rapid prototyping was highly advantageous for these parts due their inherent complexity and high tolerance requirements. Machining such parts would have required several hours on a CNC milling machine. This rapid prototyping system has 0.001” tolerance capabilities and is relatively inexpensive. Since only three or four inserts were required for initial testing, this technique was ideal. CNC machining was considered for flexible material selection, but prototype cost would have dramatically increased. In addition, the deep narrow cutouts on the 384-well insert would be virtually impossible to machine effectively. Prior to fabrication, a complete material assessment was performed on the epoxy resin RenShape SL 5220 to ensure proper material performance.

RenShape SL 5220 epoxy resin material properties were gathered and evaluated against the criteria outlined above. Table 11 contains relevant material properties for this material (fully cured).

RenShape SL 5220 Material Properties	
Property	Value
Hardness, Shore D	86
Tensile Modulus	2,703 MPa
Tensile Strength	62.0 MPa
Elongation at Break	8.30%
Glass Transition	53° C
Coefficient of Thermal Expansion	96.0e-6 /°C
Thermal Conductivity	0.156 W/m °K

Table 11: Material Properties for RenShape

Virtually all forms of epoxy are chemically resistant to THF. Bench top testing of a cured resin sample indicated no signs of chemical interaction after two hours of exposure to a 100% THF solution at room temperature. Typically membrane formation only requires the substrate to be exposed to THF for less than 20 minutes. Based on this assessment, chemical compatibility will not present a problem.

The epoxy resin also appeared to be sufficiently hard for this application. A Shore D hardness of 86 is relatively high when compared with other polymers that are chemically resistant to THF. Teflon, nylon, and polyethylene and have Shore D hardness values less than 75. This should help to prevent scratching and extend part lifespan.

To assess the materials autofluorescence characteristics, a small cured sample was placed in a 12-well polycarbonate plate and scanned at various wavelengths. Unfortunately, RenShape SL 5220 exhibited significant auto-fluorescence at low excitation wavelengths. At 485 nm excitation, peak fluorescence was observed at 520 nm and continued into the mid-600 nm range. This will cause a noisy and un-reliable dual-peak analysis with Chromoionophore III. Fortunately, when excited at 570 nm or higher, the epoxy autofluorescence was reduced by almost an order of magnitude. The emission at 670 nm was only slightly above typical background fluorescence. These results limited OIM prototypes to single 670 nm peak analysis only (ex=570 nm).

To model the effect of thermal expansion on dimension tolerances, simple calculations were performed on the two dimensional parameters of critical importance (post spacing and height). Both plate and insert module will expand upon an increase in temperature. The difference in thermal expansion coefficients will determine the dimensional changes between the inert module and well plate. Virtually all multi-well plates are constructed using polystyrene, which has a coefficient of thermal expansion of approximately $68.0 \times 10^{-6} / ^\circ\text{C}$. This is 28×10^{-6} lower than RenShape SL 5220. At 37°C , the thermal expansion difference will be approximately 4.76×10^{-4} ($[37^\circ - 20^\circ] * 28 \times 10^{-6} = 4.76 \times 10^{-4}$). At room temperature (20°C), the post height on the 384-well insert is 11.9 mm. The resulting gap between the end of the post and the bottom of the well is 100 microns. At 37°C the gap will decrease by 5.66 microns ($11,900 * 4.76 \times 10^{-4} = 5.66$ microns). This gap change of 5.66 % should not affect system performance in any noticeable fashion.

Across the longest diagonal of the 384-well OIM, the distance between corner insert posts is 124 millimeters. Assuming the insert posts in the center of the plate do not shift with respect to the well, the outer most posts will expand outward a distance of 29.5 microns ($62,000 * 4.76 \times 10^{-4} = 29.5$ microns). The overall diameter of the well is 2,900 microns, so the post position will only shift 1% of the well diameter. Optical and fluidic effects should be negligible.

To assess the durability of the prototype, a bending analysis was performed on a single 384-well insert post. The goal of the analysis is to estimate the maximum lateral force that would initiate permanent deformation or failure. Despite their slight tapers, the maximum bending moment still acts at the base of these posts. The bending and shear stresses were used to calculate the Von-Mises stress at the outer most point of a post base. Figure 37 shows a schematic of the bending analysis. The resulting analytical results are shown in Equation 19.

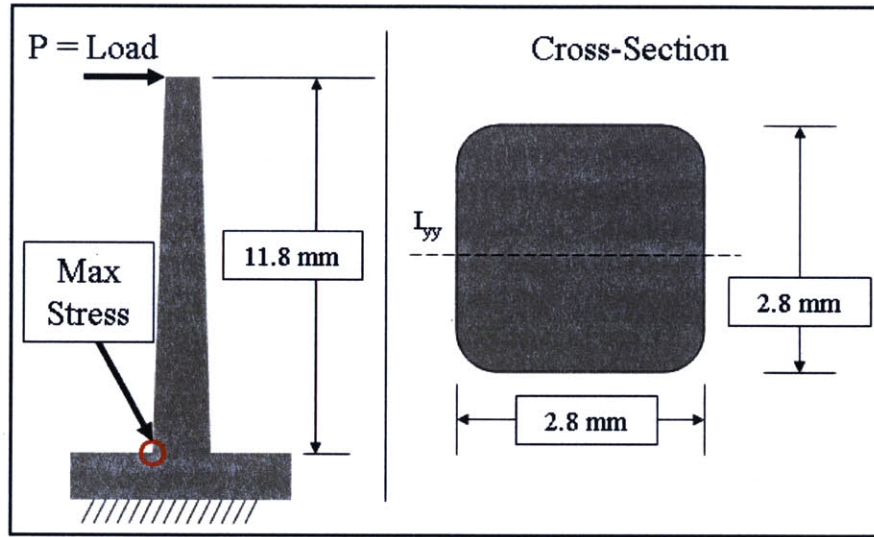


Figure 37: Diagram of Bending Analysis on a Single 384-Well OIM Post

$$I_{yy} = \frac{1}{12}bh^3 = \frac{1}{12}(0.0028)(0.0028)^3 = 5.12e^{-12} \text{ (M}^4\text{)}$$

$$M = P * L = 0.0118P \text{ (N-M)}$$

$$C = .5 * (0.0028) = 0.0014 \text{ (M)}$$

$$\sigma_{xy} = \frac{P}{A} = \frac{P}{(0.0028)^2} = 0.128P \text{ (MPa)}$$

$$\sigma_x = \frac{MC}{I_{yy}} = \frac{P(0.0118)(0.0014)}{5.12e^{-12}} = 3.23P \text{ (MPa)}$$

$$\sigma_1 = 3.24P$$

$$\sigma_2 = -0.005P$$

$$\sigma_3 = 0$$

$$\sigma_{yield} = 62.0 \text{ (MPa)}$$

$$\sigma_{mises} = \sqrt{\sigma_1^2 - \sigma_1\sigma_2 + \sigma_2^2} = 3.24P$$

$$P_{yield} = 19.1 \text{ (N)} = 4.3 \text{ (Lbs)}$$

Equation 19: Bending Analysis Calculations

The analysis predicts yield at a lateral loading of 4.3 lbs. Even with a factor of safety of two, the posts should be able to support a static load of over two pounds. With the exception of strong impacts (dropping), the post load should remain well under two

pounds during normal operating conditions. The RenShape SL 5220 resin should produce a robust insert module that delivers reliable performance.

With initial analysis predicting acceptable part performance, OIMs were fabricated for both 96-well and 384-well plates. Photographs of the initial 384-well insert module are shown in Figure 38 below (edges were machined off to reduce evaporation effects).

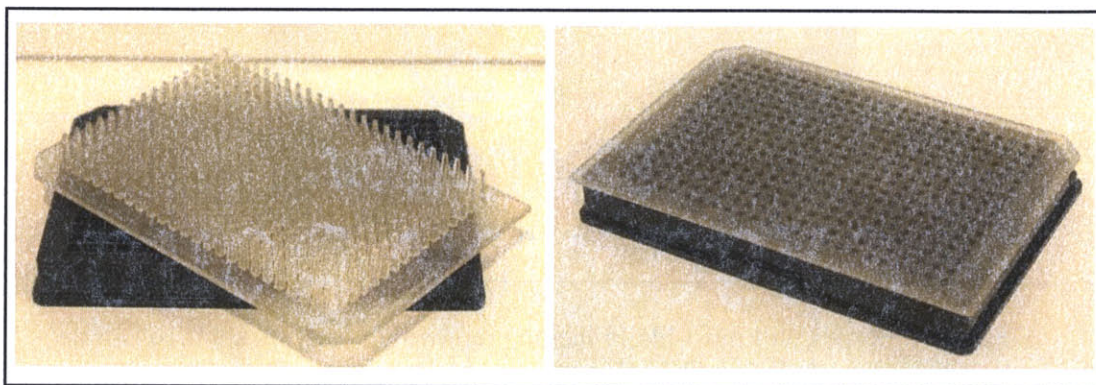


Figure 38: 384-Well OIM (Optode Inset Module) Prototype

Visual inspection of both prototypes indicated excellent part quality. The surface finish on the end of the posts was very smooth and uniform with no apparent defects. No additional smoothing was required to achieve uniform optode fabrication. The only problem noticed between both pieces was the formation of small bubbles within the resin during the layering process. These voids were only found in the support structure of the piece, so there should be no effect on light scatter or post integrity.

3.1.3: Limitations

Despite satisfying many of the design criteria discussed above, the OIM system has some limitations. Since each insert is fixed to a solid backing, it is impossible to fabricate optode membranes using spin coating. Spray coating would prove advantageous here, but the crystallization phenomenon observed in Chapter 1 prevented its use. For the experiments documented in this report, the optode membranes were fabricated on OIM posts using droplet evaporation. Due to internal stresses created during the forming process, the epoxy insert posts were slightly concave. This coupled with the surface tension interaction of the THF/Epoxy actually reduced the departure angle of the droplets. As a consequence, the edge effects described in Section 1.3.1 were minimized from the 5mm glass cover slips, therefore creating a more uniform optode membrane. This slight edge effect can be seen in Figure 39, which is a fluorescent intensity image of a single 384 optode insert coated with K-Optode II.

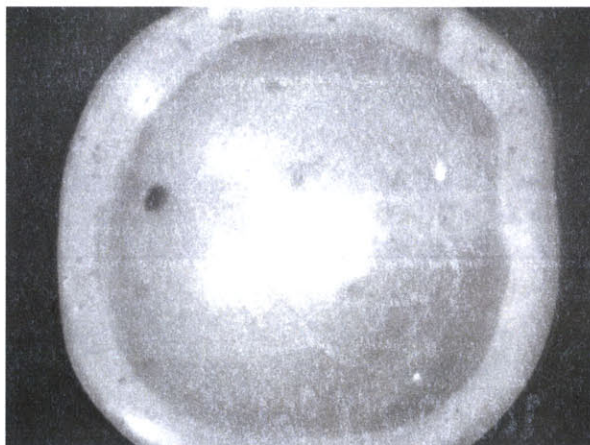


Figure 39: Fluorescent Image of a 384-Well OIM Post Coated w/ K-Optode II

Future prototypes will most likely include removable insert posts that can be individually spun coated. This would produce repeatable coatings with uniform thicknesses. This process would, however, dramatically increase assay preparation time. With proper protocols, micro-sphere deposition could also be used to fabricate optode membranes on insert posts.

Another limitation of the OIM design is its inability to utilize robotic liquid handling. Once the OIM is in place, there is no means of extracting or inserting fluid into the wells. This poses a possible problem since future customers would have to add additional customized robotic hardware to handle the OIMs during screening. Throughout this report, dosing had to be performed prior to OIM insertion, making baseline measurements difficult.

3.2 – Experimental Cell Line: HEK 293

3.2.1: Cell Properties

To test the effectiveness of the OIM system, Human Embryonic Kidney (HEK 293) cells were chosen as the target experimental cell line. HEK 293 cells are an inexpensive adherent cell line used for hundreds of “gold standard” intracellular calcium signaling based assays [57]. Typically, the opening of Ca^{2+} channels is detected using popular intracellular calcium dyes such as Fluo-4 (Invitrogen). hERG transfected HEK 293 cells are also extremely popular in patch clamp hERG screening applications[58]. A serious problem with wild type HEK 293 cells is that they have a shortage of potassium and sodium ion channels when compared to excitable cell lines. For ion channel studies, many groups transfect HEK 293 cells with various families of ion channels to increase ion flux magnitude. This makes transient current flows much larger. The use of wild type HEK 293 cells will make ion channel detection slow and difficult; but will prove the assay as a robust means for detecting extracellular ion flux.

Electrophysiological data regarding various forms of transected HEK 293 cells is abundant; however, detailed information on wild type HEK 293 cells is relatively rare. Membrane capacitance has been measured to be around 17 pF. Surprisingly, the resting membrane potential is reported to be only around -11 mV, which indicates a low conductance to potassium at rest [59]. Almost all excitable cells have a resting potential of around -60 to -90 mV due to the high percentage of open potassium channels. This data indicates potassium channels in wild type HEK 293 cells may not be the primary voltage regulating mechanisms. The effect of intracellular calcium increases on secondary ion fluxes, such as sodium and potassium, cannot be directly determined using published data.

3.2.2: Test Compounds – Isoproterenol and Forskolin

Test compounds for this assay included Isoproterenol and Forskolin. Both are agonists for the A2B receptor, which leads to the production of intracellular cAMP (cyclic AMP) [60]. A buildup of cyclic AMP will cause calcium channels to increase conductivity leading to an influx of calcium ions. Since the compounds do not act directly on calcium channel gating, this process is known as a second messenger signaling system, which is depicted in Figure 40. The A2B receptor has been the target of recent investigation due to its significance as a therapeutic site for inflammation [5, 60, 61]. For this reason, several assays have been developed and optimized to screen for A2B activity using intracellular calcium dyes [62]. The most popular among these assays seems to be the use of Fluo-4 with HEK 293 cells.

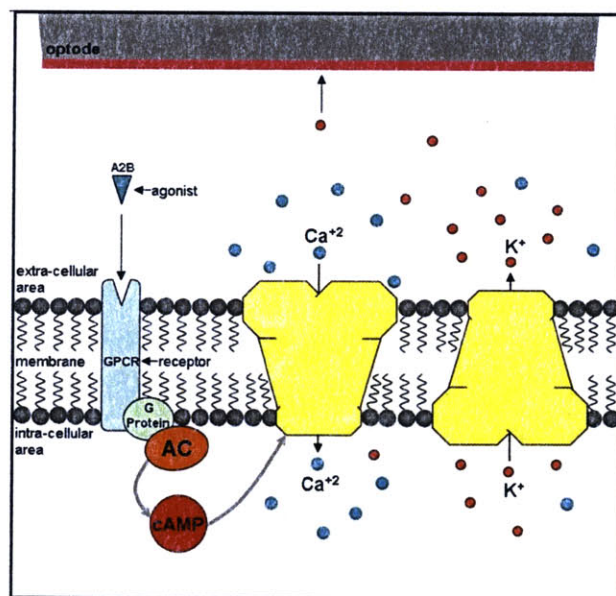


Figure 40: Second Messenger Diagram

Isoproterenol is an extremely potent compound with reported EC₅₀'s between 1 and 10 nM [57]. Forskolin is somewhat less effective with an EC₅₀ between 100 and

200 nM [3, 4]. The 100X difference in EC50s between these two compounds should test the assays ability to accurately measure a compound EC50 value.

3.2.3: Theoretical Response

As stated in Section 3.2.1, there have been few studies detailing ion flux in un-transfected HEK in response to chemical stimuli. To add to this uncertainty, no sources have been located that investigate potassium ion flux from WT HEK 293 cells in a natural environment.

For these reasons, it is extremely difficult to anticipate the potassium ion flux that would result from an increase in intracellular calcium concentration. It is only possible to make an educated guess using simple electrical models governing cellular ion flux.

It has been reported that WT HEK 293 cells have a resting potential of approximately -11.0 mV. Unless potassium pumps are operating at high flow rates, this indicates a low resting membrane conductance towards potassium (closed channels). All compounds listed above are known to cause calcium channels to open. Since the Nernst potential for calcium is approximately 130 mV, calcium will flow into the cell (negative current). Using intracellular calcium dyes such as Fluo-4, studies have shown intracellular calcium spikes as high as 1 μ M [57]. Assuming a membrane capacitance of 20 pF, and no other channel activity, the membrane potential could rise to as high as 25 mV.

By definition, inward rectifier potassium channels open due to a rise in membrane potential. In addition, the $I_{K_{Ca}}$ potassium ion channels open with increased intracellular calcium concentration [2, 63]. Both families of potassium channels are known to exist in HEK 293 cells. Therefore it is likely that high levels of intracellular calcium buildup will cause the membrane conductance to increase towards potassium. This should produce an outward flux of potassium from the cells, which will cause extracellular potassium concentration to increase. The magnitude of this change is difficult to predict with any reasonable certainty.

3.3 – Experimental Methods

3.3.1: Reagents

Human Embryonic Kidney cells (HEK 293) were acquired from American Type Culture Collection (ATCC) (Manassas, VA, USA). Growth medium consisted of standard Dulbecco's Modified Eagle's Medium (DMEM) supplemented with 8.0 % Calf Serum and 1.0 % Penicillin. DMEM also contained 4mM L-Glutamine, 4.5 g/L Glucose, and 1.5 g/L Bicarbonate. 1X Trypsin-EDTA was used during sub-culture to un-adhere the cell monolayer. All growth media components and Trypsin were acquired from ATCC.

For ion flux experiments, the growth media was exchanged with Buffer # 2. This buffer consisted of 10 mM HEPES @ pH 7.4 supplemented with 137 mM NaCl, 2.7 mM KCl, and 0.9 mM CaCl₂. HEPES and salts were acquired from Sigma-Aldrich at the highest available qualities. Tris-HCl and Trizma Base solutions were also used to pre-conditioning optode membranes.

3.3.2: Optode Insert Preparation

All previous optode polymer residues were removed from the peg posts using THF and a fine brush. The insert was then placed in the fume hood for approximately twenty minutes to allow complete solvent evaporation. Following solvent removal, 1.0 mL of K-Optode II was prepared according to the protocol specified in Chapter 1 with a PVC:THF ratio of 10:1 (mg/mL). Approximately 500 μ L of optode cocktail was then applied to a clean 25mm X 50mm class cover slip until the fluid wicked over the entire surface. Optode insert post columns were then dipped into the cocktail bath in series until each post was dipped exactly once. Care was taken to ensure posts and optode droplets were not disturbed after dipping. The insert was then placed with posts facing up in a fume hood and allowed to dry completely for a minimum of two hours. Identical procedures were used to prepare both 96-well and 384-well optode inserts.

Once fully dried, the optodes were pre-conditioned to fully expel all potassium ions associated with KTFPB. The insert was placed in a 96/384 well plate containing a 500 mM K⁺ Tris Buffer (pH 7.4) for 10 minutes. The insert was then removed and all posts were submerged in an 18 M Ω de-ionized (dI) water bath for 2-3 min. The unit was then placed into a second 96/384 well plate containing 500 mM Tris-HCL (pH 4.5) for an additional 20-25 minutes. Once complete, posts were rinsed with 18M Ω dI H₂O and placed back in the first 96/384 plate containing Buffer # 2 for at least 20 min until transfer into the testing plate. Identical procedures were followed for sodium optodes (with sodium buffer instead).

3.3.3: HEK 293 Culture and Proliferation

HEK 293 cells were maintained in DMEM (Dulbecco's Modified Eagle Medium) supplemented with 8.0 % Calf Serum and 1.0 % (Antibiotic) at 37°C and 5.0% CO₂. Cells were typically grown in (Flasks) with 10-14 mL growth medium. Once cells achieved 90% confluence they were split at 25% seeding dilutions. Cells reached 90% confluence approximately 48 hours after splitting.

Cells were detached using 2.0 mL 1X TYPSIN-EDTA from ATCC. Old media was first extracted and the flask was rinsed with 4-5 mL Dubelcos Phosphate Buffered Saline (DPBS) to ensure removal of all anti-trypsinizing agents. The time required to detach 100% of the cell monolayer ranged from 3-8 minutes depending on confluence and temperature. Once fully detached, 8.0 mL growth medium was added to halt trypsinization. Cell clumps were broken up by triturating with a 10.0 mL stereological pipette (approximately 20 cycles). Then 5.0 mL cells/medium mixture was discarded and the remaining 5.0 mL was split between two new flasks (2.5 mL each). An additional 7.5-11.5 mL medium was added to each flask to complete the splitting procedure.

3.3.4: Assay Protocol

HEK 293 cells were seeding into Nunc Poly-d-Lysine optically clear black 96- or 384-well plates 24 hours prior to run time. Wells were seeded at a very high density of

approximately 50,000 cells/cm². Despite the possibility of cell death, this was essential to achieve sufficiently high signal to noise ratios. Prior to assay run, growth medium was removed by plate inversion and slight agitation. Wells were rinsed twice with Buffer # 2 to ensure complete media removal. Following rinsing, 100 μ l / 20 μ L of Buffer # 2 was added to each well (96 or 384 respectively). Buffer was then removed with an eight channel multi-well pipette to achieve final well volumes of 20 μ L / 4 μ L (96/384). The OIM was inserted into the plate and the entire assembly was placed in a 37°C 5.0 % CO₂ incubator for 20 minutes to achieve a uniform temperature distribution. In addition, this pre-incubation was necessary to allow cellular ion flux to return to equilibrium. It has been reported that changing the media with HEK 293 cells could result in intracellular calcium buildup. If this occurs, a 20 min baseline should allow sufficient time for the cells to return to equilibrium.

After the 20 min settling time, the OIM was removed and placed into a separate plate containing 50/20 μ L of a 5X dosing solution brought up in Buffer # 2. Each optode post will pick up approximately 1.1 / 0.28 μ L (96/384) of solution. The insert was replaced into the test plate and inserted into the Molecular Devices Gemini EM plate reader pre-heated to 37°C

For the 96 well plate, three wavelength setting (ex 485, em 570: ex 485, em 670, and ex 570, em 670) were used to scan the plate at 1.5 minute intervals. Due to scan time constraints, only one wavelength was used (ex 570, em 670) for an entire 384 well plate. This was necessary to obtain an acceptable amount of data points, but was limited to single peak analysis. After a 60 min run, the data was exported to a .txt file where it was processed by the custom Matlab code described in the proceeding section. Depending on the type of analysis, the code is programmed to generate a variety of response curves.

3.3.5: Data Processing

EC50 curves were generated using the following protocol, which follows many industry standards. A standard 96 well plate is used in this example, but analogous protocols exist for 384 well plates. The dosing setup in the plate is laid out according to the diagram in Figure 41.

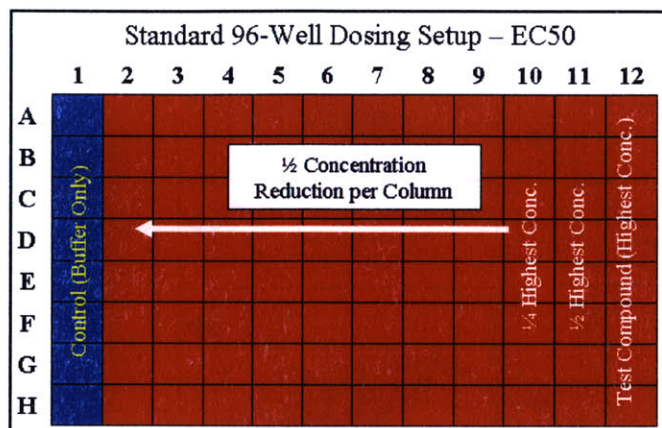


Figure 41: Dosing Setup for EC50 Assays

Each column of wells represents an individual dosing concentration. This yields n=8 for 96 well plates and n=16 for 384 plates. This allows for 12/24 test concentrations for 96/384-well plates. The first column of each plate represents the controls. In all eight of these wells, only Buffer # 2 is added with no compound. The next column of wells has the lowest dosing concentration and each succeeding column has double the drug concentration of the previous one. This dosing interval creates an even three point per decade distribution, which will generate a high content EC50 curve.

To normalize the kinetic data for each well, every point in the time series was divided by the first. After this, a series of simple techniques can be used to determine the “activity” of the well. For this application, experimental results suggested using the area under the normalized curve for the first 30 minutes after dosing. This method is also used by several other sources as a reliable means for determining EC50 data. Once the area was calculated for each optode, the average and standard errors could be calculated for each column of wells. Test column averages were then subtracted from the control value and plotted against concentration. Using least squares, a sigmoidal curve is fit to the data and the EC50, or inflection point, can be calculated. Resulting plots include normalized kinetic data and EC50 curves with error bars. All data processing was performed with Matlab 7. Plots were generated using Origin 7.5 and GraphPad Prism 4. Figure 42 shows step by step how the kinetic test data was used to generate EC50 curves.

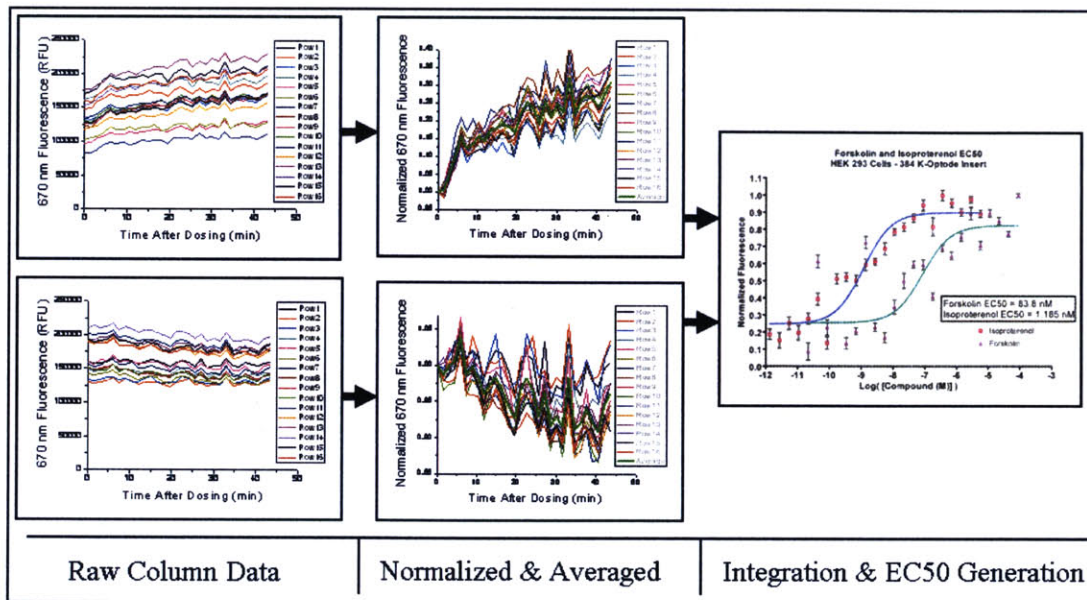


Figure 42: EC50 Curve Generation with Kinetic Data from HEK 293 Cells Dosed with Isoproterenol

3.4 – Results and Discussion

3.4.1: Isoproterenol and Forskolin EC50s'

Using the protocols outlined in section 3.3.4 and 3.3.5, EC50 curves were generated for Isoproterenol and Forskolin with HEK 293 cells. The average fluorescent intensities were used to generate the EC50 curves shown in Figure 43.

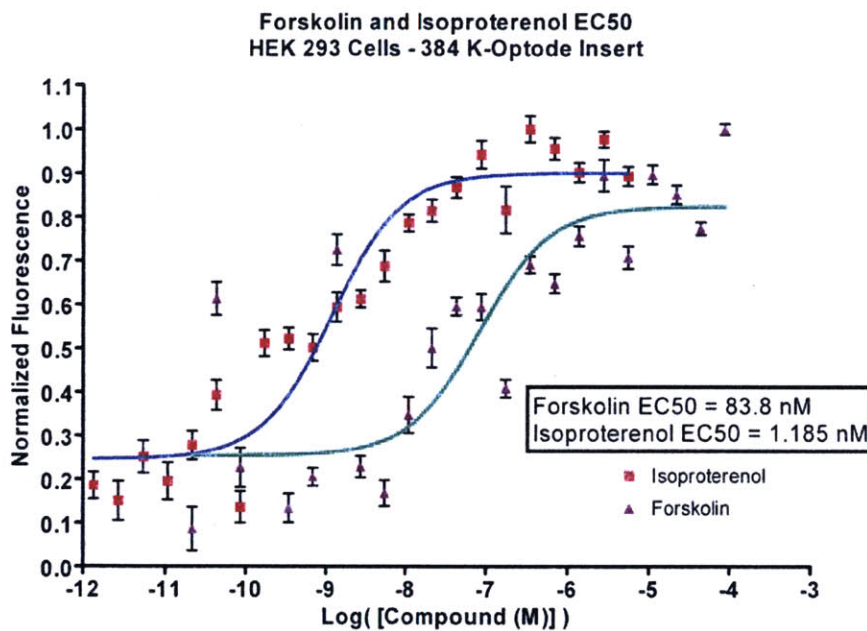


Figure 43: Dose Response Curves for Forskolin and Isoproterenol w/ HEK 293 Cells

The dose response curves indicate EC50 values for Isoproterenol and Forskolin of 1.185 nM and 83.8 nM, respectively. It is somewhat difficult to quantify the accuracy of these values due to the discrepancy in published EC50 values for Isoproterenol and Forskolin. Experimental variables such as cell type, temperature and cell density can all shift the effective dose of a compound. Reported EC50 values ranged from 1.0-100 nM for Isoproterenol and 100-5,000 nM for Forskolin [3, 4]. Both curves in Figure 43 indicate EC50 values at the lower end of these spectrums, which indicates the assay has a high sensitivity for compound binding.

The vertical axis in Figure 43 represents normalized fluorescence. In actuality, the higher doses produced a drop in 670 nm fluorescence intensity. As the response curve in Chapter 1 indicates, a drop in 670 nm fluorescence indicates an increase in extracellular potassium concentrations. This is consistent with an increase in intracellular calcium, which was predicted for this model system. Using the initial fluorescence intensity at 2.7 mM potassium, intensity changes indicate potassium concentration increases as high as 200 μ M among high dose wells.

It is interesting to note that the error bars reduce in magnitude as compound concentration increases. The number of samples ($n=16$) is held constant across all concentrations, so the reduction in magnitude is a direct result of smaller signal deviation around the mean. This implies that higher doses resulted in a more consistent cell response. This phenomenon could very well be the result of spontaneous calcium channel activation in the lower compound concentration wells. Reports have shown that HEK 293 cells can activate calcium channels as a response to changes in extracellular media [57]. The cell washing procedure performed 20 minutes prior to the test run could

easily initiate such a response. This would cause outward potassium currents even in a random population of lower dose wells, which would explain the high standard deviations. Future experiments could include a simultaneous Fluo-4 intracellular calcium assay to investigate this theory.

Overall, this assay produced acceptable EC50 curves using potassium flux as a biomarker. EC50 values fell within published values and the data displays the typical sigmoidal dose-response curve. Using the 384-well plate allows for 23 doses with n=16 for each concentration. This large sample population supports the validity of these experiments and strengthens the performance of this assay. HEK 293 cells do not express a large amount of potassium ion channels. Future experiments with more active cell lines should theoretically produce even stronger assay performance.

3.4.2: Z-Factor

A universal dimensionless parameter has been developed in recent years to assess the effectiveness of whole cell based assays [64]. This parameter, referred to as the Z-Factor, is used by countless research laboratories and pharmaceutical companies to rate assay performance. The Z-factor is a measure of the assay's ability to confidently detect biologically active wells. The calculation of this parameter is performed using two sets of known active and inactive samples. The mean and standard deviation of each data set is used in the following equation to calculate the assay Z-Factor.

$$Z = 1 - \frac{3 * SD_{active} + 3 * SD_{inactive}}{|\sigma_{active} - \sigma_{inactive}|}$$

SD = Standard Deviation

σ = Mean

Equation 20: Z-Factor Calculation

A Z-factor of unity indicates an ideal assay that has perfect discrimination between active and inactive samples. As shown in Equation 20, a high Z-factor will only be produced with very low standard deviations, regardless of overall mean signal difference. Typically, a Z-factor around 0.5 is deemed a highly acceptable assay and will yield a minimal amount of false positive and false negative results. Values between zero and 0.5 are acceptable. A Z-factor below zero shows poor ability to differentiate active and inactive wells and should not be used as a reliable screening assay.

The Z-Factor for this assay is calculated using the experimental data in Figure 43. The sixteen control wells served to define the inactive data. The “active” cell data was obtained from a column of high dose wells (typically at the crest of the EC50 curve). The following figure shows the data sets and the resulting Z-Factor for this assay.

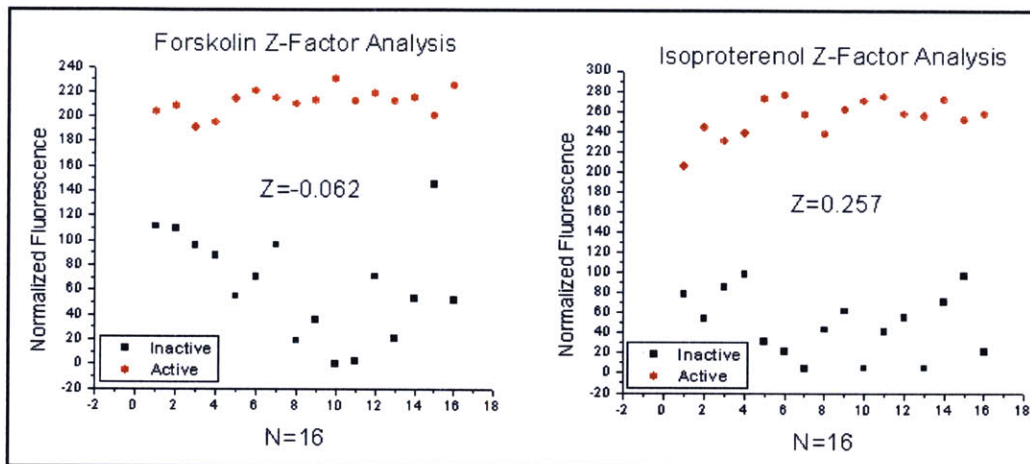


Figure 44: OIM Z-Factor Analysis

The Z-factor for the Forskolin assay was calculated to be slightly negative at -0.062. This negative value is a direct result of the large standard deviation present in the inactive data set (black square data points). Visually, it is easy to discriminate between the active and inactive wells, but the Z-factor equation heavily weights standard deviation. As stated previously, this is most likely the result of random calcium signaling from un-dosed wells. Refined washing protocols should theoretically increase the Z-factor of this assay.

The right panel of Figure 44 shows active and inactive data sets from the Isoproterenol assay. The resulting Z-factor is calculated at 0.257, which is interpreted as a moderately effective assay. The reason for the increase in Z-factor over the Forskolin assay is the reduction in standard deviation of the control wells. There is no logical reason why this should be the case, but the data shows clear improvement. It is most likely the result of a difference in cell viability or washing protocol the day of the experiments.

It must be noted that the Z-factor for any assay is strongly dependant on the particular cell line and dosing compounds. For this reason, the above Z-factors should be considered “worst case scenario” values. Using HEK-293 cells with additional transfected ion channels would dramatically increase the magnitude of compound induced ion flux. This would have a direct effect on optode signal, which would increase the resulting Z-factor. It should be noted that the HEK-293 assay detailed above was only a validation of system functionality and does not prove highly relevant pharmacological data.

Chapter 4: hERG Screening Assay

This chapter introduces a novel sensor system that employs potassium optodes to measure real time potassium flux magnitude from beating cardiac myocytes. The measurement of potassium flux during a series of action potentials could be an extremely effective method for measuring the extent of hERG potassium channel blockage caused by arrhythmic compounds. Section 4.1 introduces neonatal mouse cardiac myocytes as a model cell line to test this novel assay technique. Basic cell properties and electrophysiology are reviewed. Section 4.2 uses the Nygren atrial cell model to predict the theoretical changes in potassium concentration that will occur with a series of action potentials. A first order optode model is also introduced.

Section 4.3 introduces several prototype systems that allow the detection of extracellular potassium through precise optode placement. A detailed description of these sensor systems is presented and their performance limitations are discussed. The remaining two sections describe several “proof-of-concept” experiments used to validate the system.

4.1 – Target Cell Line: Neonatal Mouse Cardiac Myocyte

4.2.1: Cell Properties

Neonatal mouse cardiac myocytes are harvested from donor mice immediately prior to seeding. Unlike adult myocytes, these cells are spherical in shape and flatten out upon adhesion to the substrate material. Studies indicate the membrane capacitance for a single cell to be on the order of 30 pF, which is almost ten times lower than adult cells. The physical dimensions of these cells are on the order of 20 by 20 by 5 microns [65].

Approximately 12-20 hours after seeding the cells will begin to contract spontaneously. Patch clamp studies have revealed these action potentials to cause a peak membrane voltage of +34 mV with a resting potential of -83 mV. When viable, action potential durations (APD) are approximately 42 milliseconds (at 90% resting potential). Individual ion channel analysis has shown these cells to have a highly dominant $I_{K_{10}}$ current. This is the rapid rectifier current that activates at the onset of the action potential. This accounts for the sharp initial voltage spike and overall short APD. As an unfortunate consequence, these cells have a relatively low percentage of I_{K_r} channels when compared to human ventricle cells. This will reduce the affect of I_{K_r} blocker compounds on overall potassium flux [65].

4.2.2: Test Compounds - Haloperidol

The majority of experiments conducted in this chapter are designed merely to examine the systems ability to detect potassium flux during natural action potentials. However, one experiment was conducted to examine the effects of Haloperidol on potassium flux magnitude during a train of action potentials. Haloperidol is an extremely effective blocker of hERG I_{K_r} channels, which is a primary cause of arrhythmia and

Torsades de Pointes [16, 25, 66]. Haloperidol has also been shown to lower the current through voltage gated IK_s channels [67].

Unfortunately, in addition to being an effective channel blocker, Haloperidol has strong binding affinities for many other biological sites such as the sigma and dopamine receptors. The activation of these sites could very easily affect the function of potassium channels [56].

4.2 – Theoretical Response: System Modeling

4.2.1: Model Generation: Modified Nygren

Prior to conducting in vitro experiments, it was necessary to develop a theoretical model of an excitable cell encased in a small extracellular environment. This model was used in conjunction with sensor data to assess the feasibility of this system to measure extracellular potassium fluctuations. The mathematical model for the human atrial cell developed by Nygren was an excellent tool for simulating action potentials in excitable cell lines [15]. This model has been coded by several open sources in Simulink and is available from the Math Works website. Aside from ion channel properties, several input parameters were modified to properly model the optode based systems described in the subsequent sections.

First, the cells used to evaluate these sensor systems are neonatal mouse cardiac myocytes, not human Atrial cells. This required dropping the membrane capacitance from 50 pF down to 30 pF. Not enough information existed to re-define the ion channel ODE's parameters for a neonatal mouse cardiac Myocyte. For the scope of this report, the equations governing channel properties will be left unaltered.

In its stock form, the Nygren model represents the extracellular environment as an extremely low volume spherical chamber encasing the cell. This volume is referred to as the "cleft space". The default volume of this region is only 14% of the cytoplasm, which is itself only 0.006 nL. For both detection systems in this report, the extracellular environments are larger. At best (high cell density with the cell chamber), the average volume per cell has been estimated at approximately 8,000 cubic micrometers (20 by 20 by 20 micron cube) or 0.008 nL. Subtracting the estimated cell volume (0.004 nL scaled for the smaller Myocyte), this gives a net extracellular volume of 0.004 nL, approximately four times larger than the default cleft space volume. This will reduce the amplitude of the extracellular concentration fluctuations originally reported by the model [15].

Many experiments conducted in this report were performed at reduced extracellular potassium concentrations (2.7 mM) to maximize sensor performance. Unfortunately, the model was unable to accommodate modification of this parameter. Simulations with extracellular potassium concentrations below 3.0 mM showed highly arrhythmic behavior. No such behavior was noticed with neonatal mouse cardiac myocytes during testing. It will be assumed for the remainder of the report that the estimated magnitude of extracellular potassium oscillations will be similar regardless of equilibrium concentration.

4.1.2: Model Output

Before reviewing model output, it must be noted that the human atrial cell is biologically quite different from the neonatal mouse cardiac myocytes used in this report. For this reason, the following results are only estimations of actual ion currents. The primary goal of these simulations is to anticipate trends and estimate the required optode resolution.

To assess the feasibility of these sensor systems, two simulations were performed. Simulation 1 does not alter cell function in any way (no ion channel blocking). This simulation will act as the control. This simulation was also used to estimate natural potassium concentration fluctuations in the extracellular environment. Figure 45 shows the resulting membrane potential and ion currents during a seven second 1.0 Hz stimulation frequency simulation.

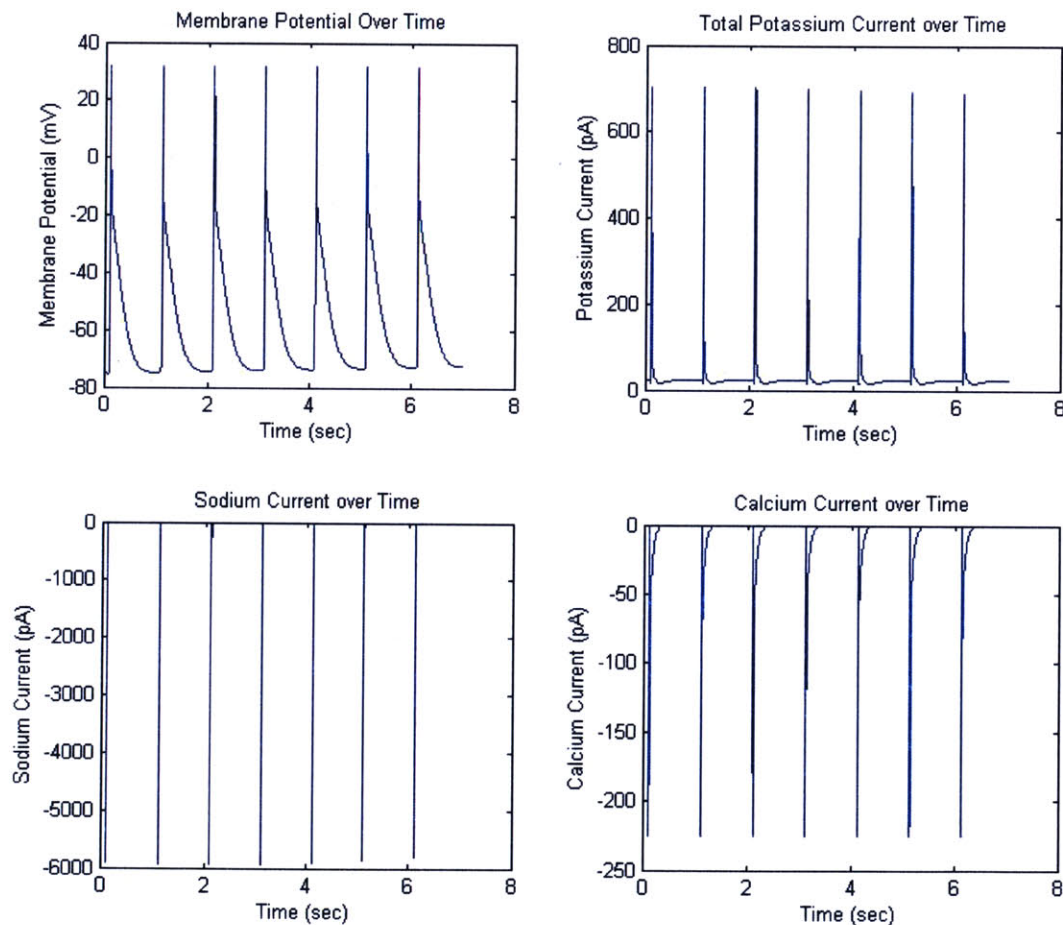


Figure 45: Nygren Model Output (Potential and Currents)

The results show steady state 1.0 Hz signals across all four panels of Figure 45, which indicates complete ion recovery after each action potential. Both sodium and calcium plots (lower half) show extremely high inward current spikes at the onset of the action potential. After peak voltage is achieved (30 mV), the sodium channels completely inactivate. The calcium channels appear to have a slightly slower de-activation extending several milliseconds into the action potential. The potassium current spikes are caused by a combination of I_t and I_{sus} currents that quickly activate upon membrane de-polarization. Potassium current data is expanded further in Figure 46, which shows individual channel currents along with extracellular concentration.

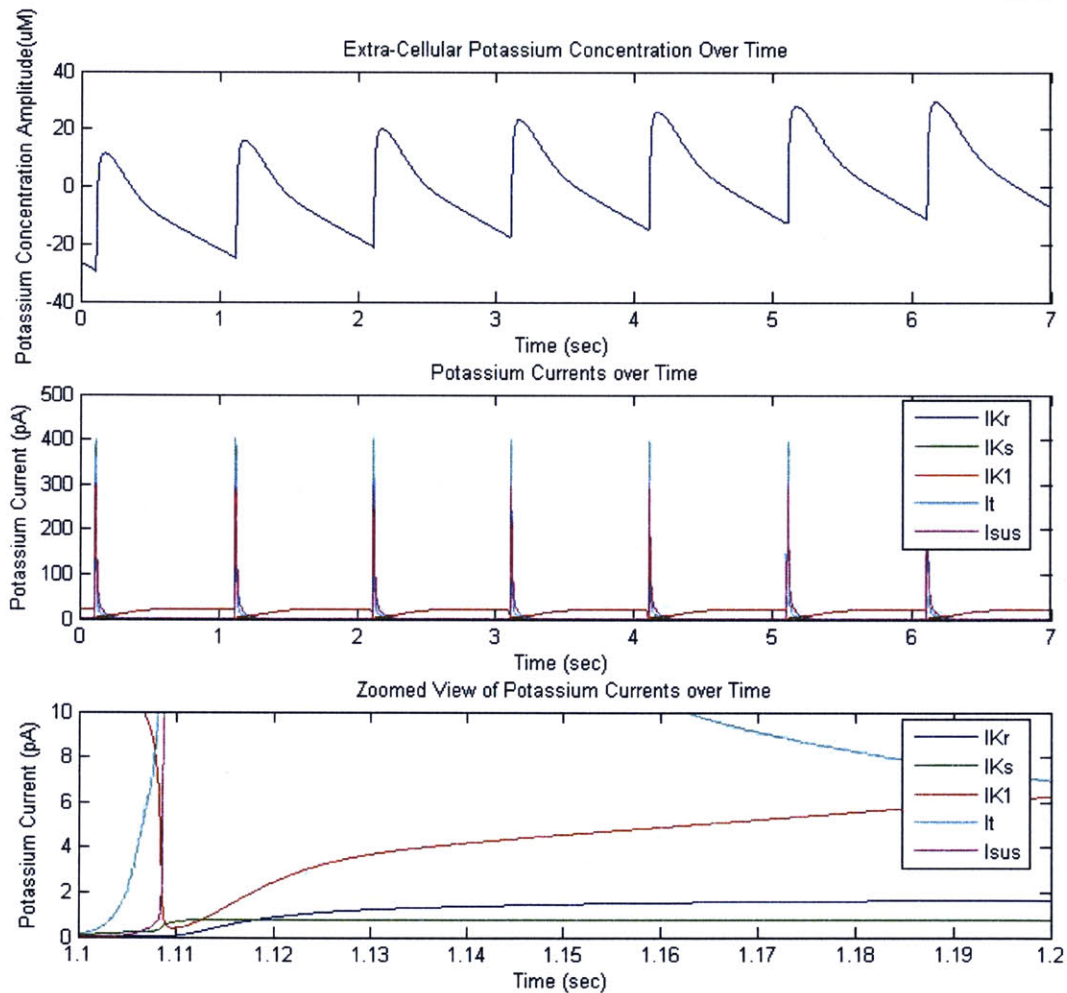


Figure 46: Nygren Model Output (Potassium Currents and Concentration)

The center plot of Figure 46 shows the five individual potassium currents throughout the seven second simulation. I_{Kr} , I_{Ks} , and I_{K1} components are completely dwarfed by the I_t and I_{sus} currents at the onset of the action potential. The lower panel in Figure 46 further accentuates the magnitude of I_t and I_{sus} with respect to the remaining

three currents. These results indicate a difficulty in measuring I_{Kr} block through the net potassium current. However, it must be noted again that the individual channel properties differ greatly between cell lines.

The upper plot in Figure 46 displays the most relevant simulation data for this study. In the estimated extracellular volume, the plot indicates potassium concentration fluctuations on the order of $50 \mu\text{M}$, which just falls within the resolution of the K-Optode II produced in Chapter 1. Though very small with respect to average concentration (2-4 mM), these changes may be detectable with high precision optics. These results are similar to actual extracellular potassium concentration fluctuations measured with potassium selective electrodes in the interstitial space of cardiac tissue [68].

To estimate the effects of potassium channel failure, a secondary simulation was performed with I_{sus} channels completely blocked. Ideally, I_{Kr} channels would be used to simulate this effect, but their current contribution in the atrial cell model is too small. Figure 47 is identical in format to Figure 45, but shows the effects of blocking 100% of I_{sus} channels.

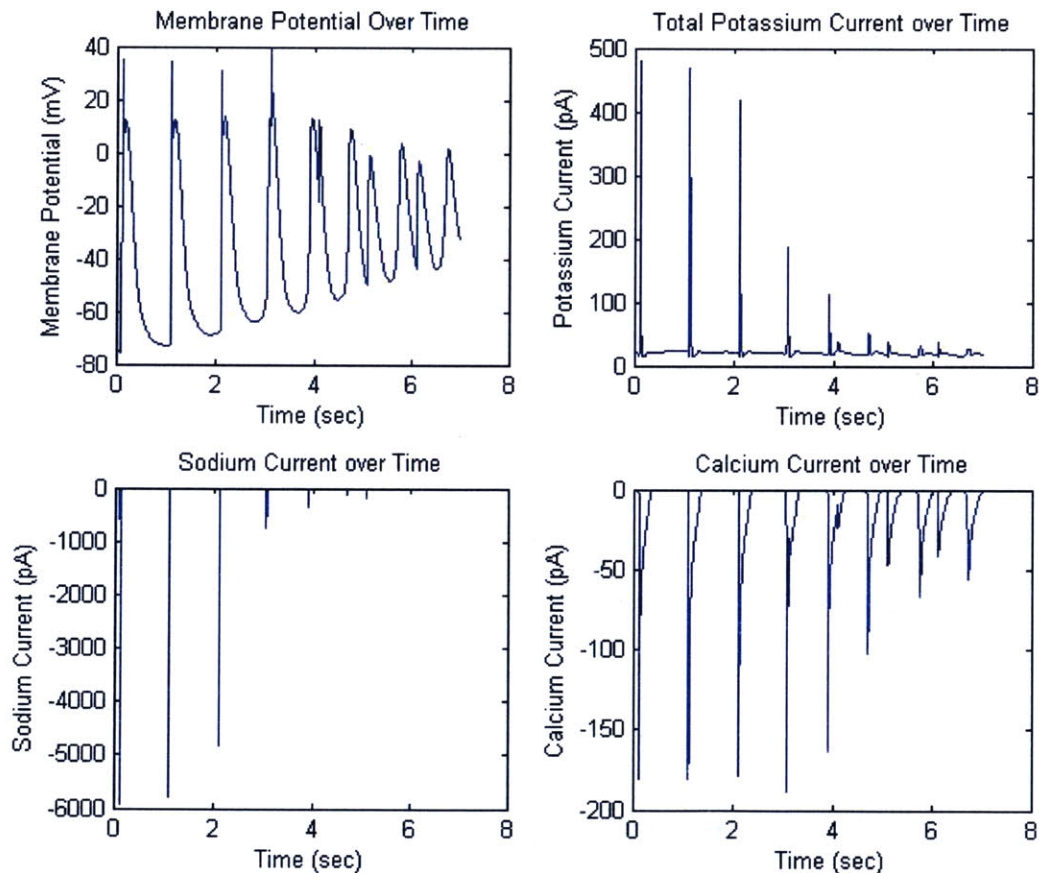


Figure 47: Nygren Model Output with I_{sus} Block (Potential and Currents)

The first two action potentials appear relatively stable. The shape of the membrane potential curve is slightly different than simulation 1, but no severe features

are noticeable. After only four seconds, the beat pattern becomes completely unstable and displays characteristic arrhythmia. The membrane potential trace in the upper left panel shows the common “double beat”^V phenomenon, which was also seen in laboratory experiments. This most likely occurs from sodium channels’ re-activating before the membrane potential has fallen below the “launch voltage”^{VI}.

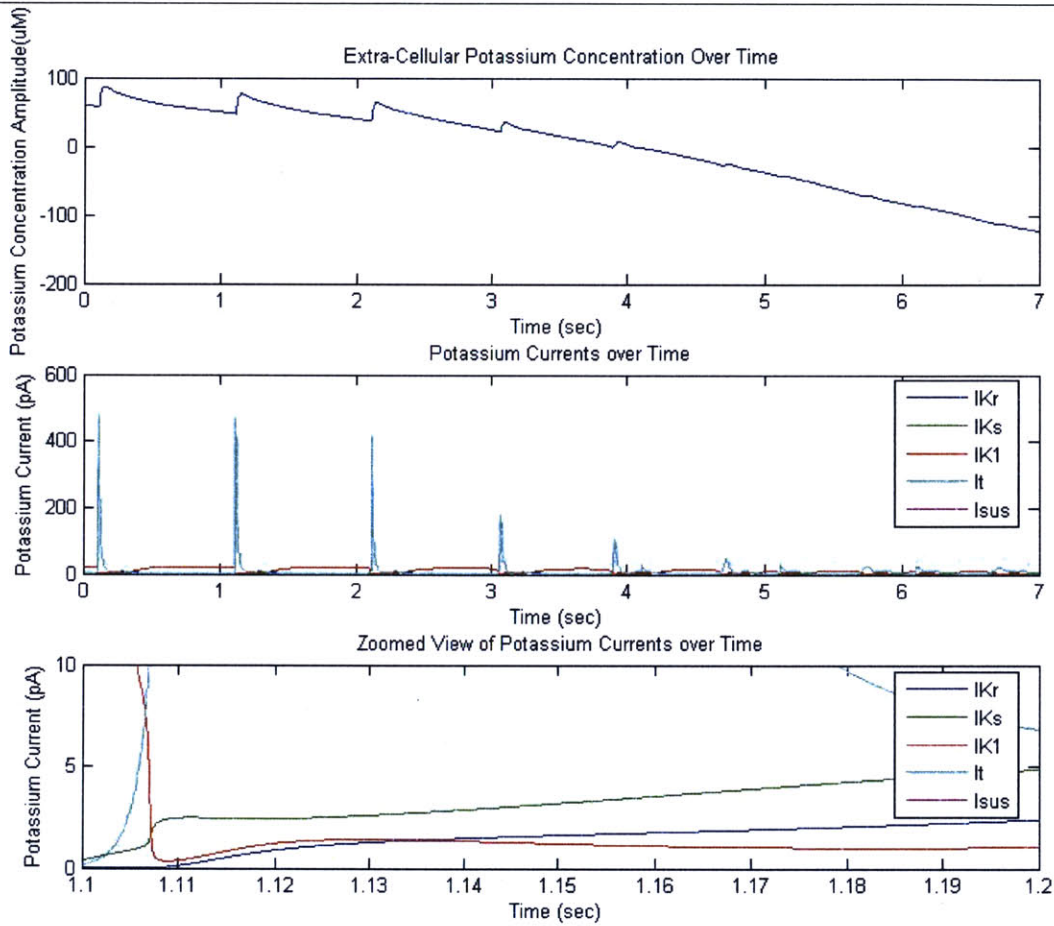


Figure 48: Nygren Model Output with Isus Block (Potassium Currents and Concentration)

Figure 48 displays the same variables presented in Figure 45. It is interesting to note the increase in I_{Kr} and I_{Ks} over the baseline simulation (shown in the lower plot). Their average intensities more than doubled as a result of I_{sus} block. As expected, the I_{sus} is eliminated from the center plot and virtually all the potassium current is being dominated by the I_t channels.

^V “Double Beat” refers to an un-stimulated secondary increase in membrane potential before the end of an action potential

^{VI} “Launch Voltage” is the minimum membrane voltage required to activate sodium channels and initiate an action potential

The upper panel in Figure 48 indicates a change in both shape and intensity of extracellular potassium fluctuations resulting from I_{KUS} block. There is also an apparent long term reduction in extracellular potassium concentration over time. This is indicative of potassium pumps transferring more ions into the cell than the channels are releasing over the series of action potentials. This long term concentration change may also be useful in quantifying ion channel blockage.

Overall, these two simulations indicate that it is feasible to detect extracellular potassium fluctuations using an optode. However, due to the small concentration changes, it is anticipated that signal filtering will be required to attenuate any noise in the system. The simulations also give insight to the effects of blocking potassium channels. Obviously, the above results will differ with actual mouse cardiac myocytes, but it is clear that a detectable change will occur from potassium channel blockage.

Due to the high cyclic rates required for this system (1 Hz), optode dynamics will have an affect. Section 1.4.6 showed that optodes could be accurately modeled with first order response. To investigate the affect of optode dynamics on flux measurement, a Matlab based model was developed to simulate the system. The model uses potassium concentration fluctuations as the plant input. The output is the observed potassium fluctuation as reported by the optode fluorescence.

For a sample simulation, the extracellular potassium concentration data in Figure 46 was used as input data for this model. Optode response time was set to 1.0 second (63% response) to exaggerate the effects of optode lag. The resulting simulation data is shown in Figure 49 (Increased extracellular volume).

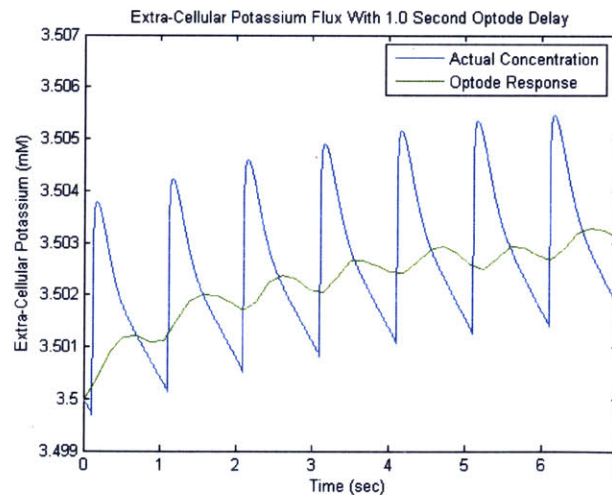


Figure 49: Simulated Optode Response to Potassium Oscillations

As the plot indicates, there is a drastic reduction in observed signal magnitude. There is also a phase delay, which will make it difficult to synchronize potassium oscillations with stimulation timing. Optode dynamics can be minimized in two ways. The first technique is to reduce the optode response time below 20-40 milliseconds. This

should produce accurate signal tracking permitting the stimulation frequency does not exceed 2.0 Hz. The second method is to measure the exact response time of an optode prior to experimental testing. This would allow the original signal to be recreated by taking into account the derivative of the observed signal. This is not recommended since it will amplify any noise and is highly dependant on accurate response time calculations. For all the experiments detailed in the following sections, optode response time was kept between 10 and 50 milliseconds.

4.3 – System Properties

4.3.1: Applications

This assay is specifically designed to measure extracellular potassium flux from excitable cell lines, primarily cardiac myocytes. This technology has been developed solely for the detection of drug induced channel blocking (specifically hERG). The reason for this is the high demand for alternative high throughput hERG screening technologies.

In principle, this system could be used for any additional application requiring the measurement of extracellular potassium flux. Essentially, any application that requires patch clamping for potassium channels in excitable cell lines could be replaced or augmented by this technology.

4.3.2: Design Criteria

Cardiac myocytes are an adherent cell line, so they will form a monolayer of cells over whatever substrate they are deposited onto. In this case, the desired substrate is the bottom of a standard multi well plate or glass cover slip. Assuming all cells are beating in sync, a single action potential will cause a coordinated release of potassium ions. The goal of this system is to measure this ion flux using a potassium optode positioned within the well close to the monolayer.

Ultimately, it is desired that this system can be used with standard 96- and 384-well plates. This will increase throughout and reduce cost. However, this application introduces a series of additional problems not encountered by the assay developed in Chapter 3. To simplify system design, the initial system was designed for use in standard 12-well plates.

The first requirement of this system is the need to electrically stimulate the monolayer of cardiac myocytes. This is commonly accomplished using a parallel set of electrodes in the well. An electrical pulse (5-10 millisecond duration) across the electrodes will generate an electric field in the salt solution surrounding the cells. This electric field causes one half of the membrane to increase potential, which will trigger the activation of sodium channels. Once activated, the sodium channels will continue to drive the membrane potential and an action potential will ensue. Field stimulation will cause the cells to release potassium in sync and provide a reference frequency to be used

in data analysis. The ability to pace the cells at various frequencies is highly valuable in measuring ion flux characteristics.

Another system requirement is the placement of the optode membrane that would allow reliable optical measurements. As discussed in Chapter 3, this has been achieved by positioning the optode membrane parallel and in close proximity to the bottom of the well. This will maximize the signal to noise ratio and reduce scatter.

The system developed in Chapter 3 is designed to measure long term potassium flux on the order of 20 minutes. This relaxes the constraint on response time allowing the use of thicker (higher fluorescent signal) optodes. With cardiac myocytes, the beat frequencies are in the neighborhood of 1 Hz. Ideally, this requires the optode to have a 66% optical response time of less than 100 milliseconds. The faster the response time, the more information gathered regarding potassium flux. Creating an optode membrane this thin is feasible using spin coating techniques; however, the overall fluorescent intensity will be low. As a result, this will reduce the signal to noise ratio of the system.

Finally, the extracellular fluid volume must be kept as low as possible to maximize changes in extracellular potassium concentration. Even with a 20 μM thick fluid layer over the cells, the simulations in Section 4.1.3 predict very small changes in potassium concentration during an action potential. The optode membrane must be positioned as close to the cell monolayer as possible without disrupting cell contraction.

4.3.3: Design 1: CSOS

The above design considerations were addressed through a prototype device referred to as the CSOS (Cell Stimulating Optode System). Figure 50 shows the solid model for this assembly drawn in SolidWorks 2005. The CSOS consists of two polymer parts that press fit together to form a single unit.

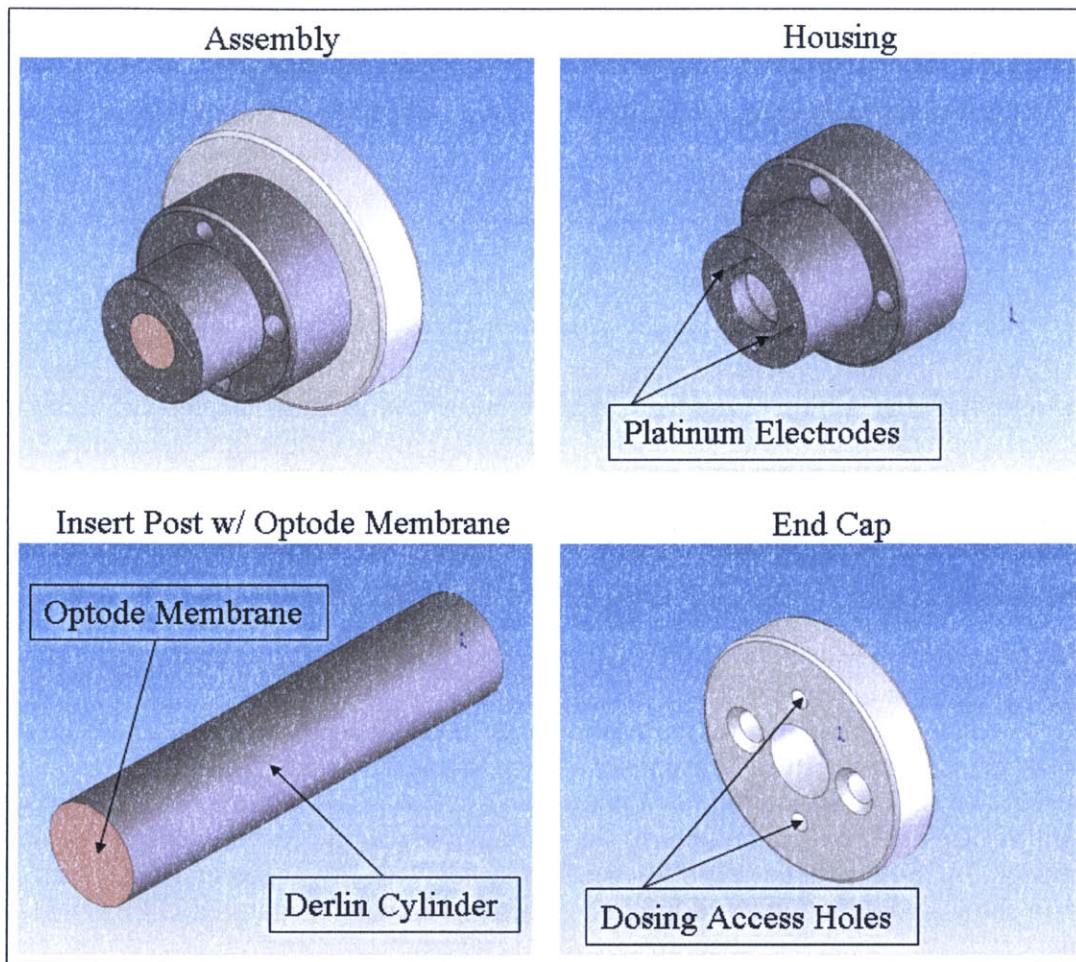


Figure 50: Solid Model Drawing of the CSOS (Cell Stimulating Optode System)

The outer part (housing) was machined out of a solid black Derlin® cylinder. The large diameter section rests on top of the well to fix the height. The distance from this section to the bottom of the housing determines the clearance of the optode membrane over the cell monolayer. The second section of the housing creates a high tolerance fit in the upper portion of the well. This helps to prevent movement during testing and reduces evaporation. The housing is then reduced to a final diameter, which is slightly larger than half the diameter of the well. This size prevents bubble formation while still covering a large area of the well.

Two parallel platinum electrode wires were embedded along grooves in the bottom of the housing. These electrodes serve to generate a field stimulated region of cells in the area between them. Through the center axis of the housing a 1/4" hole was drilled to allow clearance for the optode cylinder.

A thin K-Optode II membrane was formed on the end of a 1" Derlin® cylinder (insert cylinder) by spin coating. A custom motor shaft attachment was used to hold the cylinder vertical at high rotation rates. Prior to testing, the cylinder was manually pressed

into center of the housing until the membrane is flush with the bottom. The prototype system was designed to have a clearance between 50 and 100 microns over the bottom of a BD Falcon 12 well plate.

Removal of the insert cylinder allows for monolayer imaging using transmitted light. This was essential when calibrating the system to achieve optimal field stimulation protocols. Any standard function generator can be used to field stimulate the cells.

4.3.4: CSOS Limitations

The CSOS device has several positive design characteristics, but there is a single limitation that has the potential to cause signal interference. The optode is designed to be imaged through the bottom of the well, just like the system used in Chapter 3. Since most cell membranes have a relatively low absorbance in the visible light spectrum, their optical properties have little influence on fluorescent signal. Even if they do, it is unchanging throughout the run time of the assay. With cardiac myocytes; however, the cells contract with every action potential. These contractions change the shape of the cell and alter light transmittance. Since the contractions are in sync with potassium signaling, this motion artifact may appear to be a change in potassium concentration. Mathematical models have been presented to compensate for such artifacts, but they would be extremely difficult to apply to this application [46].

A secondary drawback to the CSOS prototype is the inability to accurately control the fluid gap distance between the optode and the bottom of the well. This dimension is critical in controlling the amplitude of potassium oscillations over at the optode interface. For future designs, the use of reference shim would allow tight control over this dimension. A solid model of a modified CSOS system was developed in SolidWorks 2005 to show a possible future design. The assembly drawing is pictured in Figure 51 below.

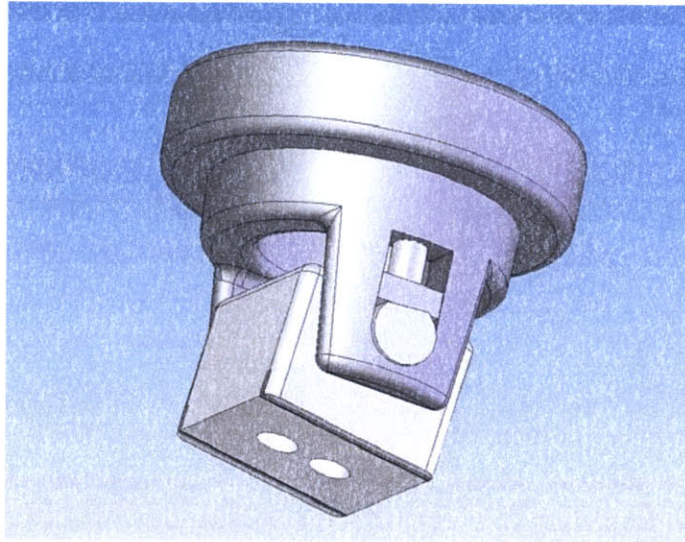


Figure 51: Solid Model Drawing of a Future Prototype CSOS

The parallel electrodes would accurately control the height of the optode membrane over the cells. The electrode and optode housing are hinged to prevent bubble formation upon insertion into the well. The housing contains two insert holes, which would permit multi-optode measurements. A potassium and calcium optodes could be used simultaneously to provide highly useful ion flux information.

4.3.5: Design 2: Stimulation Chamber

The design limitations of the CSOS device discussed in the previous section warranted the development of an alternate system to measure potassium flux. The system needed to eliminate any possibility of motion artifact and allow tighter control over the fluid gap between the cells and optode membrane.

This secondary system is relatively simple when compared to the CSOS. It consists of two parts that hinge together to form a submerged stimulation chamber with two glass cover slips. Figure 52 shows the solid model drawing of the chamber assembly.

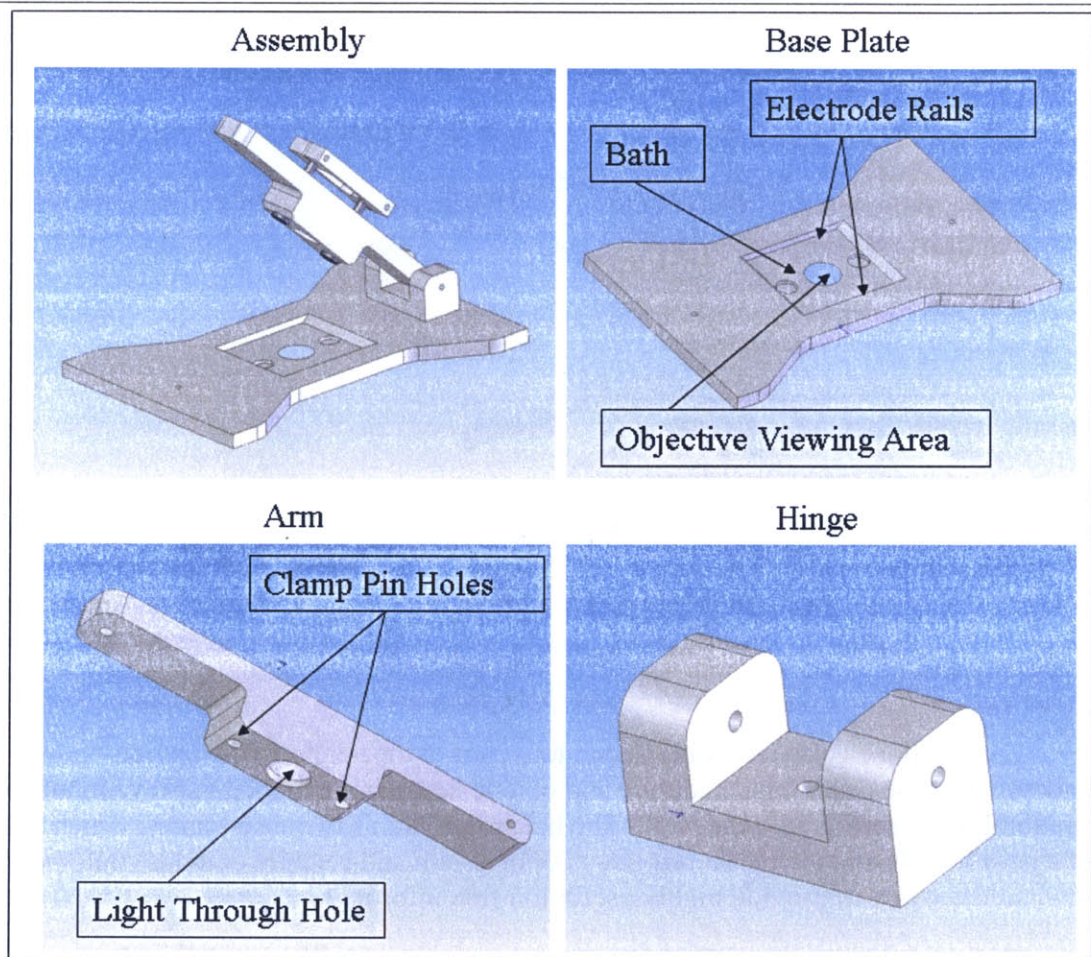


Figure 52: Solid Model Drawings of the Stimulation Chamber Assembly

The base plate has the exact outer dimensions of a multi-well plate, so it is easily clamped into any standard microscope stage adaptor. In the center of the base plate is a 2.5 mm deep 35 mm by 35mm cutout that is used as the stimulation bath area. A single 22mm by 22mm No. 1 glass cover slip is spun coat with optode membrane and secured over the center through-hole with vacuum grease. The sides of the cover slip are parallel with the sides of the bath cutout. The vacuum grease creates a strong seal preventing leakage or movement under normal operating conditions. On either side of the glass cover slip are two strips of 25 micron silver chloride foil secured to the base using adhesive spray. The thickness of the glass slide is approximately 150 microns, so the foil rests well below the upper surface of the disk. The entire sunken area is filled with 3 to 4 milliliters of desired buffer solution. Once filled, the electrodes create a field stimulation region over the surface of the 22mm by 22mm cover slip.

The arm has the ability to secure any circular 25mm diameter glass cover slip at its midsection. This side of the cover slip facing the base plate is coated with a monolayer of cardiac myocytes. A 10 millimeter through hole allows both upper and

lower cover slips to be imaged in transmittance and fluorescence mode. Once a cover slip is secured to the lever arm (cells facing down), it can be lowered into the stimulation bath. The clamp design permits the cell monolayer to be positioned just microns over the optode membrane. The two cover slips then form an ultra-thin fluidic chamber. A standard M2 screw at the end of the lever arm allows precise control over chamber thickness.

Since the membrane is beneath the cell monolayer, there is no possibility of motion artifact interference. In addition, fluorescent and bright field data can be acquired simultaneously to examine the correlation between cell contraction and potassium flux. This is also useful in determining how effectively the electrodes are pacing the cells. Many of these features are not possible with the CSOS device.

The perimeter of the cover slip chamber is exposed to buffer, which could potentially cause problems with potassium ions diffusing into the surrounding fluid. However, when the cover slips are brought together, the chamber has a very large diameter-thickness ratio ($D/t > 1000$). At pacing frequencies of 0.5 Hz and higher the localized diffusion around the edge of the cell monolayer should not effect optode measurements at the center, which is the area being imaged.

The large bath volume outside the cover slips has several advantages. The buffer used with cardiac myocytes required approximately 10 mM glucose to keep the cells beating strong over extended test periods (> 40 min). With highly reduced volumes, the cells would burn through glucose very fast. With this system; however, glucose can slowly diffuse into the chamber from the surrounding bath. In addition, the large exposed bath makes compound additions simple and precise.

4.3.6: Stimulation Chamber Limitations

The primary limitation to the stimulation chamber system is its low throughput nature. It would be difficult to design a system using the chamber setup into standard 96 or 384-well plates. It would require the cell monolayer be inverted over the optode membrane. At best, this would require the fabrication of custom well plates with a complex system of membrane positioning and stimulation. Most crucially, existing automated cell culture infrastructures would not be able to accommodate this modified system.

This system was designed as a temporary test bed to evaluate the effectiveness of potassium optodes to detect action potential flux. As a result, there are some minor design flaws that detract from the systems ability to maximize signal to noise. These flaws include usable objectives, repeatable height control, and accurate cover slip positioning.

The shape of the conical cutout on the underside of the base plate prevents the use of high NA objectives. At best, the base plate was able to accommodate a 20X objective with a NA of 0.75. A wider cutout would permit the use of an oil-immersion 63X objective with an NA of 1.7, which would greatly improve the optical signal to noise ratio.

4.4 – Experimental Methods

4.4.1: Reagents

Neonatal cardiac myocytes arrived from Massachusetts General Hospital on 25mm glass cover slips immersed in 2 mL standard DMEM solution^{VII}. To run ion flux experiments, the growth solution was replaced with Buffer # 3, which consisted of 10 mM HEPES @ pH 7.4 supplemented with 137 mM NaCl, 2.7 mM KCl, 0.9 mM CaCl₂, and 10 mM Glucose. HEPES, salts, and glucose were acquired from Sigma-Aldrich at the highest available qualities. All optode reagents can be located in Chapter 1.

4.4.2: Optode Preparation 1: CSOS

The CSOS insert was prepared by first spin coating the end of the insert cylinder with a thin layer of K-Optode II. The cylinder was rigorously cleaned with THF to completely remove any previous optode membrane or other organic residue. It was then pressed into a custom motor shaft adaptor and spun at approximately 6,000 RPM. Once up to speed, ten uL of highly diluted K-Optode II were dropped on the cylinder surface during spinning (10 mL THF / 100 mg PVC). After 10 seconds, the motor was shut down and the membrane was allowed to dry for an additional 30 minutes.

Once dry, the insert cylinder was press fit into the housing until the optode membrane was flush with the lower housing face. This step was only required for potassium flux test runs. Transmittance control experiments were performed with the insert removed. The electrode extensions were connected to a 10 V P-P waveform generator. Typically, the generator was set to apply a 10V, 5 ms duration, square wave pulses at a frequency of 1.0 Hz.

4.4.3: Optode Preparation 2: Chamber

The stimulation chamber preparation was relatively simple. A 25 mm diameter No.1 glass cover slip was cleaned with THF to remove any organic residue. The disk was then spun at approximately 6,000 RPM while 15 μ L of (10 mL THF / 100 mg PVC) K-Optode II cocktail was pipetted onto the surface. Ten to fifteen seconds after cocktail application, the spin coater was shut down and the cover slip was placed in a fume hood for a minimum of thirty minutes to allow complete solvent evaporation.

4.4.4: Myocyte Culture

Neonatal cardiac myocytes were prepared by Dr. Saumya Das and staff at Massachusetts General Hospital. Typically, cells were harvested the Friday before the week of testing. Once fully separated, the myocytes were seeded onto cover slips and allowed to adhere for 48 hours over the weekend.

^{VII} Cells were generously provided from Dr. Saumya Das and Dr. David Milan at MGH

4.4.5: Testing Protocol 1: CSOS

Neonatal mouse cardiac myocytes were seeded in BD Falcon 12-well plates four days prior to testing at Mass General Hospital. Seeding densities were estimated to be medium to high (approximately 1 cell per 30 by 30 micron square). Upon arrival, the cells were placed in a 37°C 5.0% CO₂ incubator for 45 minutes to increase cell viability. The CSOS device was then prepared according to the protocols outlined in section 4.4.2. The optode membrane was pre-conditioned using a 100 mM KCl solution for 60 seconds. The membrane was then rinsed and exposed to a 500 mM Tris-HCl (pH 4.5) solution for an additional 60 seconds to fully protonate the chromoionophore. The assembly was then placed in a 12-well plate containing Buffer # 3 for 2-5 minutes prior to testing to allow complete optode equilibrium with the testing solution.

In the well of interest, all growth medium was extracted and the monolayer of cells was rinsed twice with Buffer # 3 pre-warmed to 37° C. The well was then filled with 200 µL of Buffer # 3. This volume ensured complete fluidic contact between the CSOS housing and the cell monolayer. With the insert cylinder removed, the CSOS housing was inserted into the well to conduct pacing control experiments. Keeping the well plate at a 30 degree tilt helped ensure complete removal of trapped air.

The entire assembly was then securely fixed to the microscope stage of a Carl Zeiss LSM 510 Meta Confocal inverted microscope. The large working distance of this setup required the use of a 10X objective, which was non-ideal due to its low NA. Cell excitability was verified by focusing on the cell monolayer (bright field) and pacing the cells at various frequencies. Time-series acquisitions could then be used to assess the consistency of cell contraction. If the cells showed strong unified contractile behavior, then potassium measurement experiments could proceed.

To measure potassium oscillations, the CSOS was removed and the pre-prepared insert cylinder was pressed into place. The assembly was then re-inserted into the well keeping the plate at a 30 degree angle to ensure air removal. The microscope settings were then re-configured to properly image the optode membrane. The pinholes were reduced to 1.0 array unit, which with a 10X objective is equivalent to a 10-12 micron optical slice. This was done to prevent any motion artifact interference from the beating cell monolayer. The optode membrane was excited using the 512 nm line of an argon laser. Two detector channels were configured to measure the 570 nm and 670 nm emission bands. Once detector gain and offset were maximized, time series image acquisitions were performed while pacing the cell monolayer at various frequencies.

4.4.6: Testing Protocol 2: Stimulation Chamber

A minimum of 48 hrs prior to testing, neonatal mouse cardiac myocytes were seeded at high density onto 25 mm No.1 diameter cover slips contained in standard 6-well cell culture plates. Laboratory observations indicated that optimal cell viability occurred between 72 and 96 hours after seeding. Cells showed much stronger beating and at higher frequencies after this prolonged culture period.

The first step to prepare the stimulation chamber involved securing the optode disk to the base plate. This was accomplished by applying a thin layer of vacuum grease

in the base plate region between the parallel electrodes. The pre-coated 22 mm by 22 mm cover slip was then pressed into place on the base plate between the electrodes. Ample pressure was applied around the perimeter of the cover slip to ensure a complete seal. The chamber was then flooded with 2.5 μ L of pre-warmed Buffer # 3.

Directly before testing, a single cell coated 25 mm cover slip was removed from its well and rinsed thoroughly with pre-warmed 37°C Buffer # 3. The under side of the disked was dried with a cloth and placed on the underside of the chamber arm (cells facing up). A small amount of vacuum grease between the 25 mm cover slip and the epoxy arm surface ensured a fluidic seal and prevented movement. The arm was then rotated so the cell monolayer was in contact with the bath fluid. At this point, the M2 screw was used to lower the cell monolayer to approximately 20 microns over the optode membrane.

The entire assembly was then securely fixed to the microscope stage of a Carl Zeiss LSM 510 Meta Confocal inverted microscope. The electrodes in the stimulation chamber are at a spacing of 25 mm, which is approximately four times larger than the CSOS electrode distance. To achieve the same voltage gradient over the cell monolayer, it was necessary to pulse the cells with 30 V in stead of 8 V. This was accomplished using an additional 30 V (1.0 amp) power supply connected to the electrodes through a quickly activating reed relay. The waveform generator was then able to activate the relay at the desired pacing frequency. Fluorescent data was acquired in the same manner outlined in Section 4.4.5. An additional transmitted light channel was used to simultaneously detect membrane movement during pacing.

4.4.7: Data Processing

Both systems described above were used with the Carl Zeiss LSM 510 Meta confocal inverted microscope. The acquired data consisted of a time series fluorescent images. Essentially, a video file of the optode membrane intensity. Typically, frame size was 128 by 128 pixels at an acquisition rate of 10-40 frames / second. To analyze time dependant fluorescent changes, small regions of each image were selected and the pixel intensities averaged. This was accomplished using Carl Zeiss LSM viewing software. The particular chosen regions were basically random, but it was vital to pick areas containing similar pixel intensities.

The resulting data was a group of time series vectors representing the average intensity of a small region of neighboring pixels over time. The data was imported in Origin 7 for further processing. A second order exponential decay curve was fit to each data set to model photo-bleaching. The decay fit curve was subtracted from the raw data to obtain a zero-mean time series. A backwards FFT amplitude analysis was conducted to generate a spectral power density plot for the time series. This would reveal any dominant frequency components. Typically, a FFT threshold filter was applied to eliminate white noise.

4.5 – Results and Discussion

4.5.1: CSOS Beat Pattern Results

A total of six time series experiments were conducted to evaluate the overall performance of the CSOS device.

The preliminary experiment was a negative control intended to investigate any optical interference created by electrical field stimulation. Since optode response is based on charge balance equilibrium, the presence of an electric field may affect optode signal. The CSOS device was placed into a well containing only buffer (no cell monolayer) and an electric field was applied over the optode membrane (2Hz pacing). The resulting mean-normalized fluorescent data is shown in Figure 53.

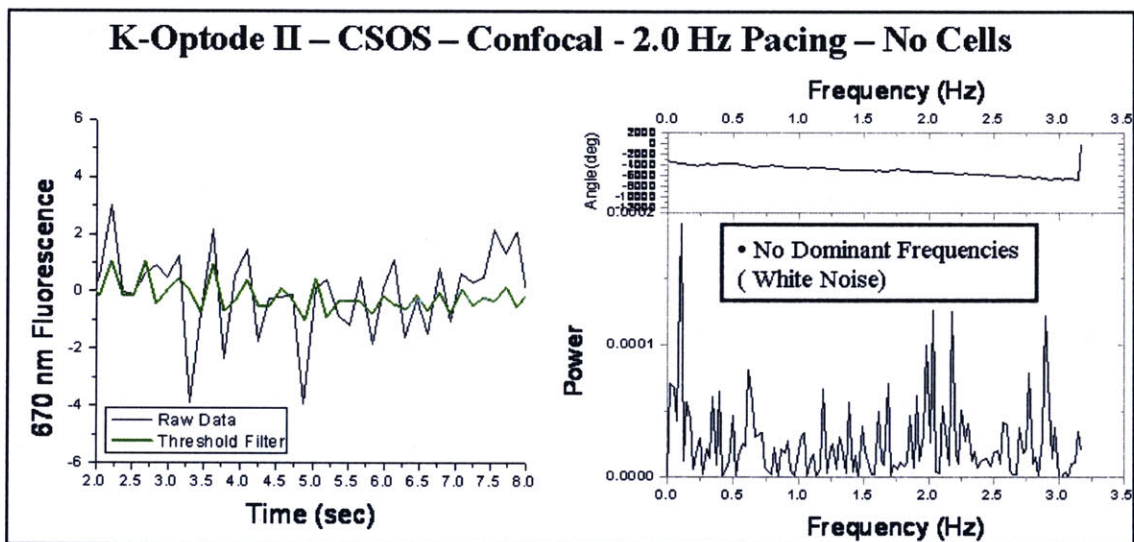


Figure 53: CSOS Negative Control Beat Data (No Cells)

The chromoionophore is primarily protonated at the experimental extracellular concentration of 2.7 mM. This causes the 670nm emission band intensity to be approximately ten times larger than the 570 nm band. To retain acceptable signal to noise levels, the amplifier gain had to be reduced to the point where the 570 nm channel was virtually non-existent. Therefore all initial experiments conducted on the confocal microscope produced only 670nm emission data.

The spectral power density analysis of the time series data is pictured in the right panel of Figure 53, which shows little to no indication of electrical interference. Notice how small the power scale is on the y-axis of the plot. There is a slight peak around 2.0 Hz, but there are also equivalent peaks at 1.8, 0.1, and 2.9 Hz. Overall, the system noise is uniformly distributed over all frequencies, which is indicative of classic white noise. The left panel shows the raw mean-normalized fluorescent data trace (black). An

additional amplitude threshold filter (FFT – green) is overlaid, which transmits only the most powerful frequencies. Visual inspection of this data indicates no oscillatory features. These results proved that electrical field stimulation through the buffer solution did not produce any noticeable interference signals.

Following the success of the negative control experiment, it was necessary to assess the ability of the CSOS to reliably field stimulate a cell monolayer using the embedded set of parallel electrodes. This will be an effective positive control for the following series of experiments.

The optode insert cylinder was removed and the CSOS housing was placed in a well containing a viable cell monolayer. By analyzing a region of pixels over a cell membrane, the transmitted light intensity will change as a result of cell contraction. Figure 54 shows the resulting beat pattern.

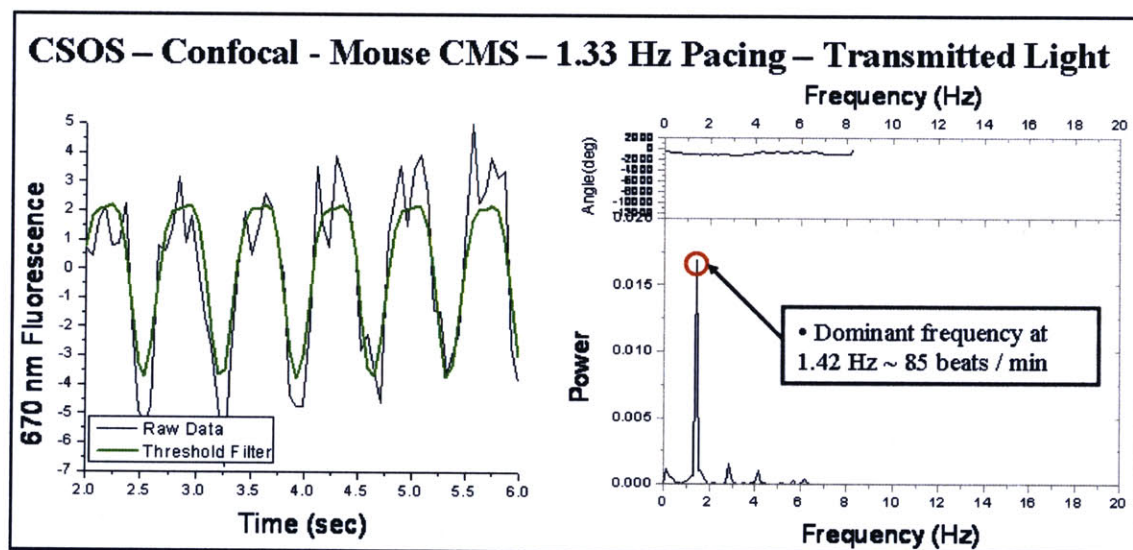


Figure 54: CSOS Transmitted Light Pacing Verification

The left panel of Figure 54 shows a very clear trace of cell membrane movement throughout the series of action potentials. The signal is very clean when compared to the fluorescent data shown in the following experiments. This is a result of the limited signal processing and amplification that occurs with bright field imaging. The FFT spectral power analysis shown in the right panel further exemplifies the distinction of the 1.33 Hz beat pattern.

Notice that no additional frequencies exist in the spectrum with any significant power. This is a strong indication that the cells are activating directly upon field stimulation. This also indicates that the cells are not being paced faster than their ion recovery period. If this were the case, the contractile strength would decrease over time. The cells could even fall into an arrhythmic beat pattern, which would present itself in the classic “double-beat” phenomenon. Usually this is the result of sodium and calcium channels not dropping below their re-activation potential upon stimulation. With “double-beat” behavior, the frequency analysis will reveal significant harmonics. Figure

54 indicates no such irregular beat patterns, thus the CSOS provided reliable cell field stimulation for this model situation.

With positive and negative controls both indicating acceptable device performance, four cell-based potassium experiments were conducted. All experiments were conducted in the same directly after each other. The only experimental parameter that differed was the electrical stimulation properties. After the positive control, the CSOS housing was removed from the well and the insert cylinder with K-Optode II was pressed into place. A single 670 nm fluorescent emission image is shown in the right panel of Figure 55. Notice the bright optode rings that extend diagonally across the image. This is a result of optode membrane being trapped in the machining grooves during fabrication (lathing). These regions provided relatively high signal to noise ratios.

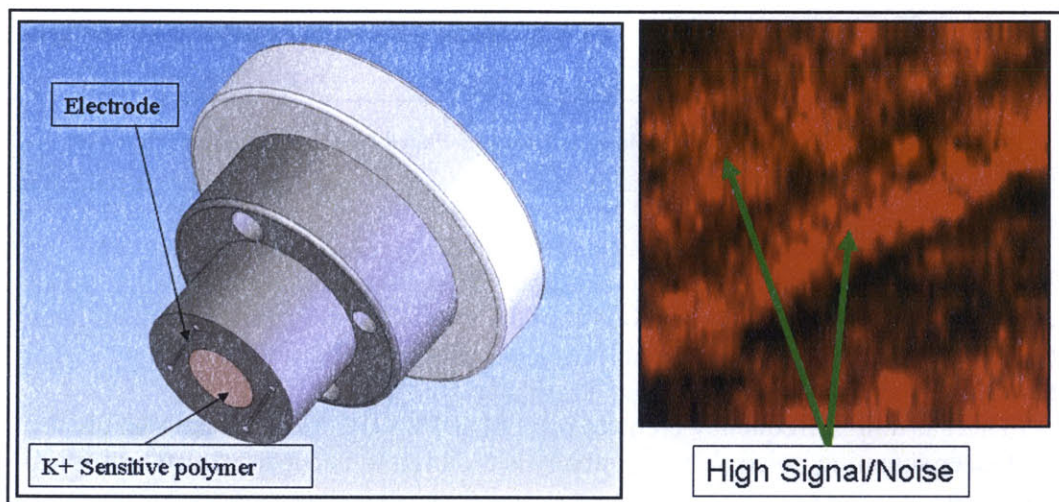


Figure 55: Fluorescent Image of the CSOS Optode Membrane (670nm Emission Band)

The first experiment did not employ electric field stimulation. This was to determine the natural beat frequency of the cell monolayer, if any at all. The natural beat frequency is necessary to gauge the range of feasible pacing frequencies which the cells can reliably pace at. Experimental observations indicated it was difficult to reliably pace the cell monolayer at frequencies 1.0 Hz above and below the natural beat frequency. Figure 56 shows the resulting time series data. As with Figure 53 and Figure 54, the left panel shows the raw mean-normalized fluorescence (black) with a FFT threshold filter (green). The right panel displays the FFT spectral frequency breakdown of the raw data.

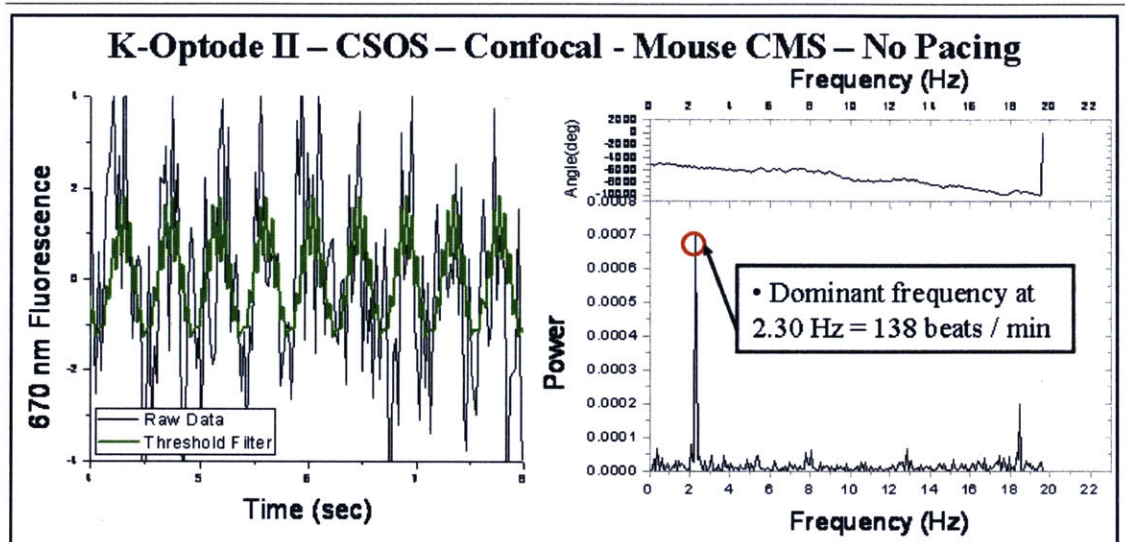


Figure 56: CSOS Potassium Oscillations from Un-Paced Neonatal Cardiac Myocytes

The spectral plot indicates a very strong oscillatory frequency present at 2.3 Hz, or 138 beats per minute. This rhythmic natural beating was also noticed during visual inspection before the CSOS was inserted into the well. In the left panel the beat pattern is clearly visible in both raw and filtered time series plots. In addition to a strong signal presence, there is little change in signal amplitude over time.

There is a high frequency element present at 18.5 Hz, which is most likely the result of laser scanning noise. The frequency is too high to occur from any biological phenomenon.

It is surprising how rhythmically the cells are able to beat with no external pacing. Later observations show this to be a strong indicator of cell health and confluence. The beat pattern in this data set has an excellent signal to noise (over 10), which was higher than anticipated from theoretical modeling.

The following three experiments used field stimulation to pace the cells at three different frequencies. To prevent arrhythmic behavior, the pacing frequencies were kept within 1.0 Hz of the natural beat frequency observed in the previous experiment. Figure 57, Figure 58, and Figure 59 show the time series potassium oscillation data from 2.0, 2.67, and 1.33 Hz pacing sets, respectively. Data for each data set includes raw and filtered time series plots along with the FFT spectral analysis.

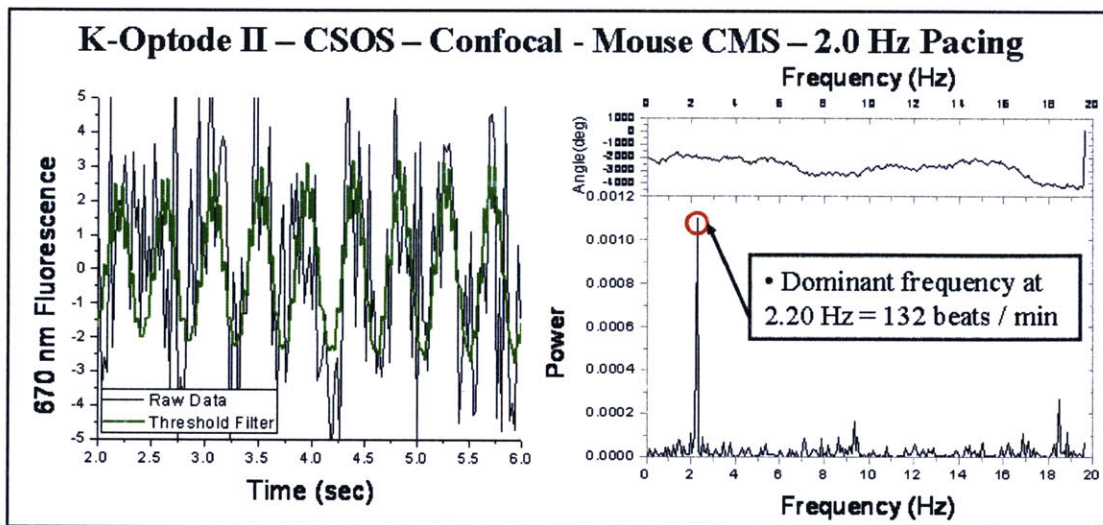


Figure 57: CSOS Potassium Oscillations from Neonatal Cardiac Myocytes
Pacing Frequency of 2.0 Hz

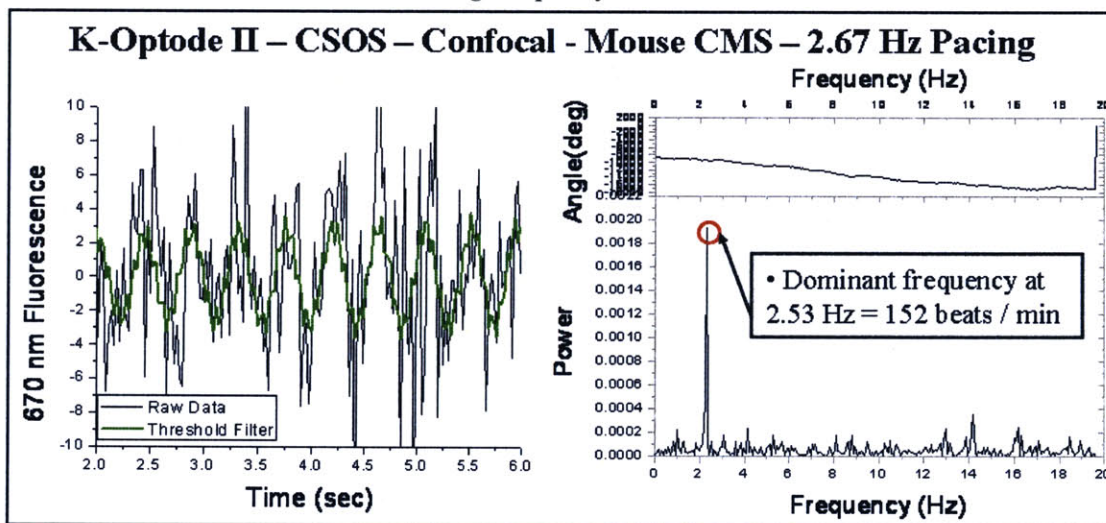


Figure 58: CSOS Potassium Oscillations from Neonatal Cardiac Myocytes
Pacing Frequency of 2.67 Hz

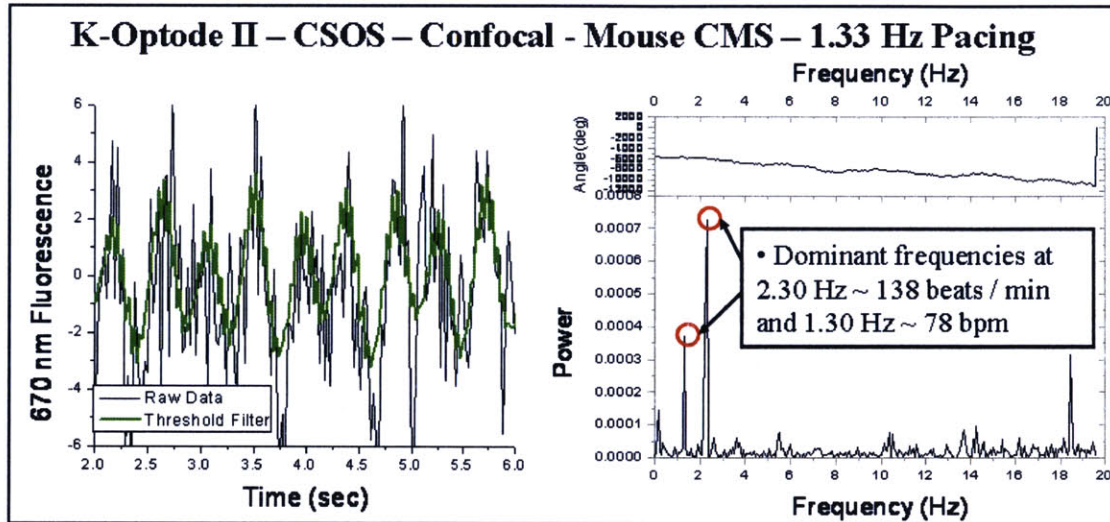


Figure 59: CSOS Potassium Oscillations from Neonatal Cardiac Myocytes Pacing Frequency of 1.33 Hz

When paced at 2.0 Hz, the presence of potassium oscillations are obvious, but at a slightly higher frequency of 2.2 Hz. This signal is clearly the only significant oscillatory pattern in the entire data set, which indicates the cells are beating slightly faster than their pacing frequency. Similarly, Figure 58 calculates the potassium oscillation at frequency 2.53 Hz when the actual pacing frequency is 2.67 Hz. In both cases, it seems the cells prefer to beat closer to their natural frequency of 2.3 Hz.

Figure 59 is particularly interesting. When paced at 1.33 Hz, the spectral analysis shows the presence of two beat frequencies at 2.3 and 1.3 Hz. As indicated by Figure 56, 2.3 Hz is the natural beat frequency for the cells. Surprisingly, the power of the 2.3 Hz signal is over double that of the pacing frequency signal at 1.3 Hz. This dual frequency phenomenon could be the result of two possible situations.

The first hypothesis for this behavior suggests that the cells are firing approximately 334 milliseconds before the stimulation pulse every other cycle. Since the natural frequency is much faster than the pacing speed, this scenario is highly plausible. Pre-firing would also account for the deviation in peak amplitude between every other cycle. This can be seen in the filtered data series of Figure 59 (green trace). Notice the spikes at 4.3 and 5.6 seconds are smaller than the 3.6 or 4.8 second spikes. If the cells are stimulated before they have fully re-polarized, they will not expel as much potassium during the second action potential. This would explain these observed amplitude discrepancies.

The second hypothesis for the dual-frequency phenomenon is that certain neighboring cells are beating at different frequencies. The CSOS measures extracellular potassium fluctuations over a field of cells. If the cells are not beating in sync, the optode will measure mixed signals. In addition, the cells outside the electrodes are most likely beating at their natural frequency of 2.3 Hz, which would introduce interfering potassium signals. This theory is also highly plausible and would explain the data.

Both of the above theories are sound, but further experimentation would be needed to determine which is valid. In either case, the data is interesting and gives insight into the potassium ion channel behavior at different beat frequencies.

The data presented in Figure 56 through Figure 59 gives significant creditability of the CSOS device to pace a monolayer of cells and simultaneously detect potassium oscillations. However, the system has an inherent design property introduces doubt to the validity of the above results. As stated previously, the optode membrane is imaged through the monolayer of beating cells. Cell membranes and random debris have the ability to alter light transmittance. Therefore it is conceivable that elements of these signals are derived from motion artifacts.

To validate the above data sets, a second series of control experiments were conducted to test the effect of any motion artifacts on fluorescent signal intensity. The tests involved using a K-Optode II membrane with no potassium ionophore. This will produce a non-changing fluorescent light source over the cells. The idea is to measure any fluorescent intensity changes that are a result of motion artifacts alone. To perform these tests, a custom cell chamber was designed and fabricated to maximize the possibility of any interference. A simple diagram of the test-rig is shown in Figure 60, which displays the overall layout of the system. It is designed for use on a wide field inverted fluorescent microscope. Using a wide field scope will include any shadow interference from out of focus objects, such as cells. This is also to maximize any motion artifact effects.

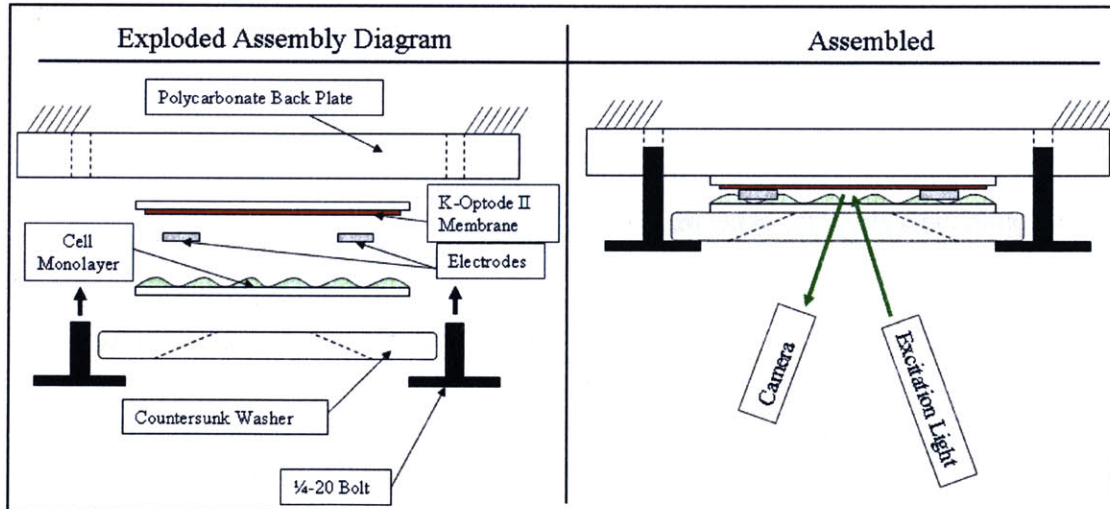


Figure 60: Diagram of Test Rig Used to Conduct Motion Artifact Studies

The system resembles a standard closed bath cell stimulation chamber only with a highly reduced chamber volume. The lower 25 mm cover slip was plated with cardiac myocytes. The upper 25 mm disk was then coated with the desired optode polymer. Both cover slips were then clamped together using washers and four 1/4-20 aluminum bolts. Clamped between the two disks were a set of 200 micron thick silver chloride foil

strips spaced at a distance of approximately 7 mm. In addition to being electrodes, the foil acted to distribute the clamping forces over the surfaces of the cover slips, preventing cracking.

The entire assembly was clamped onto the stage of a Carl Zeiss Axiovert inverted fluorescent microscope. Two optode membranes were used to conduct positive and negative control experiments. For the negative control series (motion artifact interference), a K-Optode II matrix was used without Potassium Ionophore III. Using a Rhodamine filter and a CCD Camera to image the optode membrane, the cells were paced at 1.0 Hz and membrane images were acquired at 35 fps for a total of twenty seconds. Figure 61 displays the resulting data from a random region of interest.

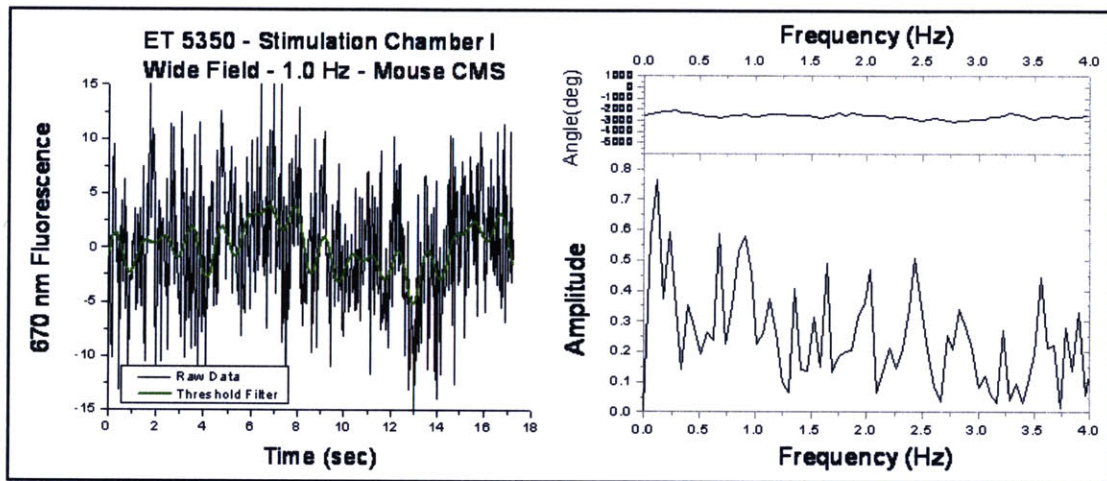


Figure 61: Negative Control Optode Signal from Motion Artifact Testing Rig

Both panels show no signs of any significant 1.0 Hz frequency elements. The spectral breakdown in the right panels displays typical white noise, with a slight bias towards lower frequencies. Several other regions over the membrane were analyzed and showed no indications of any 1.0 Hz frequency elements. This data clearly supports the argument that motion artifacts were not responsible for the oscillatory fluorescent signals reported in Figure 56 through Figure 59.

As a positive control for this series of tests, the previous experiment was replicated, but with a fully functional K-Optode II. Figure 62 shows the resulting time series data from this secondary experiment.

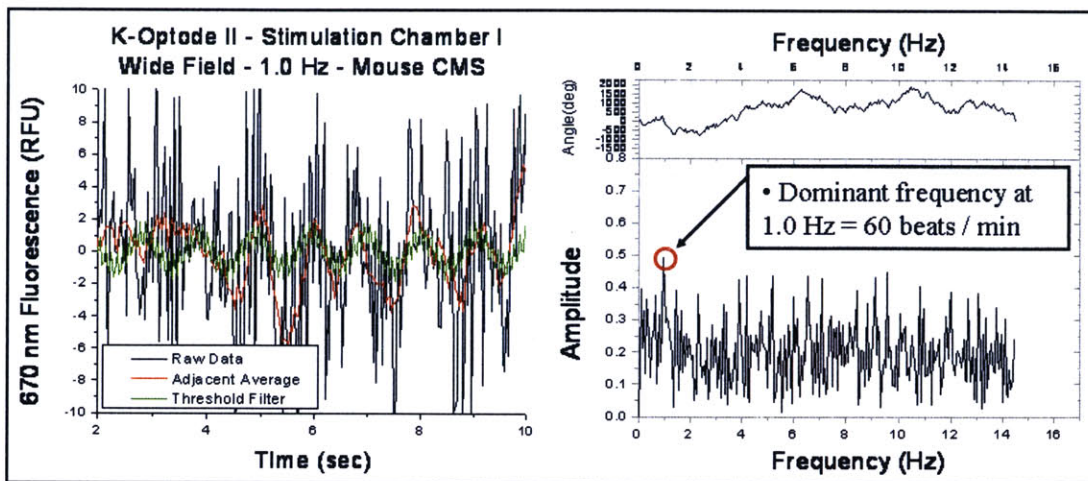


Figure 62: Positive Control Optode Signal from Motion Artifact Testing Rig

Despite a very low signal to noise ratio, both panels in Figure 61 show the presence of a 1.0 Hz signal. The poor signal to noise is the result of two system properties unique to this setup. The most apparent of these is the inability of the Rhodamine filter to fully capture the 670 nm emission. In fact, the filter will capture fluorescent emission from the 570 nm band, which will dramatically reduce optical sensitivity. The lack of signal is also the result of the large (200 micron) gap between the cells and the optode membrane. The CSOS is capable of gaps as little as 50-100 microns, which amplifies potassium oscillation amplitude.

4.5.2: Optode Chamber Beat Pattern Results

The optode stimulation chamber described in Section 4.3.3 was used in a series of highly controlled experiments to obtain irrefutable potassium flux data. Initial experiments served to verify the ability of the system to detect potassium oscillations. Since these results were similar to the experimental data reported in the previous section, they will be omitted.

Ultimately, this technology is intended to detect potassium channel blockage caused from arrhythmic compounds (drug induced LQT syndrome). This ability was evaluated in an experiment that exposed cardiac myocytes to Haloperidol, a documented LQT inducing drug. This experiment was conducted on March 2nd, 2006 at Draper Laboratory. Using a Z-stack, the gap between optode membrane and cell monolayer was estimated to be between 10 and 15 microns.

The natural beat frequency of the cells was approximately 0.8 Hz, so a 1.0 Hz pacing frequency was used to obtain reliable cell contractions. The stage was positioned to view a particularly high cell density region. The area of interest was a 100 percent confluence, resembling a thin layer of cardiac tissue. At an acquisition rate of 50 milliseconds (20Hz), 50 seconds of fluorescent and transmitted data was recorded. 25

seconds into the run, Haloperidol was added to the bath to obtain a final concentration of 2.0 μM , which is slightly over its reported EC50 value. Figure 63 shows the resulting data from the first and last twenty seconds of acquisition, which represent pre and post dosing time series data sets.

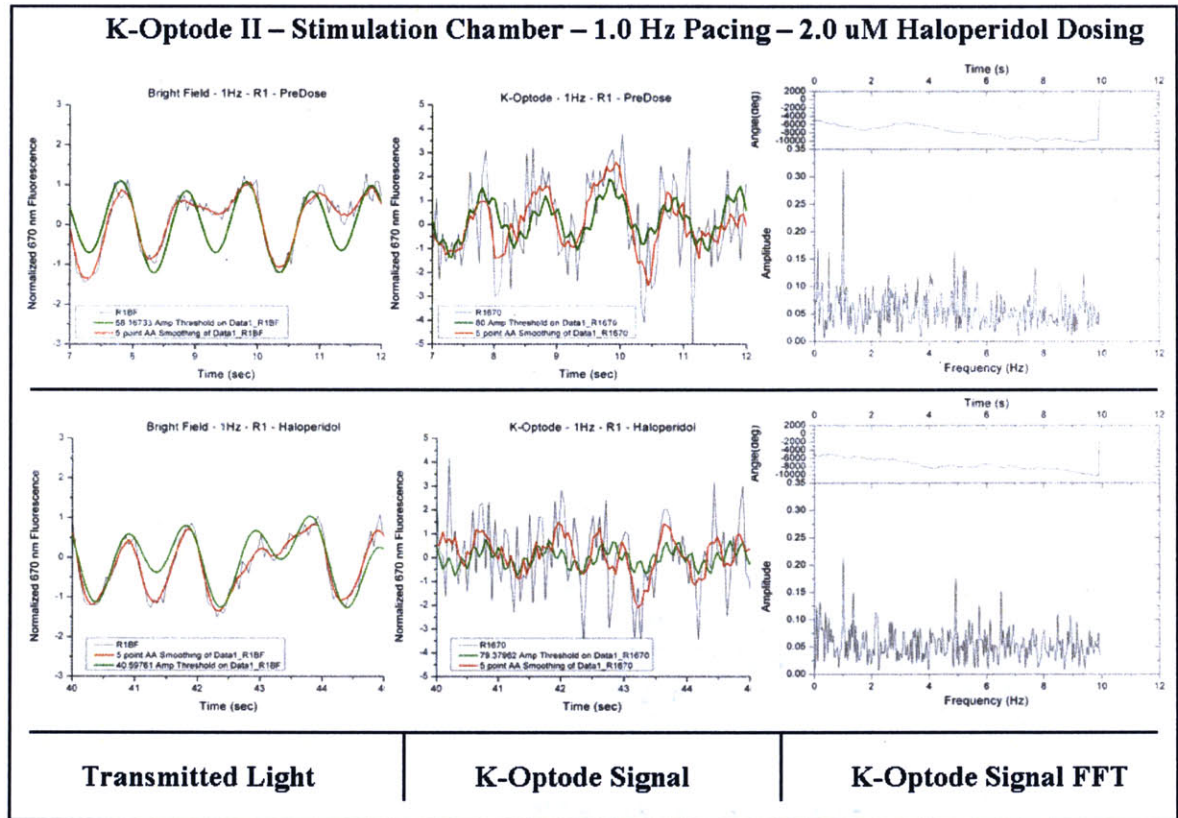


**Figure 63: Haloperidol Effect on Potassium Oscillation Magnitude
(Recorded Using the Stimulation Chamber)**

The upper panels indicate beat data prior to Haloperidol addition. Conversely, the lower panels show data starting five seconds after drug addition. The left most panels show the transmitted light intensity changes, which are a good indicator of membrane movement (contraction strength). The beat traces show little difference before and after drug addition. Due to the high cell density, the previously described “double-beat” phenomenon was present in both time series data sets. The FFT power spectrum (not pictured), indicated only a 4% change in signal amplitude change between pre and post drug addition data sets. From these plots, Haloperidol had little to no measurable effect on beat strength or regularity according to transmitted light data.

The two middle panels of Figure 63 show the 670 nm emission band time series data from K-Optode II. Before drug addition (upper panel), the beat pattern is clearly recognizable with no filtering (black trace). The red and green filtered traces further show the strong presence of 1.0 Hz potassium oscillations by eliminating high frequency

noise. The FFT spectral analysis also shows a strong 1.0 Hz signal with an amplitude of approximately 0.32. The average background noise has an amplitude of around 0.10, so the system was able to achieve a signal to noise ratio of over three to one. It is interesting to note the absence of the “double-beat” phenomenon in the potassium oscillations. At around nine seconds, the upper left panel shows a highly apparent double-beat. The potassium trace shows no such phenomenon at that point in time. This also supports the argument that these oscillations are not the result of shadows or other motion artifacts. It also suggests that the double-beat is the result of a malfunction with either sodium or calcium channels. If the membrane is not fully de-polarized when field stimulated, the sodium and calcium currents will be reduced in magnitude, which may account for less available calcium to trigger contraction. The double-beat could also be the product of cell-to-cell interactions. In either case, the potassium oscillations are strong and stable prior to drug exposure.

After Haloperidol addition, the potassium oscillations (lower middle panel) were severely affected. Even with a FFT threshold filter (green trace), the 1Hz oscillations are not obvious in the time series trace. The spectral analysis in the lower right panel indicates a dramatic reduction in 1.0 Hz signal amplitude. After dosing, the potassium oscillation amplitude was reduced by over 30 percent. It is surprising how dramatically the potassium flux was affected with Haloperidol, but the bright field traces remained relatively unchanged.

Overall, the stimulation chamber provided a reliable test bed to conduct optode based potassium flux experiments. As stated, it would be difficult to adapt this technology for high throughput infrastructures, but these results clearly demonstrate its ability to detect drug induced potassium channel blockage. This technology could soon provide an attractive alternative to patch clamp methods in the field of high throughput hERG screening.

4.5.3: hERG Screening Future Work

Both of the above systems (CSOS and Stimulation Chamber) showed the ability to reliably measure potassium flux from a layer of cardiac myocytes. For optimal performance, the signal to noise ratio of this optical system needs to be dramatically improved. This could be accomplished by improving both optode performance and cell signaling.

Optode performance can be improved by enhancing the sensitivity and overall fluorescent intensity. Sensitivity can be improved by altering the component concentrations within the membrane. As the Introduction showed, increasing ionophore and additive while decreasing chromoionophore concentration could increase sensitivity by up to two fold. Additional signal could be achieved by employing thicker membrane; however, the response time must still remain below 100 ms at most. An alternative solution could be the use of micro-sphere deposition. The resulting “mesh” of spherical particles produced by micro-sphere deposition (Chapter 1) has a higher surface area to volume ratio than traditional constant thickness membranes. This would allow for higher signal while retaining adequate response times.

Signal to noise ratios could also be improved by increasing extracellular potassium concentration fluctuation amplitude. The most obvious approach to this problem is to increase the density of the cell monolayer. This is difficult to achieve with cardiac myocytes due to their contractile behavior. As an alternative, hERG transfected HEK 293 cells could be used. Their capacitance is similar to neonatal cardiac myocytes and they are capable of producing action potentials. In addition, the effect of hERG blocking compounds would be dramatically increased. This would permit extremely tight cell packing and would eliminate any motion artifacts or induced flow.

Potassium flux amplitude could also be increased by reducing the initial extracellular potassium concentration. Although the raw change in concentration would remain constant, the percentage change in potassium would increase. This would essentially increase the sensitivity of the optode and improve the overall signal to noise ratio for the system. It is unclear how far the extracellular potassium concentration can be reduced before affecting cellular response. This will need to be determined empirically for every cell line.

If all the above parameters are optimized, it may be possible to design a 96 or 384-well system for high throughput applications. With an adequately high signal to noise ratio, the motion artifact over a large area of cells should be negligible. This would permit imaging through the cell monolayer. An initial concept “strip” prototype system is shown in Figure 64 below.

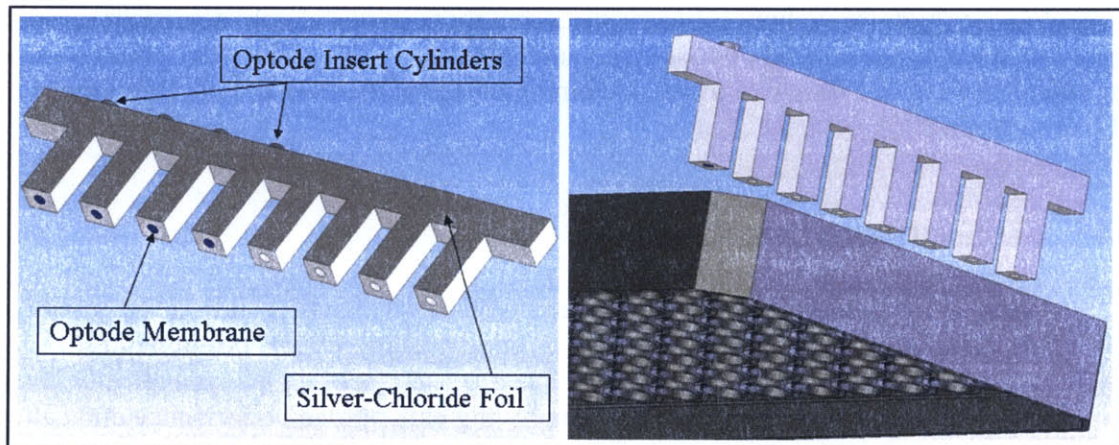


Figure 64: Solid Model of a Multi-Well hERG Screening Device

The silver chloride foil on either side of the housing would provide field stimulation of the cell monolayer. Each well would contain a removable optode insert cylinder that could be coated with any type of optode membrane. It is hoped that the square design will help to prevent bubble formation under the optode cylinders. Additional designs are being considered that allow for robotic fluid additions. This is just one particular example of possible future prototype systems.

Conclusions

The development of novel drug compounds is a highly expensive and time consuming process [69]. It has been estimated that it takes over one billion dollars to bring a single drug to market over a time period of up to twenty years [8]. Pharmaceutical companies and research laboratories all over the world are continuously seeking and investigating new technologies to streamline drug discovery.

High throughput compound screening comprises a considerable percentage of the drug development process [70]. In particular, whole cell assays are excellent *in vitro* predictors of drug efficacy. They are used to prune back massive libraries of possible compounds to a small group of compounds that will proceed to animal, toxicity, and clinical studies. Whole cell assays traditionally measure cell activity using a single critical biomarker, such intracellular calcium concentration. This technique is effective, but can produce large percentages of false positive and negative results. The errors in this system are derived from using only a single biomarker to evaluate activity. For a more complete measurement of cellular activity, additional biomarkers are required. This may be the key to accelerating the discovery of new therapeutically relevant drug compounds [70].

Every mammalian cell contains large populations of ion channels throughout its membrane. Ion channels have the ability to control the cells membrane conductivity towards a particular ion. The four primary ions that are used to regulate membrane potential and cell activity are potassium, sodium, calcium, and chloride. Virtually all cellular activity results in some form of ion flux across the cell membrane [2]. The resulting ion flux creates a change in both intra and extracellular concentration of that ion. As stated, current assays are best at measuring intracellular calcium concentration. Measuring changes in potassium, sodium, and chloride flux would give additional insight into cellular activity.

This report described the development of potassium and sodium sensitive optical ion sensors (Optodes). An Optode is a plasticized polymer that changes optical properties in response to the target ion concentration in the surrounding solution [34, 35]. Using novel devices, these optodes were capable of measuring changes in extracellular ion concentration caused by compound induced cellular ion flux. For this report, the state of an optode was measured using fluorescent emission intensity.

Each optode displayed excellent selectivity against other interfering ions. In particular, the K-Optode II matrix proved to be 1000 times more selective for potassium over sodium. The best commercially available potassium dyes are only 1.5 times more selective for potassium over sodium. In addition to selectivity, these optodes are highly sensitive. The estimated resolution for the K-Optode II matrix in this report was 48.1 μM . These detection capabilities allow this optode to reliably measure cellular ion flux.

Both optodes displayed typical first order response behavior to step changes in concentration. If sufficiently thin, these optode membranes were capable of achieving millisecond response times. Their fast response time was critical in the detection of potassium flux during the action potentials of field stimulated cardiac myocytes. Overall, these two optodes proved to be highly robust sensors for their respective ions.

Physically, an optode can be formed into any shape; therefore, there are endless possibilities for fabrication and implementation. This report discussed several fabrication

techniques that were able to produce thin optode membranes. These techniques included spin coating, spray coating, micro-sphere deposition, and evaporation. Each technique had unique advantages and disadvantages, but they were all effective. Experimental observations concluded that spin coating was dominant in producing consistent uniform thickness coatings. However, this required the substrate to be spun at high speed, which prevented multiple coating on the same part. Typically, spun coat substrates were limited to disks or cylinders. Micro-sphere deposition was more difficult to perform, but resulted in fast response times because of the increased surface area to volume ratio.

The core of this report detailed the use of these optodes in three applications for the detection of extracellular ion flux. The first two applications included novel optode based whole cell assays for drug screening (detection of “hit” compounds). One assay system was specifically engineered for use with suspended cell lines and the other for adherent. Both systems were designed to be easily integrated with existing high throughput drug screening infrastructures.

The suspended cell assay described in this report consisted of optode coated disks placed at the bottom of standard 96 and 384-well plates. To investigate the performance of the assay a model cellular system was tested. The assay proved capable of detecting long term potassium and sodium flux from wild type *Saccharomyces Cerevisiae* (yeast) when stimulated with Haloperidol and Ifenprodil. Sensitivity was large enough to produce accurate dose-response curves for Haloperidol. The drawback to this system was the difficult and time consuming process of coating individual optode disks and placing them at the base of each well. Automation could be used to streamline this process, but there were additional disadvantages to the optode disk system (movement). Current work is being performed which employs micro-sphere deposition to form optode membranes at the base of multi-well plates. Initial results look promising and this technique will most likely be employed for future suspended cell assays.

Using optodes with adherent cell lines provided a host of additional design problems. The most severe being the restriction on total fluid volume within each well. In standard 96-well plates, the total fluid volume could not exceed 25 μL to retain acceptable signal to noise levels. This problem was solved using a single insert module that positioned an optode membrane within a hundred microns of the cell monolayer. This restricted fluid volume and allowed for effective imaging using standard plate readers. The system is highly compatible with almost any commercial plate reading system and could easily be adapted for robotic fluid handling. The insert module was evaluated using fully confluent HEK 293 cells with potassium optodes to measure ion flux. Extracellular potassium flux was detected after stimulation with Isoproterenol and Forskolin, which are known producers of intracellular cyclic AMP. Cyclic AMP has been shown to activate calcium channels [57]. The influx of calcium into the cell should then produce an outward potassium current to balance membrane potential. Dose response curves were generated for each compound, which produced accurate EC50 values. The optode insert module showed robust performance with this model assay.

Finally, a specialized system was developed that used a potassium optode with neonatal cardiac myocytes to detect potassium flux during an action potential. The goal of the system was to measure changed in potassium flux magnitude when the cells are exposed to a known channel blocker, such as 4-AP or Haloperidol. Initial experiments proved the systems ability to track potassium oscillations from series of field induced

action potentials. A secondary test showed a 30% reduction in potassium flux amplitude after exposure to 2.0 μ M Haloperidol.

As a whole, this report uncovers some advantages of using optodes to detect extracellular ion flux. To date, no sensor systems exist that can measure extracellular ion flux in standard multi-well plate configurations using commercially available plate readers. By measuring multiple ion fluxes, this technology is able to accurately characterize cellular activity in a high throughput format. Above all, this system can measure activity without altering cell function in any way.

Biographical Note

Daniel I. Harjes was born in Olney Maryland, but grew up in Hanover New Hampshire just a few miles away from the Dartmouth College main campus. He attended Hanover High School from 1996 to 2000. Daniel received his Bachelors of Science in Mechanical Engineering from Lehigh University in Bethlehem Pennsylvania in June 2004. During the summers between 1998 and 2002 Daniel worked at the Cold Regions Research and Engineering Laboratory (CRREL) located in Hanover New Hampshire under the supervision of Dr. Sally Shoop. His work consisted of dynamic vehicle modeling and validation. Publications produced during this time include “Seasonal Deterioration of unsurfaced roads” *Journal of Geotechnical and Geoenvironmental Engineering* and “Mechanical System Simulations for Seismic Signature Modeling” (Available at *Storming Media*).

Bibliography

1. Barberis, A., *Cell-Based High-Throughput Screens for Drug Discovery*. European BioPharmaceutical Review, 2002(Winter 2002).
2. Hille, B., *Ion Channels of Excitable Membranes*. Third ed. 2001: Sinauer Associates, Inc.
3. Fischmeister, R. and A. Shrier, *Interactive effects of isoprenaline, forskolin and acetylcholine on Ca²⁺ current in frog ventricular myocytes*. J Physiol, 1989. **417**: p. 213-39.
4. Seamon, K.B., W. Padgett, and J.W. Daly, *Forskolin: unique diterpene activator of adenylate cyclase in membranes and in intact cells*. Proc Natl Acad Sci U S A, 1981. **78**(6): p. 3363-7.
5. Varani, K., et al., *Pharmacological characterization of novel adenosine ligands in recombinant and native human A2B receptors*. Biochem Pharmacol, 2005. **70**(11): p. 1601-12.
6. Netzer, R., et al., *Screening lead compounds for QT interval prolongation*. Drug Discov Today, 2001. **6**(2): p. 78-84.
7. Trudeau, M.C., et al., *HERG, a human inward rectifier in the voltage-gated potassium channel family*. Science, 1995. **269**(5220): p. 92-5.
8. Griffith, L.G. and M.A. Swartz, *Capturing complex 3D tissue physiology in vitro*. Nat Rev Mol Cell Biol, 2006. **7**(3): p. 211-24.
9. Lindsay, M.A., *Target discovery*. Nat Rev Drug Discov, 2003. **2**(10): p. 831-8.
10. Bolten, B.M. and T. DeGregorio, *From the analyst's couch*. Trends in development cycles. Nat Rev Drug Discov, 2002. **1**(5): p. 335-6.
11. Schreiter, C., et al., *Reversible sequential-binding probe receptor-ligand interactions in single cells*. Chembiochem, 2005. **6**(12): p. 2187-94.
12. Durick, K. and P. Negulescu, *Cellular biosensors for drug discovery*. Biosens Bioelectron, 2001. **16**(7-8): p. 587-92.
13. Takahashi, A., et al., *Measurement of intracellular calcium*. Physiol Rev, 1999. **79**(4): p. 1089-125.
14. Luo, C.H. and Y. Rudy, *A model of the ventricular cardiac action potential. Depolarization, repolarization, and their interaction*. Circ Res, 1991. **68**(6): p. 1501-26.
15. Nygren, A., et al., *Mathematical model of an adult human atrial cell: the role of K⁺ currents in repolarization*. Circ Res, 1998. **82**(1): p. 63-81.
16. Yang, T. and D.M. Roden, *Extracellular potassium modulation of drug block of I_{Kr}. Implications for torsade de pointes and reverse use-dependence*. Circulation, 1996. **93**(3): p. 407-11.
17. Redfern, W.S., et al., *Relationships between preclinical cardiac electrophysiology, clinical QT interval prolongation and torsade de pointes for a broad range of drugs: evidence for a provisional safety margin in drug development*. Cardiovascular Research, 2003. **58**: p. 32-45.
18. Fenichel, R.R., et al., *Drug-induced torsades de pointes and implications for drug development*. J Cardiovasc Electrophysiol, 2004. **15**(4): p. 475-95.

19. Keating, M.T. and M.C. Sanguinetti, *Molecular and cellular mechanisms of cardiac arrhythmias*. Cell, 2001. **104**(4): p. 569-80.
20. Zhou, Z., et al., *HERG channel dysfunction in human long QT syndrome. Intracellular transport and functional defects*. J Biol Chem, 1998. **273**(33): p. 21061-6.
21. Tan, H.L., et al., *Electrophysiologic mechanisms of the long QT interval syndromes and torsade de pointes*. Ann Intern Med, 1995. **122**(9): p. 701-14.
22. Rudy, J.S.Y., *Subunit Interaction Determines IKs Participation in Cardiac Repolarization and Repolarization Reserve*. Circulation, 2005(112): p. 1384-1391.
23. Sanguinetti, M.C. and P.B. Bennett, *Antiarrhythmic drug target choices and screening*. Circ Res, 2003. **93**(6): p. 491-9.
24. Berecki, G., et al., *HERG channel (dys)function revealed by dynamic action potential clamp technique*. Biophys J, 2005. **88**(1): p. 566-78.
25. Katchman, A.N., et al., *Comparative Evaluation of HERG Currents and QT Intervals following Challenge with Suspected Torsadogenic and Non-Torsadogenic Drugs*. J Pharmacol Exp Ther, 2005.
26. Dorn, A., et al., *Evaluation of a high-throughput fluorescence assay method for HERG potassium channel inhibition*. J Biomol Screen, 2005. **10**(4): p. 339-47.
27. Sorota, S., et al., *Characterization of a hERG screen using the IonWorks HT: comparison to a hERG rubidium efflux screen*. Assay Drug Dev Technol, 2005. **3**(1): p. 47-57.
28. Guo, L. and H. Guthrie, *Automated electrophysiology in the preclinical evaluation of drugs for potential QT prolongation*. J Pharmacol Toxicol Methods, 2005. **52**(1): p. 123-35.
29. Witchel, H.J., et al., *Troubleshooting problems with in vitro screening of drugs for QT interval prolongation using HERG K⁺ channels expressed in mammalian cell lines and Xenopus oocytes*. J Pharmacol Toxicol Methods, 2002. **48**(2): p. 65-80.
30. Ammann, D., P.S. Chao, and W. Simon, *Valinomycin-based K⁺ selective microelectrodes with low electrical membrane resistance*. Neurosci Lett, 1987. **74**(2): p. 221-6.
31. Anker, P., et al., *Potentiometry of Na⁺ in undiluted serum and urine with use of an improved neutral carrier-based solvent polymeric membrane electrode*. Clin Chem, 1983. **29**(8): p. 1508-12.
32. Anker, P., et al., *Determination of [K⁺] in blood serum with a valinomycin-based silicone rubber membrane of universal applicability to body fluids*. Clin Chem, 1983. **29**(7): p. 1447-8.
33. Kilbourn, B.T., et al., *Structure of the K⁺ complex with nonactin, a macrotetrolide antibiotic possessing highly specific K⁺ transport properties*. J Mol Biol, 1967. **30**(3): p. 559-63.
34. Bakker, E., P. Buhlmann, and E. Pretsch, *Carrier-Based Ion-Selective Electrodes and Bulk Optodes. 1. General Characteristics*. Chem Rev, 1997. **97**(8): p. 3083-3132.
35. Seiler, K. and W. Simon, *Theoretical aspects of bulk optode membranes*. Analytica Chimica Acta, 1992. **266**: p. 73-87.

36. Johnson, R.D. and L.G. Bachas, *Ionophore-based ion-selective potentiometric and optical sensors*. Anal Bioanal Chem, 2003. **376**(3): p. 328-41.
37. Peper, S., I. Tsagkatakis, and E. Bakker, *Cross-linked dodecyl acrylate microspheres: novel matrices for plasticizer-free optical ion sensing*. Analytica Chimica Acta, 2001. **442**: p. 25-33.
38. Buhlmann, P., E. Pretsch, and E. Bakker, *Carrier-Based Ion-Selective Electrodes and Bulk Optodes. 2. Ionophores for Potentiometric and Optical Sensors*. Chem Rev, 1998. **98**(4): p. 1593-1688.
39. Simon, W. and E. Carafoli, *Design, properties, and applications of neutral ionophores*. Methods Enzymol, 1979. **56**: p. 439-48.
40. Bakker, E. and W. Simon, *Selectivity of Ion-Sensitive Bulk Optodes*. Anal Chem, 1992. **64**: p. 1805-1812.
41. Bakker, E., et al., *Selectivity of polymer membrane-based ion-selective electrodes: self-consistent model describing the potentiometric response in mixed ion solutions of different charge*. Anal Chem, 1994. **66**(19): p. 3021-30.
42. Seiler, K., et al., *Design and Characterization of a Novel Ammonium Ion Selective Optical Sensor Based on Neutral Ionophores*. Analytical Sciences, 1989. **5**: p. 557-561.
43. Lerchi, M., et al., *Lead-Sensitive Bulk Optodes Based on Neutral Ionophores with Subnanomolar Detection Limits*. Anal Chem, 1992. **64**: p. 1534-1540.
44. Shortreed, M.R., S. Dourado, and R. Kopelman, *Development of a fluorescent optical potassium-selective ion sensor with ratiometric response for intracellular applications*. Sensors and Actuators, 1997. **B**(38-39): p. 8-12.
45. Shortreed, M., E. Bakker, and R. Kopelman, *Miniature sodium-selective ion-exchange optode with fluorescent pH chromoionophores and tunable dynamic range*. Anal Chem, 1996. **68**(15): p. 2656-62.
46. Tai, D.C., et al., *Correction of motion artifact in transmembrane voltage-sensitive fluorescent dye emission in hearts*. Am J Physiol Heart Circ Physiol, 2004. **287**(3): p. H985-93.
47. Retter, R., et al., *Flow cytometric ion detection with plasticized poly(vinyl chloride) microspheres containing selective ionophores*. Anal Chem, 2002. **74**(20): p. 5420-5.
48. Clark, H.A., et al., *Optical nanosensors for chemical analysis inside single living cells. 2. Sensors for pH and calcium and the intracellular application of PEBBLE sensors*. Anal Chem, 1999. **71**(21): p. 4837-43.
49. Shortreed, M., E. Monson, and R. Kopelman, *Lifetime enhancement of ultrasmall fluorescent liquid polymeric film based optodes by diffusion-induced self-recovery after photobleaching*. Anal Chem, 1996. **68**(22): p. 4015-9.
50. Wang, E., et al., *Optical sensors for sodium, potassium and ammonium ions based on lipophilic fluorescein anionic dye and neutral carriers*. Analytica Chimica Acta, 1997. **357**: p. 85-90.
51. Bornside, D.E., C.W. Macosko, and L.E. Scriven, *Spin coating: One-dimensional model*. J Appl Phys, 1989. **66**(11): p. 5185-5193.
52. Lawrence, C.J., *The mechanics of spin coating of polymer films*. Phys Fluids, 1988. **31**(10): p. 2786 - 2795.

53. Hughes, T.R., *Yeast and drug discovery*. *Funct Integr Genomics*, 2002. **2**(4-5): p. 199-211.
54. Hahnenberger, K.M. and S.E. Kurtz, *A drug screening program for ion channels expressed in yeast*. *Trends Biotechnol*, 1997. **15**(1): p. 1-4.
55. Soustre, I., et al., *Sterol metabolism and ERG2 gene regulation in the yeast *Saccharomyces cerevisiae**. *FEBS Lett*, 2000. **470**(2): p. 102-6.
56. Moebius, F.F., et al., *Yeast sterol C8-C7 isomerase: identification and characterization of a high-affinity binding site for enzyme inhibitors*. *Biochemistry*, 1996. **35**(51): p. 16871-8.
57. Wayman, G.A., T.R. Hinds, and D.R. Storm, *Hormone stimulation of type III adenylyl cyclase induces Ca²⁺ oscillations in HEK-293 cells*. *J Biol Chem*, 1995. **270**(41): p. 24108-15.
58. Zhou, Z., et al., *Properties of HERG channels stably expressed in HEK 293 cells studied at physiological temperature*. *Biophys J*, 1998. **74**(1): p. 230-41.
59. Meltzer, J. and J. Santos-Sacchi, *Temperature dependence of non-linear capacitance in human embryonic kidney cells transfected with prestin, the outer hair cell motor protein*. *Neurosci Lett*, 2001. **313**(3): p. 141-4.
60. Cooper, J., S.J. Hill, and S.P. Alexander, *An endogenous A2B adenosine receptor coupled to cyclic AMP generation in human embryonic kidney (HEK 293) cells*. *Br J Pharmacol*, 1997. **122**(3): p. 546-50.
61. Holgate, S.T., *The Quintiles Prize Lecture 2004. The identification of the adenosine A2B receptor as a novel therapeutic target in asthma*. *Br J Pharmacol*, 2005. **145**(8): p. 1009-15.
62. Peakman, M.C. and S.J. Hill, *Endogenous expression of histamine H1 receptors functionally coupled to phosphoinositide hydrolysis in C6 glioma cells: regulation by cyclic AMP*. *Br J Pharmacol*, 1994. **113**(4): p. 1554-60.
63. Benton, D.C., et al., *Small conductance Ca²⁺-activated K⁺ channels formed by the expression of rat SK1 and SK2 genes in HEK 293 cells*. *J Physiol*, 2003. **553**(Pt 1): p. 13-9.
64. Zhang, J.H., T.D. Chung, and K.R. Oldenburg, *A Simple Statistical Parameter for Use in Evaluation and Validation of High Throughput Screening Assays*. *J Biomol Screen*, 1999. **4**(2): p. 67-73.
65. Nuss, H.B. and E. Marban, *Electrophysiological properties of neonatal mouse cardiac myocytes in primary culture*. *J Physiol*, 1994. **479** (Pt 2): p. 265-79.
66. Rampe, D., et al., *The antipsychotic agent sertindole is a high affinity antagonist of the human cardiac potassium channel HERG*. *J Pharmacol Exp Ther*, 1998. **286**(2): p. 788-93.
67. Akamine, T., et al., *Effects of haloperidol on K(+) currents in acutely isolated rat retinal ganglion cells*. *Invest Ophthalmol Vis Sci*, 2002. **43**(4): p. 1257-61.
68. Cohen, I. and R. Kline, *K⁺ fluctuations in the extracellular spaces of cardiac muscle. Evidence from the voltage clamp and extracellular K⁺ - selective microelectrodes*. *Circ Res*, 1982. **50**(1): p. 1-16.
69. Armer, R.E. and I.D. Morris, *Trends in early drug safety*. *Drug News Perspect*, 2004. **17**(2): p. 143-8.
70. Handen, J.S., *High Throughput Screening challenges for the future*. *Drug Discovery World*, 2002. **Summer 2002**: p. 47-50.

